INVESTIGATING THE MICROSTRUCTURE EVOLUTION OF INDUSTRIAL Al_2O_3 WITH GLASS PHASE CHEMISTRY IN THE CaO-Al_2O_3-SiO_2 SYSTEM

BY

SARAH C. WHIPKEY

A THESIS

SUBMITTED TO THE FACULTY OF

ALFRED UNIVERSITY

IN PARTIAL FULFILLMENT OF THE REQUIREMENTS
FOR THE DEGREE OF

DOCTOR OF PHILOSOPHY

IN

CERAMIC ENGINEERING

ALFRED, NEW YORK

MAY 2020

INVESTIGATING THE MICROSTRUCTURE EVOLUTION OF INDUSTRIAL Al_2O_3 WITH GLASS PHASE CHEMISTRY IN THE CaO-Al_2O_3-SiO_2 SYSTEM

BY

SARAH C. WHIPKEY

B.S. VIRGINIA POLYTECHNIC INSTITUTE AND STATE UNIVERSITY (2015)

SIGNATURE OF AUTHOR _____

APPROVED BY _____

DR. WILLIAM CARTY, ADVISOR

_____

DR. STEVEN TIDROW, ADVISORY COMMITTEE

_____

DR. HOLLY SHULMAN, ADVISORY COMMITTEE

_____

DR. TIMOTHY KEENAN, ADVISORY COMMITTEE

_____

DR. ALEXIS CLARE, CHAIR, ORAL THESIS DEFENSE

ACCEPTED BY _____

DR. GABRIELLE GAUSTAD, DEAN
KAZUO INAMORI SCHOOL OF ENGINEERING

ACKNOWLEDGEMENTS

I would like to express my gratitude for all the lessons I've learned during my years in Alfred, both good and bad. In a short summation, it's been a strange and intriguing adventure, but I've grown and accomplished more in my time here than I ever thought possible.

I'd also like to thank my advisor, Dr. Carty for his support and encouragement through the last few years, as well as all those in Alfred who have helped me along the way. I won't exhaust the page with a list, but I anticipate those of you who belong on it know who you are. Thank you also to my parents and family for your support (and patience) as I've successfully completed the Job Avoidance Program that is graduate school. I know there have been countless times when things have been stressful, but you have always been there to lend help or encouraging words when I needed them. It has never gone unnoticed or unappreciated.

And since it's been 15 minutes, I'd like to thank my officemates and fellow ABC crew members, who have been more supportive and helpful in keeping my attention (and sanity) in check than they can ever know. I'd also like to gratefully acknowledge Alex's College Spot, for the many encouraging conversations and motivational libations I've enjoyed during my time in Alfred:

"This must be Thursday,' said Arthur to himself, sinking low over his beer. 'I never could get the hang of Thursdays."

-Douglas Adams, *The Hitchhiker's Guide to the Galaxy*

TABLE OF CONTENTS

LIST OF TABLES

Page

LIST OF FIGURES

Page

ABSTRACT

While extensive research has been performed on sintering of high purity alumina (>99.9%), the role of liquid phase properties on microstructural evolution of industrial Al_2O_3 (88-98% Al_2O_3) has been studied to a limited extent. This study investigates the microstructure evolution of industrial Al_2O_3 (99.8%) sintered with glass phase chemistries in the CaO-Al_2O_3-SiO_2 **(**CAS) system. Two ancillary results demonstrate: (1) industrial Al_2O_3 contains significant agglomeration after processing which can be removed via either wet milling or with a sedimentation technique, and (2) optimized etching conditions for Al_2O_3 with significant glass phase necessitate a two-part chemical-thermal etch for imaging of Al_2O_3 grains.

Al_2O_3 samples were created with glass compositions within the CAS system of varying SiO_2:CaO ratios and compared to samples of as-received Al_2O_3, with no additional glass forming additives. A statistical Design of Experiments (DOE) was used to investigate the validity of statistical analysis to empirically model densification with varying glass phase compositions. The relative significances of sintering time, temperature, and Al_2O_3 levels were determined for each composition system. It can be concluded that full factorials more completely represent densification in liquid-phase sintered systems than partial factorials due to the asymptotic nature of densification curves.

It was observed that the SiO_2:CaO ratio strongly influenced both densification and grain size under identical sintering conditions, and these behaviors can be grouped by the relative ratios of SiO_2:CaO in the system (according to SiO_2:CaO >1, ≈1, and <1). The compositions of the glass phases and secondary phase formation can be predicted based on the established Glass Formation Boundary approach to sintering. Al_2O_3 grains were observed to exhibit normal grain growth in all samples; however, significant secondary crystallization occurred with increasing CaO content, which limited the growth of Al_2O_3 grains. The average grain size of Al_2O_3 grains increased with increasing CaO content until the SiO_2:CaO ratio fell below 1:1.5, where excessive secondary phase formation occurred and reduced the average Al_2O_3 grain size.

1. INTRODUCTION

1.1 Motivation

While extensive research has been conducted on sintering of ultra-high purity Al_2O_3 systems (>99.9%), more than 90% of industrial Al_2O_3 applications use powder derived from the Bayer-process. This process produces a comparably lower purity Al_2O_3 derived from bauxite (99.0-99.9%), the main benefit being reduced production cost compared to the ultra-high purity powder.[1] In addition to impurities inherent from the Bayer-process, polycrystalline ceramics such as Al_2O_3 are typically sintered with supplementary oxide components added to the system (e.g. CaO, Na_2O, SiO_2, MgO), which melt at lower temperatures than the bulk ceramic and form a liquid phase.[2] MgO represents a special case, as it is typically added to Al_2O_3 with the intention of hindering abnormal grain growth and its influence has been extensively discussed; however, its role as a sintering mechanism is still a topic of debate.[3-8] Liquid phase sintering allows for densification at arguably faster times and lower temperatures than is otherwise possible using high purity systems.

The chemistry of the liquid phase has previously been demonstrated to have a strong influence on densification and grain growth in high purity Al_2O_3.[9-20] These effects, however, has not been well described for industrial systems with significant liquid phase, resulting in a substantial gap in understanding for the sintering behavior of Al_2O_3. The goal of this thesis work is to bridge the gap of microstructural evolution of Al_2O_3 between well-described high purity systems (>99.9%) and those commonly used in industrial practice for applications such as high voltage electrical insulators, spark plugs, and refractories (88-98%). A greater understanding of the microstructural evolution of these systems is critical, as properties such as densification and grain size are known to strongly influence macroscopic properties such as strength, electrical resistivity, and thermal conductivity.

1.2 Sintering Theory of Polycrystalline Ceramics

There are three main types of sintering processes: solid state sintering, viscous sintering, and liquid-phase sintering. Polycrystalline ceramics are typically sintered in the presence of a liquid phase, as additives and impurities present in the body melt at lower temperatures than the bulk ceramic, which then form a liquid.[2] This liquid phase allows for ceramics to be sintered at lower temperatures and with faster densification rates than would otherwise be possible without the liquid phase present.[21] Out of the six sintering mechanisms for polycrystalline materials, only grain boundary diffusion and lattice diffusion (from grain boundaries to pores) contribute to densification for polycrystalline ceramics.[22]

Figure 1.1 demonstrates the evolution of a powder compact during the three stages of liquid phase sintering. Stage I involves the redistribution of the liquid formed by the melted additives and rearrangement of the solid particles due to capillary stresses from the wetting liquid. In Stage II, densification and grain shape changes occur due to a solution-precipitation process of grains through the liquid phase. Densification can occur via either contact flattening or Ostwald ripening. During contact flattening, compressive capillary forces on particles from the surrounding liquid phase increase solubility at the particle-particle interface. Mass transport then occurs away from this contact point, resulting in a flattened interface between grains. Ostwald ripening, when it occurs due to liquid phase sintering, involves smaller grains dissolving into the liquid phase and then re-precipitating onto larger grains.[2]

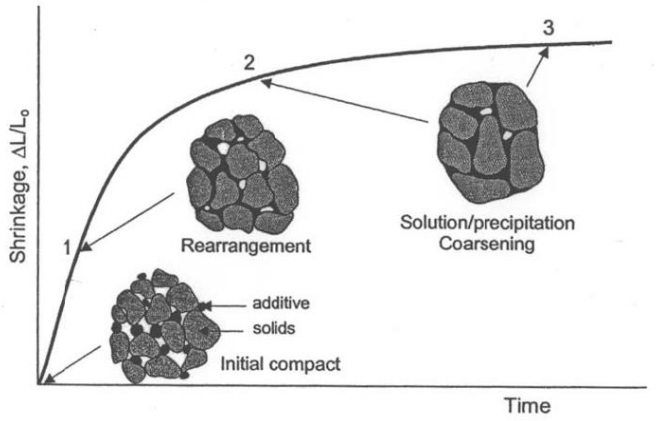

Figure 1.1. Evolution of a powder compact during liquid-phase sintering, demonstrating the three stages. Reprinted from Rahaman.[2]

The final stage of liquid-phase sintering is dominated by particle coarsening and is driven by the removal of isolated pores in the liquid. During the final stage of sintering, if discontinuous grain growth occurs before theoretical density is achieved, this process results in "trapped" closed pores, which prevent the system from fully densifying.[3] This failure to reach theoretical density is believed to be due to non-diffusing gas being trapped within the discontinuous pores.[3] This phenomenon is often observed when sintering temperatures are high enough to initiate rapid grain growth (i.e. coarsening) before full density is reached. Thermodynamic and kinetic factors which need to be considered during liquid-phase sintering include the wetting and spreading of the liquid, the dihedral angle between the liquid and grain boundary interfaces, the grain size and shape, the solubility between the liquid and solid species, and capillary forces from the liquid.[2, 23]

Both densification and grain size have been indicated to strongly influence macroscopic properties of materials, such as strength and electrical resistivity. Because dense, ceramic bodies with small, uniform distributions of grain sizes are often desired for improved material properties, a variety of processing techniques have been used to produce controlled microstructures with high densities and small grain sizes. These methods can include sintering under an external pressure, adding dopants to inhibit accelerated grain growth, and manipulating sintering rates and conditions for desired microstructures.[21] Microstructural inhomogeneities caused by poor processing result in densification gradients which can induce residual stresses in a material and reduce its overall quality and performance.[2]

1.3 Sintering of Alumina (Al_2O_3)

1.3.1 Sintering Behavior of High Purity Al_2O_3

Al_2O_3 is one of the most commonly used and widely studied ceramics, as it exhibits a versatile range of properties such as high electrical resistivity, low chemical reactivity, high hardness, and high melting temperature. This prevalence does not mean, however, that the sintering behavior of Al_2O_3 is fully understood. Even with small impurity levels on the ppm scale, Al_2O_3 will sinter in the presence of a liquid phase, as impurities or additives with low solubility in Al_2O_3 will migrate to the grain boundaries and form a liquid.[24] These impurities can be a residual product of Al_2O_3 production, as is common in

Bayer-process Al_2O_3, or can be added intentionally to enhance densification or other properties. A range of work has demonstrated the complicated effects these impurities have on microstructural properties such as densification, grain growth rate, and grain shape.[17] The correlation between these constituents and resulting microstructures is important in order to also explain macroscopic properties of Al_2O_3 like mechanical strength.[9]

The grain boundary glass phase is the key to understanding the sintering behavior of Al_2O_3 with high amounts of impurities in the system. The compositional dependence of the viscosity of the glass phase is also critical, as a lower starting viscosity of the glass has been reported to require less glass present in order for particle rearrangement to happen for densification.[25] The viscosity of the liquid phase will also affect the distribution of the liquid phase and may change over time as Al_2O_3 dissolution occurs or reaction products form from the melt. If the viscosity of the liquid phase is too high during sintering, it is believed that this viscosity may actually hinder densification and grain growth behavior in Al_2O_3.[10] It is argued if gases are trapped in the glass phase during the final sintering stage, the pressure of the trapped gas will oppose the capillary pressure of the glass phase network and hinder densification.[13] Gas pressures can also continually increase during sintering due to the shrinkage of pores, gas being transferred between pores, and new gases forming from decomposition of impurities in the system.[26] These effects have experimentally been avoided by sintering Al_2O_3 systems in a vacuum, where full penetration of the glass into the grain boundary has been observed as compared to Al_2O_3 systems sintered in air, and constant densification rates have been measured.[27] The densification rate-limiting effect can be used to explain the non-linearity of densification rates in Al_2O_3 observed experimentally, where theoretical sintering models otherwise predict linear densification rates.[3-4]

Another point to consider with the grain boundary liquid phase is the distribution and chemical homogeneity of the liquid. It is believed that as the liquid redistributes, it will begin to fill the pores in order of smaller, lower coordination number to larger, higher coordination number.[13] Brydson et al. discovered stronger segregation of CaO at Al_2O_3 grain boundaries with SiO_2 and CaO tending to segregate in three grain junctions, which have been observed to be independent of the additive level.[14] The study claimed that Al^{3+} ions substitute in tetrahedral SiO_4 sites in the triple points; however, they move to

octahedral sites in the grain boundary films. It has also been reported that the Al^{3+} ion mobility is greater than O_2 mobility through the grain boundaries, which means the diffusion of Al^{3+} ions will be the controlling species for grain growth within the system.[28]

Grain growth in pure, undoped Al_2O_3 has been observed to be anisotropic in nature, noted to have large aspect ratios and long basal plane facets.[20] Bae and Baik demonstrated abnormal, or exaggerated, grain growth will occur in Al_2O_3 when the impurity content exceeds 10 ppm, which is well below typical impurity thresholds for industrial applications.[15] When MgO is added to the system, however, it is consistently reported to drastically reduce the tendency for abnormal grain growth in Al_2O_3.[4-6, 12, 18, 20, 29] One common explanation for this phenomenon is that MgO reduces the grain boundary velocity (i.e. mobility), which suppresses abnormal grain growth, as well as reduces the overall grain growth rate of the system.[5-6, 16, 30] Handwerker et al. suggested MgO increases the solubility of SiO_2 in Al_2O_3 due to charge compensation in the Al_2O_3 lattice.[6] Another explanation suggests MgO acts as a glass modifier in the liquid grain boundary phase, changing the viscosity and therefore changing the dissolution-reprecipitation kinetics through the liquid.[1] As demonstrated by these contradictory theories, a universally accepted mechanism by which MgO controls abnormal grain growth in Al_2O_3 is still a topic of debate.

While MgO is observed to inhibit abnormal grain growth in Al_2O_3, CaO and SiO_2 have oppositely been proposed to trigger abnormal grain growth.[11, 15, 20, 31-35] This effect is suggested to be caused by lowering the interfacial energy of grain boundaries when CaO or SiO_2 are present.[9] These opposing effects can be observed in Figure 1.2, comparing an Al_2O_3 microstructure doped with CaO and one doped with MgO of similar levels. The CaO additive induces the growth of large, impinging abnormal grains compared to the more equiaxed grains in the MgO-doped case exhibiting normal grain growth. Ca^{2+} ions have also been demonstrated to preferentially segregate to basal planes of Al_2O_3, resulting in a non-homogeneous chemical distribution around grains, which may promote abnormal grain growth and, as will be discussed, secondary phase formation in these regions.[36-38]

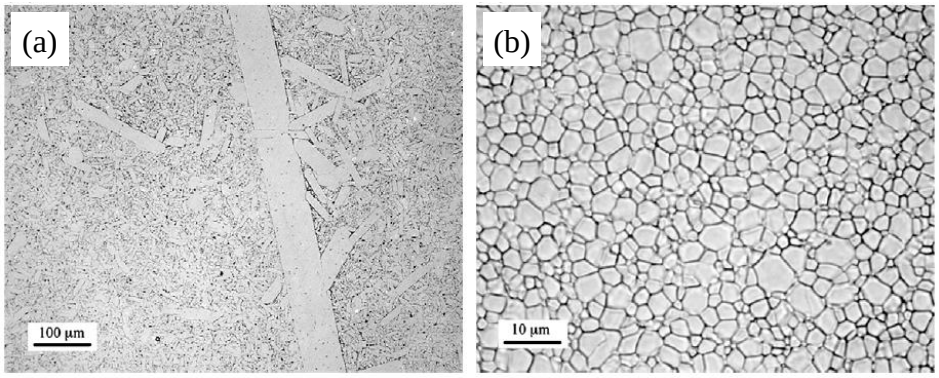

Figure 1.2. Optical micrographs of (a) CaO-doped Al_2O_3 annealed at 1750°C and (b) MgO-doped Al_2O_3 annealed at 1700°C.[39]

Ahn et al. investigated the effects of the ratio of $CaO:2SiO_2$ in Al_2O_3 in concentrations of 250-1000 ppm (0.025-0.1 wt%).[17] They observed that both the onset of abnormal grain growth and grain size were significantly affected by the liquid content even at minute levels. A larger grain size and higher aspect ratio grain (i.e. greater abnormal grain growth) were found in the systems with less liquid phase, while smaller grain size and aspect ratios were observed with greater liquid content. It was also reported that the amount of additives necessary to initiate abnormal grain growth in this Al_2O_3 system was about the solubility limit of each species in Al_2O_3 (300 ppm for SiO_2 and 30 ppm for CaO). These findings experimentally compliment those of Bae and Baik, who claimed that a glass phase will form when the solubility limit of the impurities in Al_2O_3, are exceeded. They experimentally determined the solubility of SiO_2 and CaO in Al_2O_3 to be 100 and 20 ppm, respectively.[15]

In addition to the importance of impurities controlling the glass phase composition and abnormal grain growth in a system, secondary phase formation is also of concern due to introduced stresses from thermal expansion differences between phases. If the solubility limit of the impurities and Al_2O_3 in the liquid phase is exceeded for a given temperature, the excess will precipitate as secondary phases in the grain boundaries.[9] It has been determined experimentally that once secondary crystallization begins, the densification of the system will likely be reduced by one of, or a combination of, the following four mechanisms: (1) an increase in the glass viscosity due to a change in composition; (2) a decrease in interfacial reaction due to decreased liquid content; (3) a reduction in the solution-reprecipitation process by coating the grains with the crystallized phase; or (4)

creation of a percolating crystalline network which restricts shrinkage during sintering.[40] A large variety of crystalline phases have been reported to form at the grain boundaries of sintered Al_2O_3 when combined with various additives (K_2O, Li_2O, Na_2O, MgO, CaO, SiO_2, Y_2O_3), which are summarized elsewhere.[41] These observations of secondary phases formed, however, do not always agree with those predicted by equilibrium phase diagrams and thermodynamics.[14, 40, 42-44] Due to the conflicting influences on microstructure evolution of additives such as those discussed, interaction effects between additives like SiO_2 and alkaline earth oxides (MgO, CaO, etc.) on the sintering behavior of Al_2O_3 have not been previously well-described.

1.3.2 Grain Boundary Complexion Models for Al_2O_3

Significant research has been completed over the last decade to explain the microstructural evolution of Al_2O_3 based on six identified grain boundary interface complexions that can exist within a polycrystalline system during sintering, as illustrated in Figure 1.3.[45-50] These complexions are considered grain boundary "phases", as they have a distinguishable volume within the grain boundary; however, they differ from a traditional phase because they cannot exist without the interface of the two crystals.[47] Because the interfaces such as grain boundaries and grain boundary phases typically have much higher mass transport rates than the bulk material, this work claims the interfaces present will essentially control the macroscopic properties, even at low volume fractions compared to the bulk.[46] For Al_2O_3 systems, this work suggests interfaces between Al_2O_3 and glassy grain boundaries, including any secondary crystallization in the grain boundaries, are of critical importance to understand in relation to microstructure evolution.

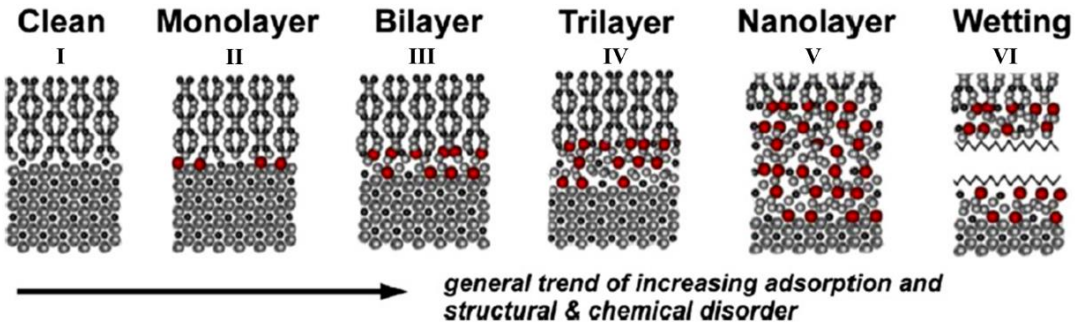

Figure 1.3. The six Dillon-Harmer complexions in order of increasing solute adsorption.[45]

The work of Dillon et. al. has attempted to describe the way complexions form in regards to phase boundaries and precipitation.[39] They found a correlation between the activation energy for precipitates to form and the temperature at which grain boundary complexions take place. According to their work, additives that promote a single complexion will cause normal grain growth, while additives that have multiple complexions with varying mobilities at one temperature will experience abnormal grain growth. This concept is used to describe the opposing effects of MgO and CaO in Al_2O_3, despite both components being divalent cations which segregate to grain boundaries upon sintering. The lower order complexions induced by the addition of MgO have been found to have lower mobilities and induce normal grain growth, whereas the additional of CaO supports multiple, more disordered complexions on varying Al_2O_3 planes, resulting in abnormal grain growth.[46-48] Relating these phenomena to activation energy, the studies indicate that the lower activation energy process will dominate between complexion transitions and precipitation.

The complexion studies have investigated additives such as CaO and SiO_2 in relation to densification and grain growth of Al_2O_3; however, these investigations utilized high purity Al_2O_3 systems (99.995%) with dopants in the range of 30-500 ppm. While the complexion model is informative for transitions happening at grain boundary interfaces at low impurity levels, the model predicts that only the two highest order complexion transitions (V and IV) will be present in an Al_2O_3 system with impurity contents greater than a few wt%, yet, microstructural evolution using such high level impurities have not been investigated in detail.[45] Liquid-phase sintering theory predicts with larger concentrations of impurities, glass phases will wet grain boundaries uniformly (complexion VI); however, this is not always observed experimentally. The glass phase has been observed to accumulate in pockets within the microstructure, leaving very thin films of glass/liquid between Al_2O_3 grains, which more closely resemble complexions III-V. A further understanding of the correlation between grain boundary complexions and experimentally observed grain boundaries with significant glass phase is a critical step to more accurately describing microstructure evolution of Al_2O_3 systems.

1.3.3 Sintering of Industrial Grade Al_2O_3

Extensive research has been conducted on high purity Al_2O_3 systems (>99.9%), which are typically derived from compounds such as aluminum chloride ($AlCl_3$), ammonium alum ($NH_4Al(SO_4)$), or boemite (γ-AlOOH).[1] While this body of work has been informative, Al_2O_3 most commonly utilized in industry is derived from bauxite via the Bayer process, resulting in a lower purity Al_2O_3 (99.0-99.9%).[51]

It is commonly observed in Bayer-process Al_2O_3 that sintered powdered systems do not reach full relative density. This observed trend is proposed to be due to large agglomerates inherent in the powder synthesis process, which pin pores during sintering and prevent full densification. For typical industrial-grade Al_2O_3, hard agglomerates can be reduced or removed by subsequent processing such as milling after production. The detection and elimination of these agglomerates and their effects on densification behavior will be discussed in Chapter 6. Despite a lower purity and less desirable powder uniformity as shortcomings of Bayer-process Al_2O_3, their significantly lower cost compared to powders synthesized through other methods leads to their prevalent use in industry.

In addition to impurities present from powder synthesis, industrial Al_2O_3 is frequently sintered using a combination of additional liquid-forming components (88-98% Al_2O_3), including but not limited to SiO_2, Na_2O, K_2O, and CaO. These liquid-forming constituents have been observed to interact and influence sintering behavior in complex ways.[15-20] Herein exists a significant fundamental lack in understanding of the sintering behavior of Al_2O_3.

Two relatively recent studies have begun to bridge this gap in understanding, focusing on industrial-grade Al_2O_3 produced via the Bayer process.[52-53] Both studies demonstrated that the composition of the liquid grain boundary phase significantly affects diffusion behavior and therefore the densification and grain growth behavior of Al_2O_3. Further, these works only investigate Na_2O and SiO_2 impurities at concentrations inherent in Bayer process Al_2O_3 powder on the ppm scale. Frueh et al. conclude that the rate of densification of an Al_2O_3 system doped with up to ~1600 ppm of various Na_2O:SiO_2 ratios will be controlled by either the interface reaction between the grain boundary liquid and Al_2O_3 grains, or by diffusion of Al^{3+} ions through the liquid grain boundary.[53] These studies are moving in the right direction, but are still far removed from industrial Al_2O_3 systems

for applications such as high voltage electrical insulators and high temperature refractories, which are typically sintered in the presence of significant liquid phase (4-15 wt%).[53]

Powell-Dogan et al. investigated eleven commercial Al_2O_3 products of 96 wt% with varying levels of SiO_2, MgO, CaO, and Na_2O.[43, 54-55] This study discovered that while the glass-forming additives do form a continuous liquid phase, the boundaries are not evenly wetted, indicating a significant difference in interfacial energy between the crystal-crystal and crystal-glass interface. The study reports as many as eight different crystalline phases forming in the grain boundaries, which is informative but also increases the complexity of associating direct correlations of additive contents with microstructure evolution. Because of the complicated mechanisms within these systems, the role of specific liquid phase compositions on densification and grain growth of Al_2O_3 during sintering is not well understood.

1.3.4 The Glass Formation Boundary Approach to Sintering Al_2O_3

Lam previously described the glass formation boundary (GFB) approach to predicting reaction products and glass phase compositions within the CaO-Al_2O_3-SiO_2 (CAS) system.[41] The GFB theory was developed from the Seger method for predicting glaze textures in porcelains by representing the chemistry of the glass oxides as molar ratios of the sum of total flux in the system (R_2O+RO) to SiO_2. The GFB approach allows for the prediction of glass compositions and secondary phase formation during sintering of industrial Al_2O_3. This approach succeeds where other methods based on equilibrium conditions and phase diagrams/cooling path analysis have not fully been able to describe these systems.[41, 56-58]

Traditional glass theory defines glass formation as dictated by the rate of cooling in order to prevent crystallization and maintain a glassy, disordered structure.[59] In realistic industrial systems, however, cooling rates are often limited by furnace capabilities and thermal shock restrictions, resulting in typical rates of 1.7-0.12 K/sec rather than quenching.[41] These slower cooling rates imply a comparatively smaller compositional range of glass formation compared to quench-cooled systems.[60] The GFB for the CAS system (Figure 1.4) illustrates where compositions will intrinsically form a glass when cooled at industrial cooling rates under ambient pressure (to the left of the boundary). Glass

compositions which fall outside the boundary (to the right) will crystallize phases within the corresponding compositional phase field. This method can be used to predict secondary phase formation in Al_2O_3 with various liquid phases, which is critical to further predicting mechanical, thermal, and electrical properties of these materials.

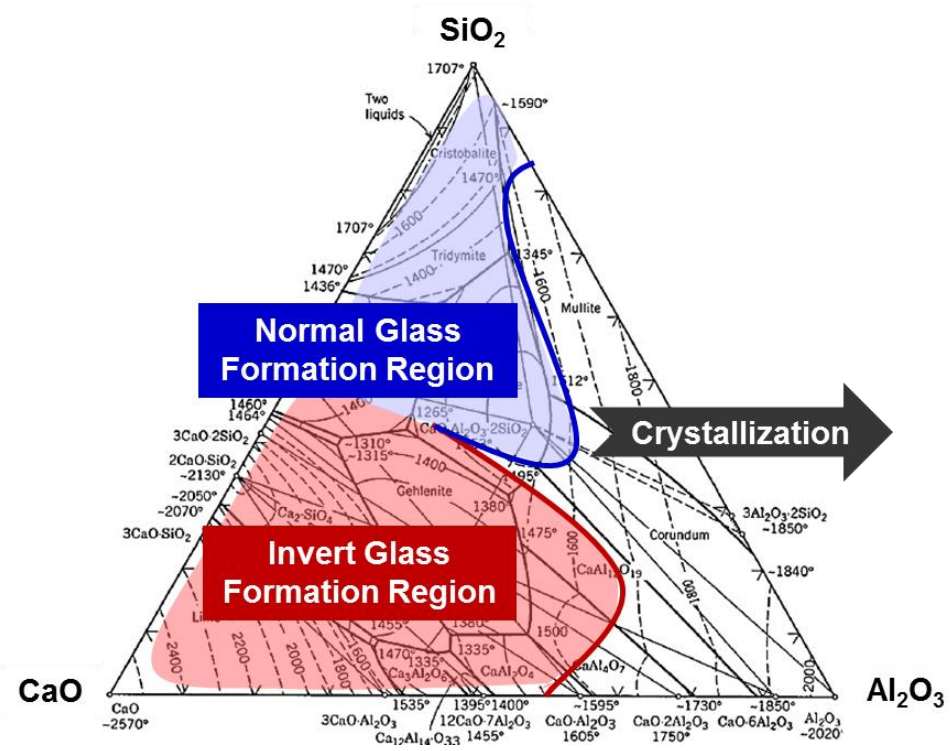

Figure 1.4. CaO-Al_2O_3-SiO_2 phase diagram with normal and invert glass formation boundaries identified, as proposed by Lam.[41]

According to the GFB theory for Al_2O_3, during heating the initial grain boundary chemistry will only depend on the impurities present, which melt at lower temperatures than the bulk, forming a eutectic liquid.[61] Differences in ionic size and charge will limit the solubility of impurity ions in bulk Al_2O_3, and Al_2O_3 will subsequently start to diffuse into the glass phase due to its diffusivity in the liquid.[61] Previous studies have demonstrated the dissolution of Al_2O_3 into the grain boundary liquid phase occurs very rapidly during sintering, within several minutes, and the Al_2O_3 dissolution level is in constant proportion to the total flux present in the glass phase (i.e. alkali and alkaline earth oxides) by the ratio of (R_2O+RO): Al_2O_3 = 1:1.19.[61-63] Assuming this dissolution level in the CAS system, known ratios of SiO_2:CaO can be combined with bulk Al_2O_3 to produce precise glass phase

chemistries. This will allow for an isolated analysis of how grain boundary chemistry and glass quantity contribute to microstructure evolution in industrial Al_2O_3.

For this work, glass boundary chemistries with SiO_2:CaO >1 are considered "normal" chemistry glasses. The corresponding glass formation boundary is represented by the solid blue line in Figure 1.4. Glass phase chemistries with SiO_2:CaO <1 are referred to as "invert" glasses (red line in Figure 1.4). The ratio inequality is specifically important, since invert glasses of this composition are differentiated from normal glasses by the calcium ions structurally acting more like glass formers than modifiers when Al_2O_3 is also present.[64] Invert glasses have been observed to exhibit dramatically different properties, such as lower glass transition temperatures and higher fragilities compared to normal glasses, so their influence on microstructure evolution compared to normal glasses is also expected to differ significantly.[57, 65-66] Compositional properties such as thermal expansion coefficient, density, and refractive index also vary simultaneously with SiO_2:CaO ratios, so it is expected these two glass types will also behave differently during sintering.[57, 67] "Boundary" glasses will be considered glass phases with SiO_2:CaO ~1, as pockets of glass where both normal and invert compositions may exist, resulting in unpredictable behavior of these "boundary" compositions in work to date.

The CAS system was chosen for this study because CaO and SiO_2 are common additives in industrial Al_2O_3 systems and significant sintering research has been performed with these additives in Al_2O_3 for comparison.[9-10, 14-15, 17-18, 25, 31, 33, 43-44] Many past works have also described the bulk forming ability of glasses with compositions in the CAS system, which can be compared to the results using the GFB method.[56-57, 65, 67-68] Other common impurities such as Na_2O and K_2O tend to migrate in electron beams during imaging and MgO can have significant solubility in the Al_2O_3 lattice.[69] While this initial study utilizes a simplified system compared to the variety of impurities in industrial Al_2O_3, it offers a preliminary view of how these liquid phases affect the microstructural evolution of Al_2O_3, which can later be applied to more complex systems.

1.4 Microstructure Analysis: Preparation and Measurement

1.4.1 Preparing Ceramic Microstructures for Microscopy and Grain Size Analysis

High purity oxide ceramics are often prepared for microstructure analysis after polishing by a thermal etch, where samples are heat treated 50-150°C below the sintering temperature for 15-30 min.[70-71] The etching temperature promotes grain boundary grooving without significantly altering the microstructure, resulting in improved image quality compared to an unetched sample.[70, 72] These effects are shown in Figure 1.5 for (a) an unetched and (b) a thermally etched Al_2O_3 sample. The goal of etching for grain size analysis is to select a technique to reveal the highest degree of delineation between grain boundaries, as poor delineation and resolution can lead to significant experimental error in measurement.[73] While a generalized thermal etch approach is sufficient for imaging high purity Al_2O_3, additional glass phase additives can introduce several complications.[74] These include secondary crystallization within sample grain boundaries and over-etching of the glass phase, where erosion of the glass from the surface leaves empty channels along grain boundaries. A detailed discussion on the optimization of etching conditions for polycrystalline ceramics containing a glass phase is presented in Chapter 2. Since distinctions are desired between Al_2O_3 grains for grain size measurements, a combined chemical-thermal etch is proposed in Chapter 2 to first remove the glass phase via a chemical etch, followed by a thermal etch to reveal grain boundaries, demonstrated in Figure 1.5(c).

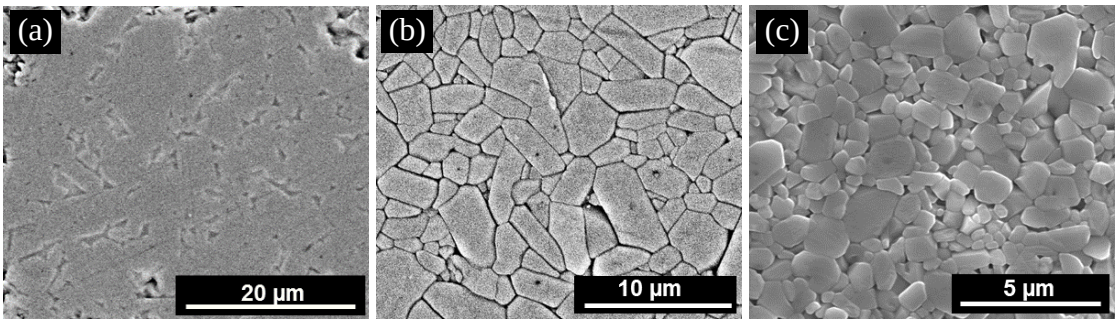

Figure 1.5. (a) 94 wt% Al_2O_3 unetched, (b) 99.8 % Al_2O_3 thermally etched, and (c) 92 wt% Al_2O_3 chemically etched in 10 wt% HF for 10s, then thermally etched 50°C below sintering temperature for 30 minutes.

1.4.2 Measuring and Representing Grain Size and Grain Growth Rates

Many methods exist to measure grain size in ceramic microstructures, including variations of the lineal intercept, planimetric, and circular-intercept methods, as well as the utilization of image analysis software to measure average grain size by two dimensional area.[75-76] Image analysis software provides a less biased measurement of average grain size than traditional intercept methods. This method, however, requires micrograph images have distinct grain boundaries with little contrast so binary image filters can be applied, which is not always feasible with liquid-phase sintered samples.

Most grain size measurement methods assume the microstructure is nontextured with equiaxed polyhedral grains and that only normal grain growth occurs.[77] By taking a random cross section of a microstructure, the measured average grain sizes are determined by a proportionality constant, as described by Mendelson.[77] Ideal grain growth for polycrystalline solids is often modeled using Equation 1:

$$G^m - G_o^m = Kt \qquad (1)$$

where G_o is initial average grain size, G is final average grain size, t is time, K is a constant with dependence on temperature and grain boundary mobility activation energy, and m is a grain growth exponent (usually accepted as 3 for liquid-phase sintered systems where grain growth is limited by solution-precipitation through the liquid).[21, 78] Polycrystalline ceramics exhibiting normal grain growth typically follow a log-normal grain size distribution.[77] Figure 1.6(a) is an example microstructure of Al_2O_3 with a normal grain size distribution. Abnormal grain growth can be detected in Al_2O_3 systems by variations from log-normal behavior, as observed in Figure 1.6(b). Variations in grain size distributions can be detected by plotting the logarithm of average grain size against a probability axis.[45] Figure 1.7 is an example of this grain size behavior for a recent sintering study performed on Al_2O_3.[45] Figure 1.7(a) demonstrates a log-normal grain size distribution with a linear trend, whereas Figure 1.7(b) exhibits two linear regions, indicating a bimodal grain size distribution and the presence of abnormal grain growth. All grain size data in this work is correspondingly represented on a probability axis in order to observe these trends.

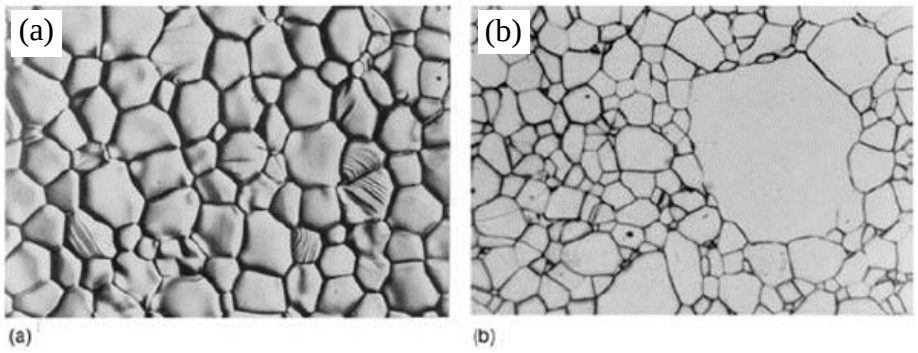

Figure 1.6. Microstructures of Al_2O_3 with (a) normal grain size distribution and (b) abnormal grain growth.[21]

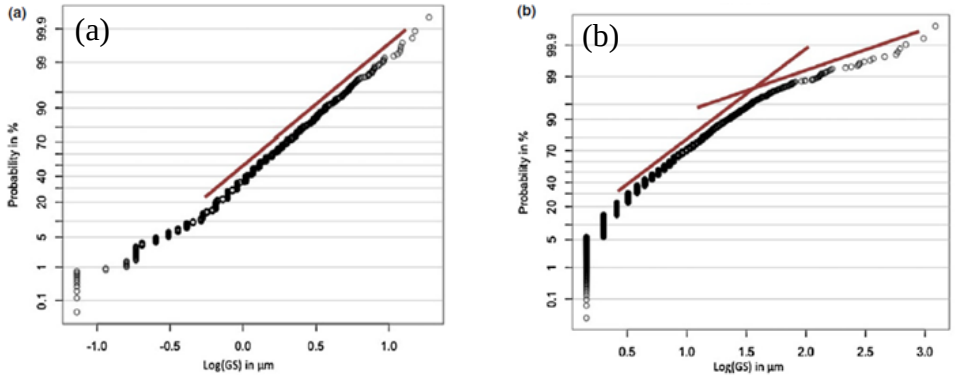

Figure 1.7. Probability plots of Al_2O_3 samples (99.9%) demonstrating (a) log-normal grain size distribution and (b) bimodal distribution indicative of abnormal grain growth.[45]

A possible source of error in representing grain size distributions can occur when multiple grain size distributions are present but not recognized, such as in Figure 1.7(b). If data falls on two intersecting lines, there may, in fact, be two distributions present, as may be the case for abnormal grain growth.[79] Distributions which may be observed to exhibit multiple grain size distributions in Al_2O_3 include duplex structures, which can be a result of either abnormal grain growth or the growth of a separate precipitated phase. There are two types of classified duplex grain structures: (a) agglomeration of small grain in a matrix of large grains, or the reverse, (b) a continuous dispersion of coarse or fine grains throughout the microstructure, as is most commonly observed in Al_2O_3.[73] While industry standards exist for measuring duplex grain size for single-phase systems, the only recommendations in the literature for multiphase structures involve measuring volume fractions via a point count method rather than measure the individual grain sizes of discrete phases.[73, 80]

1.5 Sintering Models: Experimental Design and Statistical Analysis

Statistical experimental design is used frequently in both academic and industrial settings and offers reliable methods for tasks such as monitoring production variability, designing and analyzing experiments, and optimizing response systems. Its applicability is wide-reaching, and when used correctly, reduces the time and effort necessary to learn important information about an experimental system. Without the help of experimental design, single factors would need to be analyzed individually in order to view their effects, and any interactions between factors would be difficult, if not impossible, to detect.[81]

For ceramists, the applicability of experimental design to sintering behavior is of particular interest, especially for modeling and predicting densification. Traditional sintering theory for ceramics such as alumina (Al_2O_3) presents densification as a process of competing forces between densification mechanisms and a driving force for grain growth during sintering. With these forces, the activated grain growth typically causes a rate-limiting effect on densification, rendering densification a non-continuous/terminating process.[3-4] Even more complications arise with the addition of constituents that form a liquid phase during sintering, which are typically inherent in some quantity in all industrially sintered ceramic systems. Some of these constituents are even added intentionally to increase densification at lower temperatures or purposefully influence other macroscopic properties of the material.

Past works have used experimental design methods, many including response surface methodology (RSM), to empirically model sintering systems of ceramics, as well as other materials.[81-86] RSM involves fitting a polynomial equation to experimental data in order to visualize a system with several influencing variables for a response.[87] The benefit of RSM is that it allows nonlinear experimental data to be described by a quadratic surface using statistical methods such as full factorial, central composite, Box-Behnken, and mixture designs.[88-89] Many past studies utilizing RSM, however, do not necessarily take into consideration the mechanisms responsible for sintering when analyzing the resulting models.[82-86, 90-91]

Full factorial designs with three factors at three levels each require 27 runs (without replicates) based on the rule $N=3^k$, where N is number of experiments and k is the number of factors (Figure 1.8(a)). Since minimizing experimental resources such as cost, time, and

energy consumption are often preferred, any experimental design which reduces the necessary run number is typically desired. Central composite and Box-Behnken designs are fractional 3k factorials which allow for enough observations to predict up to second-order effects without requiring the number of treatments for a full factorial. Because higher than second-order effects are not typically of concern for most practical experiments, these methods are frequently used to model physical systems.[89] For densification experiments utilizing RSM, the central composite design (CCD) is the most often utilized in the literature, and only requires 15 runs to analyze a three factor system (Figure 1.8(b)).[81, 84-86] However, since replicates are often required in order to estimate the error associated with repetitions, a CCD in practice typically requires 16-20 runs.[88]

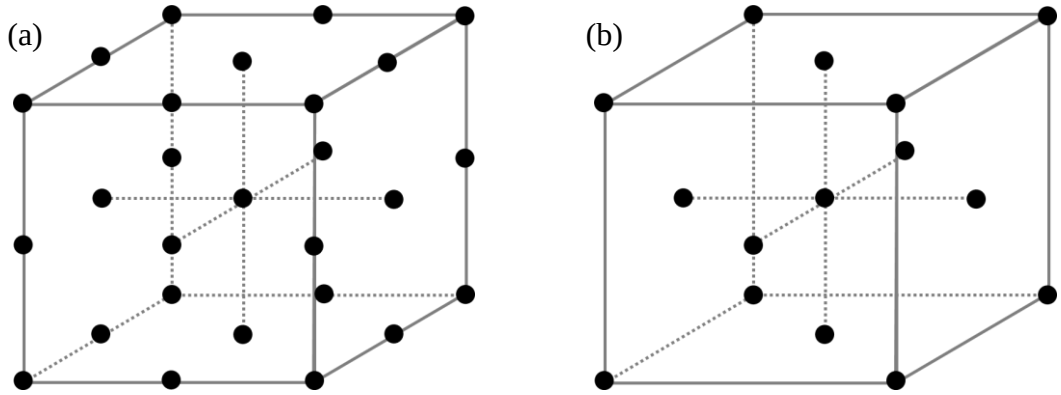

Figure 1.8. (a) 3^3 full factorial design and (b) Central composite design for three factors. Recreated from Mason et al.[89]

After the experimental treatment runs are completed, the method of least squares regression analysis is used to fit the experimental response vector to a mathematical model with the lowest residual error. It is assumed the error is randomly distributed about the mean response value and the errors are independent of each other.[88] To determine how well the fitted model describes the design space, analysis of variance (ANOVA) is used to compare the variation due to treatment conditions with the variation caused by random error of the response measurement.[88] This analysis uses several statistical methods to determine significant factors and the "goodness of fit" of the selected model, such as the p-test, F-test, lack-of-fit test, and the distribution of residuals.[92]

A common issue with using regression analysis as described involves relying too heavily on the generated empirical models without appropriate consideration of the

physical system being studied, where possible discontinuities may occur such a phase changes, physical limitations of factors or responses, etc.. Because of these limitations, empirical models generated in this way cannot necessarily be extrapolated outside of the experimental design space, and the physical limits of the system need to be closely considered.[93]

A typical approach to using DOE's for sintering studies is to use statistical software to generate a partial factorial design, often in the form of a central composite design. After completing all of the treatment conditions and producing the responses, a model is statistically mapped to the data based on the determined "goodness" of fit. After, one or more validation experiments are completed to compare the predicted model responses to experimental values, but some studies do not include or even consider completing confirmation runs.[94-95] If the confirmation runs are in relative agreement with the model predictions, the investigation typically ends without further scrutiny. The question then remains if this DOE approach is a reliable way to represent physical sintered systems, which has not yet been addressed.[81, 85]

There is limited critique in the literature of using partial factorial methods for statistical sintering studies beyond generating models from the initial experimental responses. Since the RSM and partial factorial designs are intended to represent continuous functions, if an experimental behavior, such as densification, does not follow continuous behavior, a partial factorial may not be sufficient to describe the system. The standard method to report density after sintering is to report the relative sample density to the theoretical full material density, as a percentage. Due to inherent defects in physical microstructures, such as agglomerates and pores which can never be fully eliminated in actual systems, ceramic systems in practice are rarely reported to reach 100% density, creating an asymptotic relationship when modeling densification. In addition, competing factors such as accelerated grain growth caused by "over sintering" a system may counteract typical fitting of statistical models. Figure 1.9 is an example of possible error introduced near the asymptotic density limit with partial factorial models, where the residuals of a ceramic densification partial factorial study begin to deviate after approximately 99% relative density.[85] It is proposed that for non-continuous densification models, a full factorial may be more appropriate to accurately model ceramic systems than

traditionally "efficient" partial factorial models. This work endeavors to critically investigate how this densification behavior can be applied to statistical experimental design methods to model and optimize densification of ceramic systems.

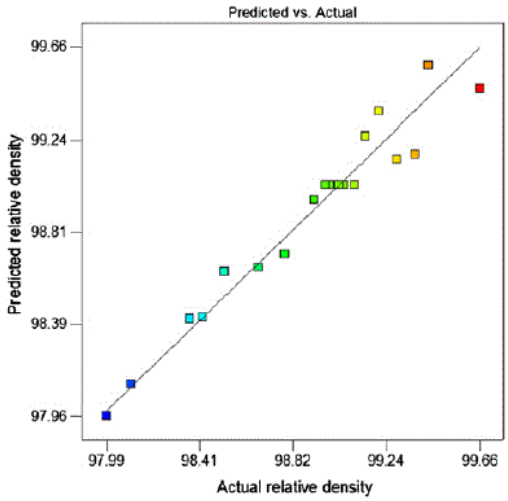

Figure 1.9. Predicted versus actual residuals for relative density for a partial factorial (CCD) sintering study of magnesia partially stabilized zirconia.[85]

2. OPTIMIZED ETCHING OF POLYCRYSTALLINE CERAMICS WITH A GLASS PHASE

2.1 Abstract

Chemical and thermal etching techniques are commonly used in ceramography to enhance microstructural features for microscopy. While thermal etching works well for high purity ceramic systems, when significant glass is included, thermal etching alone may not be appropriate or acceptable. Porcelain and industrial alumina (Al_2O_3) both contain significant amounts of glass phase (typically 4 to 30 vol% in Al_2O_3 and 40-60 vol% in porcelain), and it is proposed that the chemistries of these glasses are similar. Chemical etching of porcelain is common, but the images published in the literature are frequently over-etched, leading to erroneous interpretations regarding the role of quartz. When glass is present in the grain boundaries of alumina, thermal etching can sometimes cause the glass in the grain boundaries to "disappear," presumably by wetting and capillary action, and other times results in recrystallization of the grain boundary glass, obscuring the microstructure. Because of this concern, it is proposed that both chemical and thermal etching are necessary to prepare an industrial alumina microstructure for grain size measurements. In addition, it has been observed that chemical etching is sensitive to the residual stress in the glass phase, becoming more aggressive when there is residual tension in the glass.

2.2 Introduction

Etching is commonly used to enhance imaging of microstructural features for both porcelains and ceramics, such as grain boundaries, crystalline phases in a glassy matrix, grain orientation, and grain size distribution.[70] Several etching techniques have been applied to these systems, including chemical, thermal, plasma, electrolytic, and polarizing optical etching; however, chemical etching is traditionally used for porcelains, and thermal or chemical etching is most commonly selected for polycrystalline ceramics such as alumina (Al_2O_3).[70, 74, 96] Grouping industrial Al_2O_3 and porcelain together is logical since the glass chemistry in industrial Al_2O_3 and porcelain are similar, and the Al_2O_3 solubility limit in the glass is in a fixed molar ratio to the sum of the fluxes (R_2O + RO) at ~1.2 moles

of alumina per mole of flux.[58, 61-63] It is therefore proposed that the optimal chemical etching conditions for both porcelain and Al_2O_3 with a glass phase should also be similar. The difference between industrial Al_2O_3 and porcelains is consequently the amount of glass in the system, where sintered Al_2O_3 typically contains 4-30 volume percent (vol%) glass phase and porcelain systems contain 40-60 vol%.

The Al_2O_3 level referenced, such as "96%" Al_2O_3, describes the chemical mass percentage of Al_2O_3, but not the amount of corundum. Based on the rule of mixtures, and density levels of glass and Al_2O_3 at ~2.5 g/cm^3 and ~4.0 g/cm^3, respectively, the volume of glass is calculated to be 6.25 vol%. Al_2O_3, however, is not inert in the system and readily dissolves into the glass phase at a level of approximately 50 mass % (the exact amount depends, of course, on the ratio of flux to silica in the dopant addition). The volume of glass in the system is therefore more appropriately 9.4%. In short, there is a significant level of glass in an industrial Al_2O_3 sample so developing a chemical etching approach is appropriate.

In chemical etching, an aggressive acid (or base) is typically applied to preferentially attack the glass phase of a polished sample.[70] The reaction of the glass phase with the etchant introduces surface relief, which improves image contrast. Chemical gradients may result in preferential etching.[97] In addition, when all of the glass phase is removed, the distinction between pores resulting from sintering and pores created by the dissolution of the glass may become impossible without making assumptions.

Chemical etching methods for porcelain have traditionally used hydrofluoric acid (HF), and occasionally sodium hydroxide (NaOH), but often the etching conditions are not specified.[98-104] When the etching conditions are listed, it is common that the etching temperature is not specified. Table 2.I provides a summary of etching conditions for porcelain utilized in the literature (when reported).

Table 2.I. Recommended Literature Etching Conditions for Porcelain.

Temperature	Time	Chemistry	Ref.	Evaluation
100°C	20 minutes	50% NaOH	[105]	TEM
0°C	10 seconds	40% HF	[105]	TEM
Room Temperature (RT)*	20 seconds	10% HF	[106]	Optical
RT*	3 minutes	5% HF	[107-108]	Optical
RT*	30 seconds	1% HF	[109]	SEM
RT*	15 seconds	2.5% HF	[110]	SEM
RT*	4 minutes	15% HF	[111]	Optical
RT*	Unlisted	20% HF	[112]	Optical
RT*	60 seconds	15%HF	[113]	Optical
RT*	4 minutes	2 v/o HF	[114]	Optical
RT*	3 minutes	5% HF	[115]	Optical
RT*	60 seconds	5%HF	[116]	Optical
RT*	30 seconds	5%HF	[116]	Optical
RT*	120 seconds	10% Glacial Acetic acid	[116]	SEM
RT*	1 minute	10 vol% HF	[117]	SEM

*Room temperature etch is assumed; the etching temperature was not listed.

In the case of porcelain, the goal of etching is to illuminate the presence of mullite, consisting of primary, secondary, and tertiary (when corundum is present). The other microstructural features of interest are quartz grains, quartz dissolution rims, corundum (if added), and potentially cristobalite. The problem with etching porcelain, however, is that the coefficient of thermal expansion (C.T.E.) of quartz is significantly greater than the glass matrix, roughly 3x greater, and therefore the quartz particle and surrounding glass matrix are placed in radial tension and tangential compression.[118-119] In addition, and consistent with reduced chemical durability of glasses in tension, the glass matrix under such stresses will etch preferentially and more rapidly in these areas. While useful for demonstrating the role of tension (and compression) and identifying where these stresses are present, the consequence of the reduced chemical durability yields a strong potential to "over-etch" in the vicinity of quartz particles and cause the formation of large crevices (Figure 2.1). These

crevices around quartz particles have previously been used to incorrectly argue that porcelains are mechanically unreliable.[120]

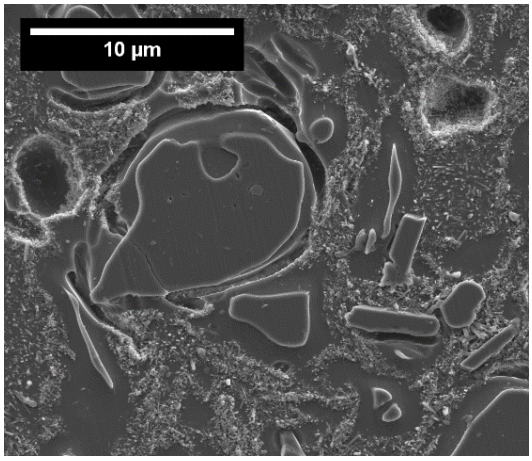

Figure 2.1. Porcelain microstructure etched in 20 wt% HF for 20 seconds at 0°C with large crevices around a quartz particle as a result of over-etching.

Corundum (Al_2O_3) is frequently added to porcelain to increase the strength and is also one of the most highly utilized industrial ceramics for applications such as spark plugs, refractories, wear parts, and electronic substrates. Previously reported thermal and chemical etching methods for polycrystalline ceramics, including Al_2O_3, have taken a pseudo-recipe approach, where etching conditions are recommended based on the behavior of high purity Al_2O_3 systems which do not contain significant amorphous phase. Published etching conditions for Al_2O_3 are summarized in Table 2.II, but these all ignore the presence of a unique, amorphous grain boundary phase.

Table 2.II. Recommended Literature Etching Conditions for Al_2O_3

	Temperature	Time		Ref.
Thermal Etch	1300-1400°C	15-20 minutes		[70]
	1500°C	20-30 minutes		[72]
	1100-1300°C	2 hours		[72]
	1350-1400°C	20 minutes		[97]
	1400°C	15 minutes		[97]
	1250-1500°C	0.5-4.5 hours		[121]
	Temperature	**Time**	**Etchant**	**Ref.**
Chemical Etch	250°C	5 to 600 seconds	85% H_3PO_4	[70, 97]
	Boiling	15-60 seconds	H_3PO_4	[72]
	Boiling	2-10 minutes	H_3PO_4	[72]
	20°C	15 minutes	10% HF	[121]
	230°C	2-10 minutes	H_2SO_4	[121]
	250°C	1-10 minutes	H_3PO_4	[121]

Thermal etching of sintered Al_2O_3 is typically conducted using a post-sintering heat treatment 50-150°C below the initial sintering temperature for 15-30 minutes.[70-71] The high temperature is intended to initiate grain boundary grooving that exploits the formation of an equilibrium dihedral angle at the grain boundary. Ideally, this subsequent heat treatment will not significantly alter the sample microstructure.[70] An example of this effect altering the grain appearance but not altering the microstructure is step bunching, which occurs on grain surfaces where atoms accumulate unevenly in grooves (Figure 2.2).

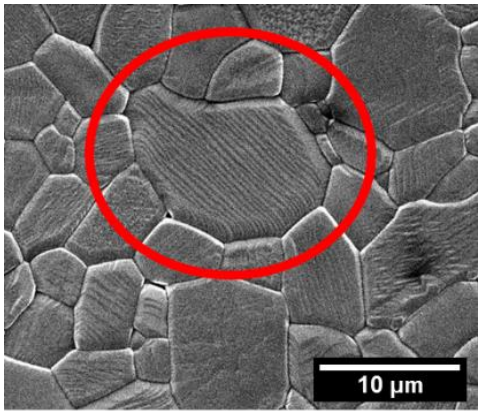

Figure 2.2. Step bunching observed in Al_2O_3 samples sintered at 1500°C for 3.2 hours, thermally etched at 1450°C for 30 minutes.

The thermal etch process results in a slightly elevated surface in the vicinity of the grain boundary, as the process removes material from the grain boundary to obtain the equilibrium dihedral angle, compared to the flat (equilibrium) surface of the polished grain.[122-123] The resulting surface relief between the elevated grains and grain boundaries provides the necessary contrast for scanning electron microscopes to image the grain boundaries and features such as grain size and secondary crystalline phases.[72] The need to thermally etch at a temperature that is scaled to the sintering temperature is because the grain size increases with increasing sintering temperature. With larger grains, the typical practice is to reduce the magnification to allow more grains to be imaged for grain size analysis. The amount of grain boundary grooving increases with increasing temperature, so with larger grains, and thus poorer resolution at lower magnification, a larger grain boundary groove is required, and a higher etching temperature is therefore necessary.[72, 124]

While a generalized thermal etching approach is typically sufficient for high purity Al_2O_3 (Figure 2.3(a)), the presence of significant amorphous phase introduces several complications.[74] One possible issue is the potential to over-etch the glass phase, in which the reduced viscosity of the glass phase, coupled with obvious wetting of the grain boundaries, results in the extraction of the glass phase from the surface via capillary action (Figure 2.3(b)). These interactions create vacant grain boundaries which may mimic the appearance of a pore. A second potential consequence is secondary crystallization on the surface of the sample, most often along grain boundaries (Figure 2.3(c)). Both of these effects can lead to erroneous conclusions about the microstructure being analyzed.

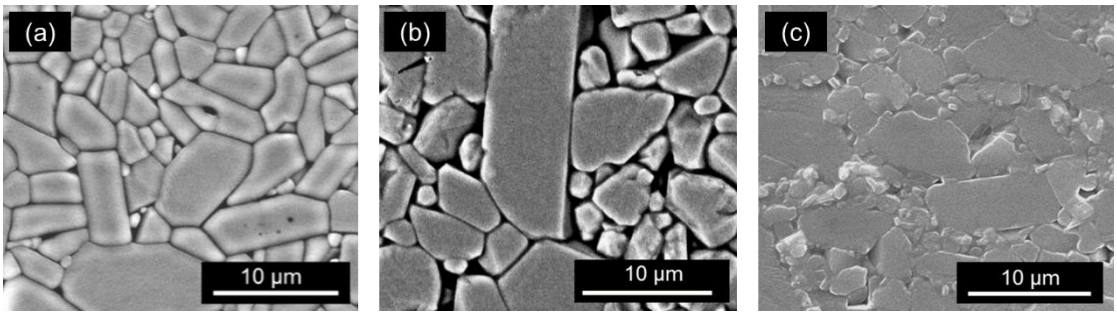

Figure 2.3. **(**a) 99.8% Al_2O_3 sintered at 1550°C for 10 hours and thermally etched at 1500°C for 30 minutes; (b) 85% Al_2O_3 (approximately 14% glass) sintered at 1550°C for 10 hours and etched at 1500°C for 30 minutes; (c) 86% Al_2O_3 (approximately 14% glass) sintered at 1480°C for 3 hours and etched at 1430°C for 30 minutes.

2.3 Materials and Methods

This study is divided into: (1) etching of porcelain (50-60 vol% glass phase) and (2) polycrystalline Al_2O_3 (6-30 vol% glass phase). The compositions of the glass phases in both the porcelain and the grain boundaries of polycrystalline Al_2O_3 samples are presumed to be comparable, with the molar quantity of silica (SiO_2) present being greater than the molar sum of the fluxes (R_2O + RO).

2.3.1 Porcelain Sample Preparation

Commercial quartz-based and alumina-based high-tension electrical insulator porcelains (Victor Insulators, Inc., Victor, NY) were used for the porcelain etching experiments. Porcelain bodies were extruded and evaluated as either glazed (single-fire) or un-glazed. The bodies were sectioned, mounted in epoxy, and polished to a 1 μm finish using SiC and diamond suspensions on nylon polishing cloths (MetLab Corp., Niagara Falls, NY). Samples were etched using the variable conditions listed in Table 2.III. After etching, the specimens were immersed in a calcium carbonate suspension to neutralize the acid, then rinsed and ultrasonicated. Sample microstructures were then analyzed via SEM (ESEM, Quanta 200, FEI Company, Hillsboro, OR).

Table 2.III. Chemical Etching Conditions Evaluated for Porcelain Microstructures

HF Concentration (wt%)	5, 10, 20
HF Temperature (°C)	0, 20
Exposure Time (seconds)	10, 20

2.3.2 Polycrystalline Alumina Sample Preparation

An industrial grade Al_2O_3 powder (99.8% Al_2O_3, CT 3000 LS SG, Almatis, Inc., Ludwigshafen, Germany) was combined with kaolin clay and calcium carbonate (EPK Kaolin, Edgar Minerals, Inc., Hawthorne, FL; Castle Carb 18, Oldcastle Industrial Minerals, Inc., Thomasville, PA) to generate samples with a SiO_2:CaO ratio of approximately 3:1. 30 vol% aqueous suspensions of Al_2O_3 were dispersed at 0.3 mg/m^2 using a NH_4-PMAA polyelectrolyte (Darvan C-N, Vanderbilt Minerals, LLC, Norwalk, CT) and slip cast into gypsum molds to produce discs approximately 4 cm in diameter.

Cast samples were dried at 100°C overnight and heated in air at 1550°C for 1.5 hours. Specimens were then ground and polished to a 1 μm finish (MetLab Corp., Niagara Falls, NY) and etched, either chemically and/or thermally.

The initial thermal etch experiments were conducted in a sample temperature range targeted around the estimated glass transition temperature (T_g) of the glass phase (approximately 780-830°C).[41, 65-66] Temperature increments were established using a gradient furnace over a total range of 570-1135°C, all etched for 30 minutes. Chemically etched samples were immersed in room temperature dilute HF acid solutions at concentrations of either 1, 5, or 10 wt% HF for 5 or 10 seconds (Sigma-Aldrich, St. Louis, MO). Samples were then neutralized after etching with calcium carbonate and ultrasonicated for 20 minutes. Microstructures were analyzed via SEM.

2.4 Results and Discussion

2.4.1 Porcelain Microstructure (approximately 50% glass phase): Chemical Etch

Figure 2.4 presents images of quartz porcelain microstructures etched with 10 wt% HF at 0 and 20°C for 10 and 20 seconds. No significant differences in etching behavior can be observed. At 20%, however, etching was aggressive, as illustrated in Figure 2.5. At 5 wt% solution (Figure 2.5(a)), the dissolution of the glass phase was minor and did not provide sufficient resolution to image mullite and quartz, while 20% HF created large craters in the vicinity of the undissolved quartz grains (2.5(c)). The over-etched microstructure presented in Figure 2.5(c) misrepresents the microstructure and therefore has the potential to generate erroneous conclusions about the role of quartz in porcelain. From these results, it is proposed that optimum etching conditions are obtained with a 10% HF solution for 10-20 seconds at 20°C (Figure 2.5(b)).

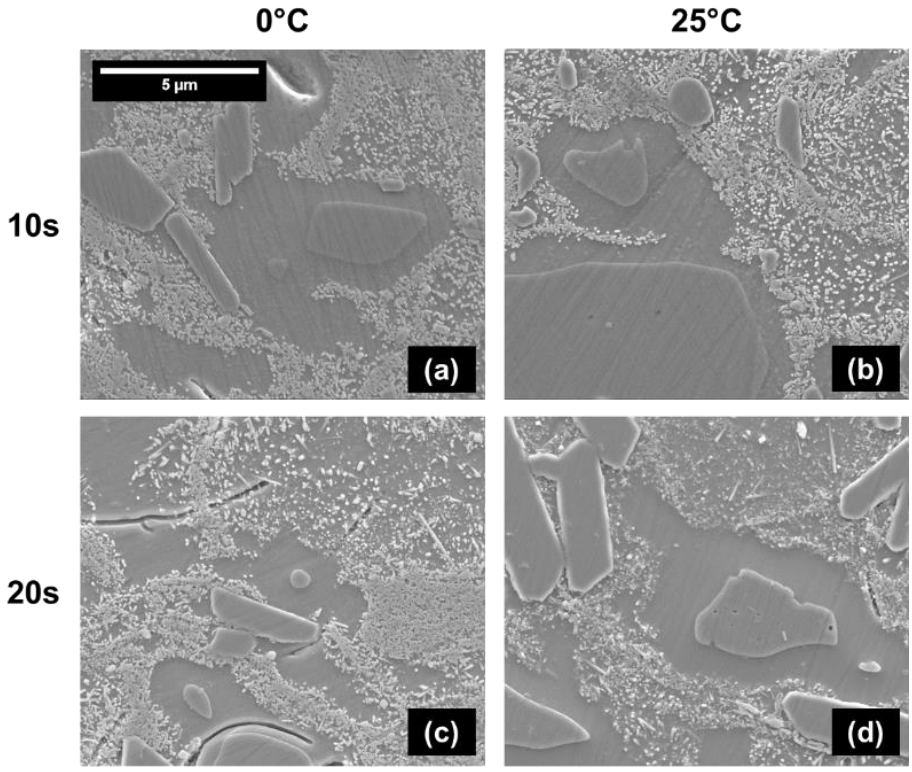

Figure 2.4. Quartz porcelain microstructures etched in 10 wt% HF for (a) 10 seconds at 0°C, (b) 10 seconds at 20°C, (c) 20 seconds at 0°C, and (d) 20 seconds at 20°C.

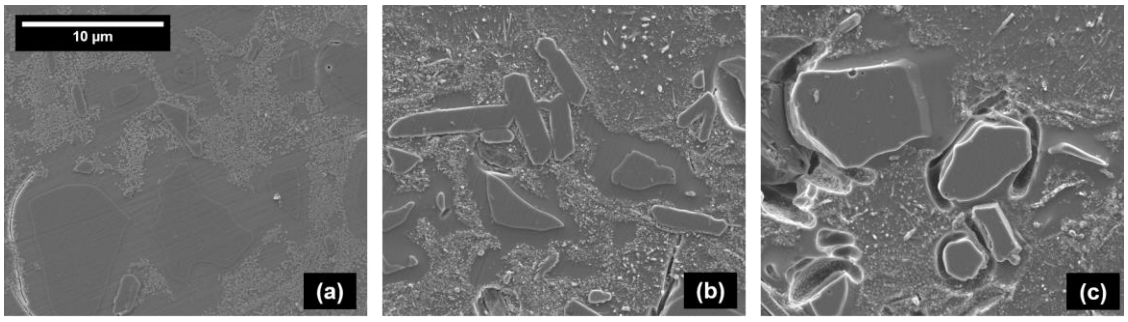

Figure 2.5. Quartz porcelain etched in (a) 5 wt% HF, (b) 10 wt% HF, and (c) 20 wt% HF for 10 seconds at 20°C.

2.4.2 Body-glaze Interfacial Tension and Enhanced Etching Phenomenon

If the proposed optimum porcelain etching conditions, 10% HF for 10 seconds, are used to etch polycrystalline Al_2O_3 microstructures, the amorphous grain boundary phase is completely removed, indicating over-etching. This over-etching is proposed to be due to residual stress (i.e. the glass in the grain boundaries being in tension). The coefficient of

thermal expansion (C.T.E.) of Al_2O_3 is roughly 3x that of the grain boundary glass, placing the grain boundary phase in tension, and therefore accelerating its dissolution. It is well established that glazes that well-fit a porcelain body have a lower C.T.E. than the body and are therefore placed in compression during cooling. Correspondingly, the underlying porcelain body is placed in tension. The maximum tension is located in the porcelain body just below the glaze surface.

Figure 2.6(a) demonstrates preferential etching of the body glass phase at the body-glaze interface for a glazed body. Figure 2.6(b) for comparison, displays etching of the bulk body. There are two interesting aspects to these figures: (1) the depth of the tensile region below the glaze is evident and indicates the residual tensile strain dissipates in a relatively short distance, and (2) there does not appear to be etching of the glaze. Figure 2.6(b) is at a higher magnification than Figure 2.6(a) and reveals the bulk body did etch but the extent of etching body is limited, particularly compared to the etching exhibited by the body in residual tension.

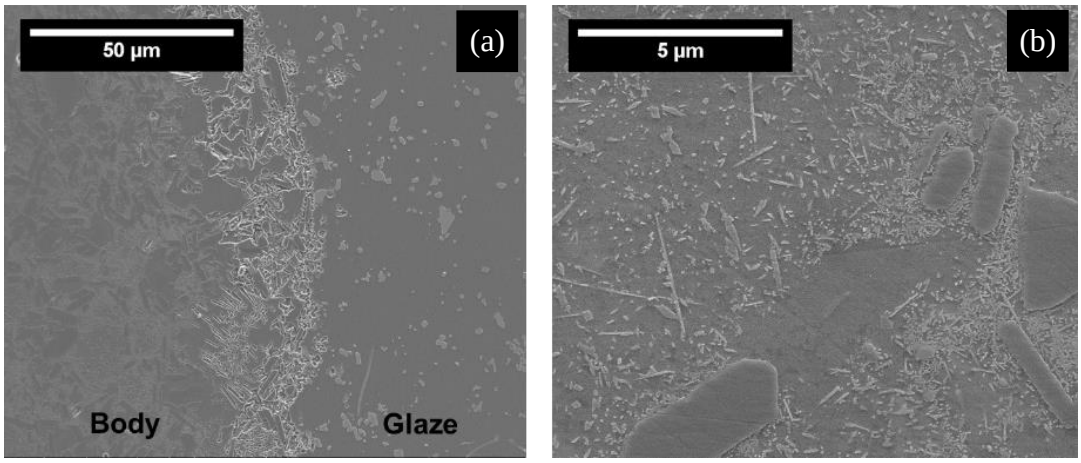

Figure 2.6. Porcelain microstructure (a) body-glaze interface and (b) body, chemically etched in 5 wt% HF for 20 seconds at 0°C.

2.4.3 Polycrystalline Alumina (approximately 8-14% glass phase): Thermal Etch

Figure 2.7 displays 88% Al_2O_3 samples thermally etched at various temperatures for 30 minutes after being sintered for 1.5 hours at 1545°C. Clear distinctions can be made between the glass phase and bulk Al_2O_3 grains in almost every case. The ideal definition between these two phases occurs at approximately 880°C, which is slightly above the

estimated glass transition temperature (T_g) of the glass phase (780-830°C).[41, 65-66] Unlike the apparent elimination of the grain boundary glass (Figure 2.3(b)), all of the specimens in Figure 2.7 still have glass present. This indicates that in the range of the T_g, the viscosity is too high to allow surface tension induced capillary action and extraction of the liquid phase from the grain boundaries. As the etching temperature increases (1125-1135°C), the grain boundary glass starts to crystallize. Crystallization of the glass becomes more obvious with higher glass levels (Figure 2.8). Specimens sintered at high temperatures and etched at a moderate temperature (Figure 2.8(a)) reveal the onset of crystallization at the grain boundaries. With lower sintering temperature the problem becomes unmanageable (Figure 2.8(b)) for a specimen sintered at 1480°C and then etched 50°C below the sintering temperature at 1430°C.

These results suggest that a thermal etch temperature selected close to the T_g of the grain boundary phase may provide a reasonable route for etching. The issue, however, is the need to be able to estimate T_g for the grain boundary glass. The second problem is that crystallization from a glass melt is strongly dependent on chemistry and temperature – if the composition of the glass phase can be identified, then it may be possible to estimate T_g. A more ideal route is proposed that first eliminates the amorphous grain boundary and then introduce a thermal etch to illuminate the grain boundaries.

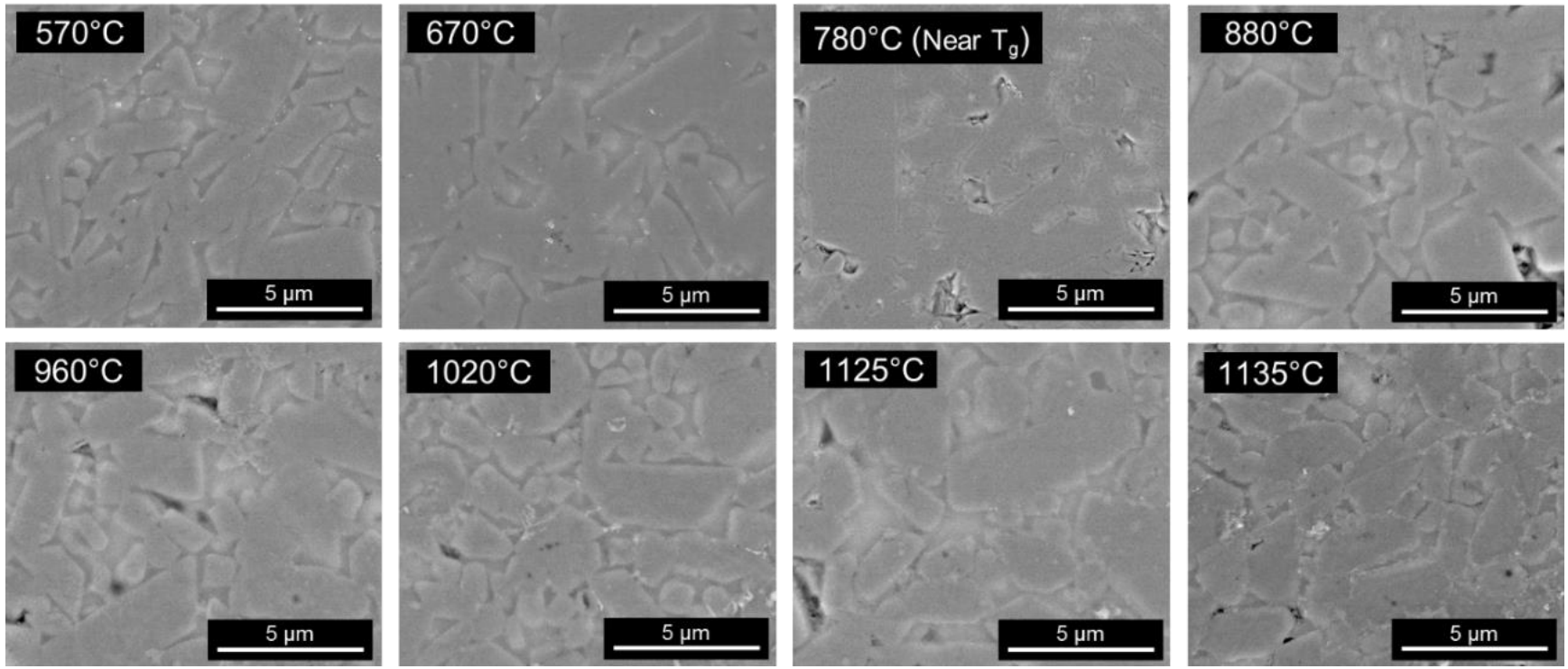

Figure 2.7. 88% Al_2O_3, 12% glass sintered for 1.5 hours at 1545°C and thermally etched for 30 minutes at various temperatures.

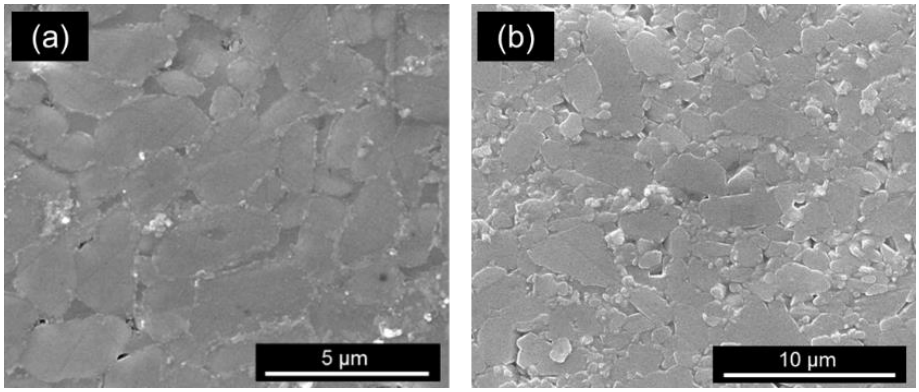

Figure 2.8. 86% Al_2O_3, 14% glass phase sintered at (a) 1545°C for 1.5 hours and etched at 1135°C for 30 minutes and (b) 1480°C for 3 hours and etched at 1430°C for 30 minutes.

2.4.4 Polycrystalline Alumina: Chemical Etch

Figure 2.9 presents microstructures of 88% Al_2O_3 sintered at 1545°C for 90 minutes, sectioned, mounted, polished, then chemically etched using various HF concentrations and times. Etching with 10% HF exposure for 10 seconds (Figure 2.9(a)) matched the optimum porcelain etching conditions previously discussed, but in this case the glass phase is completely eliminated, indicating the etch was too aggressive. From the observations regarding etching of glass with residual tension (Figure 2.6(a)) the grain boundary glass should be in tension. Based on the predicted chemistry of the grain boundary glass, it would be expected that the $C.T.E._{Alumina} \sim 2C.T.E._{Glass}$, so that on cooling, the Al_2O_3 grains contract away from the grain boundary phase, placing the grain boundary in tension. In such a situation, inter-granular fracture would be anticipated, because residual tension in the grain boundary would provide a preferred crack propagation pathway.

To avoid the elimination of the grain boundary glass, reducing the HF concentration and exposure time appears to resolve this issue (Figure 2.9(b) and (c)). With these etching conditions, the glass phase is still visible. It is clear, however, that in all of the chemical etching conditions shown in Figure 2.9, the resolution of the grain boundaries between Al_2O_3 grains is not evident. This means that if the sample is chemically etched to allow the glass in the grain boundary to be defined, it is still not feasible to conduct an automated grain size measurement – it will be necessary to draw the grain boundaries to delineate between grains. This observation is also consistent with the low temperature thermal etch conditions presented in Figure 2.7.

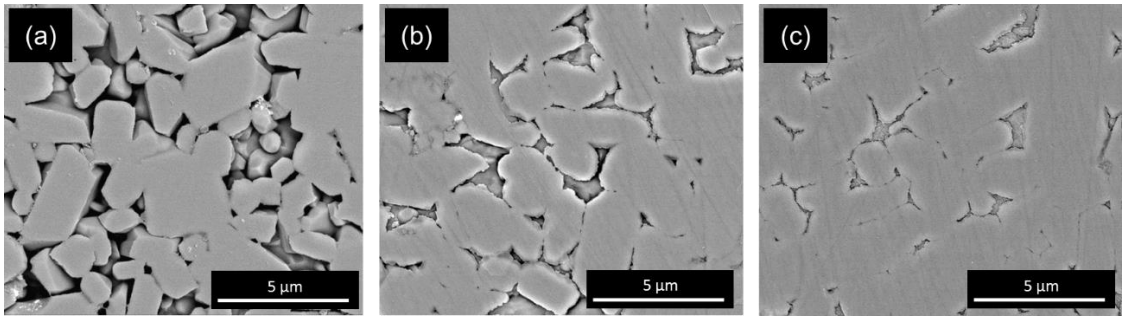

Figure 2.9. 88 wt% Al_2O_3 (approximately 12% glass phase) sintered for 1.5 hours at 1545°C and chemically etched in (a) 10 wt% HF for 10 seconds, (b) 5 wt% HF for 5 seconds, and (c) 1 wt% HF for 5 seconds.

2.4.5 Polycrystalline Alumina: Combined Thermal and Chemical Etch

In order to visualize distinct grain-grain interfaces, a combined chemical etch followed by a thermal etch is necessary, executed approximately 50°C below the sintering temperature. The glass phase is thus eliminated and the direct-bonded alumina grains exhibit grain boundary grooving to delineate the grain boundary. The results of this combined method are presented in Figure 2.10 for 92% Al_2O_3 sintered for 3 hours at 1500°C and 1550°C. The grain boundary glass has been eliminated by the chemical etch and the grain-grain boundaries are readily visible. The elimination of the glass in the grain boundaries (at the polished surface) eliminates the potential for secondary crystallization. The problem with this approach is that the pores remaining after sintering cannot be distinguished from the pores resulting from the elimination of the grain boundary glass. If it is necessary to account for both porosity and glass content, as opposed to solely measuring the grain size distribution in a sintered microstructure, it is therefore necessary to take images under different etching techniques and conduct a sequential microstructure analysis.

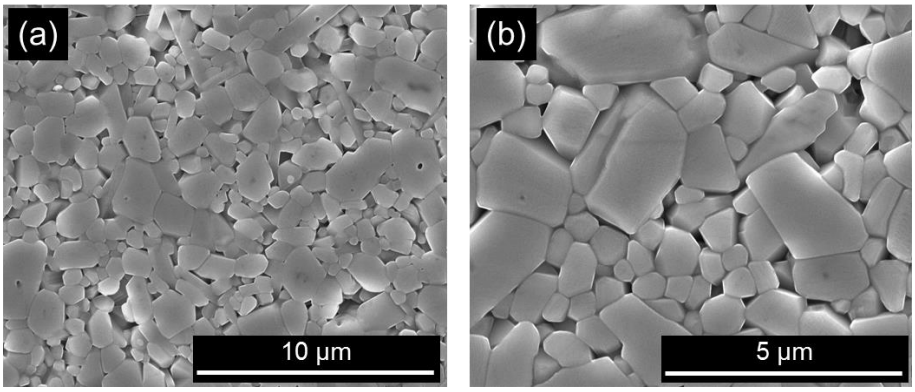

Figure 2.10. 92% Al_2O_3 sintered for 3 hours at (a) 1500°C and (b) 1550°C after a chemical etch (10% HF for 10 seconds) followed by a thermal etch (50°C below the corresponding sintering temperature for 30 minutes).

2.5 Conclusions

The optimum chemical etching conditions for industrial porcelain microstructures is determined to be 10% HF for 10-20 seconds at 20°C. It has been demonstrated that residual tension results in a preferential chemical etch, offering the potential for this technique to decorate regions of residual tension in a ceramic microstructure containing glass. For polycrystalline alumina containing measurable glass grain boundary levels, it is shown that a thermal etch can eliminate the glass in the grain boundary or cause secondary recrystallization of the grain boundary glass, obscuring the microstructure. If a chemical etch is undertaken to avoid recrystallization of the grain boundaries, Al_2O_3-Al_2O_3 grain interfaces are difficult to discern, making this approach of limited benefit. To obtain microstructures of sufficient quality to allow for automated grain size analysis, it is proposed that a combination of chemical and thermal etching be employed. If the porosity distribution, glass content, and the grain size distribution are required, it appears that imaging will be necessary between etching steps to allow all of these microstructural features to be documented.

3. INVESTIGATING THE APPLICABILITY OF STATISTICAL EXPERIMENTAL DESIGN TO CERAMICS SINTERED WITH A LIQUID PHASE

3.1 Abstract

Statistical experimental design methods such as response surface methodology have previously been used to model ceramic densification behavior during sintering. While abbreviated experimental designs are often used to study and optimize processing conditions, the question remains if these methods can accurately represent densification behavior of liquid-phase sintered ceramics such as alumina (Al_2O_3). A Design of Experiments approach has been used with industrial grade Al_2O_3 (99.8 wt%), combined with glass forming compositions in the CaO-Al_2O_3-SiO_2 system, to observe the significance of sintering time, temperature, and glass phase quantity on densification. Empirical models have been generated with both partial and full factorial designs to compare the applicability of these models to the experimental results. A time dependence was observed in the as-received Al_2O_3 and the sample group without additional CaO; however, densification was independent of time in all of the systems containing CaO. It is concluded that because densification follows asymptotic behavior, typical experimental design methods such as partial factorial designs may not be sufficient to represent densification in liquid-phase sintered systems, and full factorials that more completely map the experiment design space may instead be more applicable.

3.2 Introduction

Statistical experimental design is used frequently in both academic and industrial settings and offers reliable methods for tasks such as monitoring production variability, identifying critical variables, and optimizing process conditions. Its applicability is wide-reaching, and when used correctly, reduces the number of experiments and data necessary to acquire important information about a system. Without the help of experimental design, single variables need to be analyzed individually and variable interactions can be difficult, if not impossible, to assess.

For ceramists, the applicability of experimental design to sintering behavior is of particular interest, especially for modeling and predicting densification. Traditional sintering theory for ceramics such alumina (Al_2O_3), a common industrial ceramic, presents densification as a process of competing forces between pore elimination and grain growth during sintering. With these forces, grain growth typically limits the densification process, rendering densification an asymptotic, terminating process.[3-4] In addition, inherent defects in ceramic powders, such as agglomerates and their resulting trapped pores, which are never fully eliminated in practice, typically prevent microstructures from reaching 100% relative density. Even more complications arise with the addition of constituents that form a liquid phase during sintering, which are typically present in some quantity in almost all industrially sintered ceramic systems. Some of these components are added intentionally as dopants to facilitate densification or to influence other sintering properties.

Previous work has used experimental design methods, many including response surface methodology (RSM), to empirically model sintering systems of ceramics, as well as other materials.[81-86] RSM involves fitting a polynomial equation to experimental data in order to visualize a system with several variables.[87] The benefit of RSM is that it allows nonlinear experimental data to be described by a quadratic surface using statistical methods such as full factorial, central composite, Box-Behnken, and mixture designs.[88-89]

Full factorial designs with three factors at three levels each require 27 runs (without replicates) based on the rule $N=3^k$, where N is the number of experiments and k is the number of factors (Figure 3.1(a)). Since full factorials typically require a large number of runs, fractional factorial designs which reduce the number of runs necessary are commonly preferred, such as the central composite and Box-Behnken designs.[89] For densification experiments utilizing RSM, the Central Composite Design (CCD) is most often utilized in the literature, and only requires 15 runs to analyze a three factor system (Figure 3.1(b)).[81, 84-86] Since replicates are often suggested in order to estimate the error associated with repetitions, a CCD in practice typically requires 16-20 runs.[88]

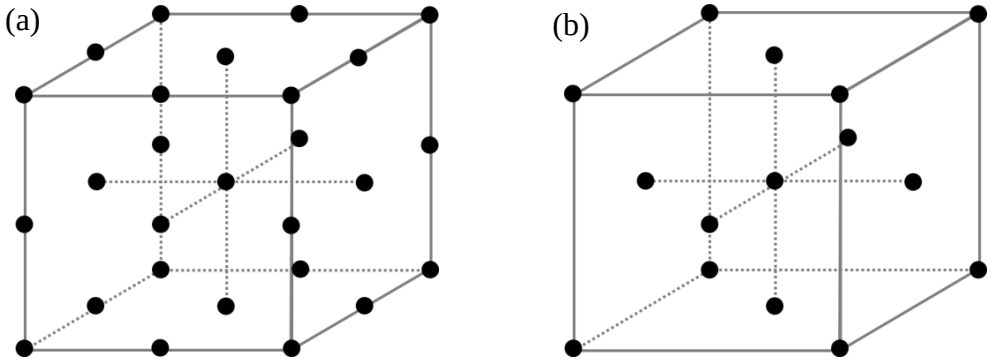

Figure 3.1. (a) 3^3 full factorial design and (b) Central Composite Design for three factors, recreated from Mason.[89]

After the experimental treatment runs are completed, regression analysis is used to fit the experimental response to a mathematical model with the lowest possible error.[88] To determine how well the fitted model describes the design space, analysis of variance (ANOVA) is used to compare the variation due to treatment conditions with the variation caused by random error of the response measurement.[92]

A typical approach to using DOE's for sintering studies is to use statistical software to generate a partial factorial design, such as a central composite design. After completing all required treatment conditions and producing the responses, a model is statistically fit to the data based on the determined "goodness" of fit. One or more validation experiments are then typically completed to compare the predicted model responses to experimental values; however, some densification studies do not include confirmations runs at all.[94-95] If the confirmation runs are in relative agreement with the model predictions, the investigation typically ends without further scrutiny.

A common issue with regression analysis as described involves relying too heavily on resulting empirical models without considering the physical system being studied, where discontinuities may occur such as phase changes or physical limitations of factors and responses.[93] Many past studies utilizing RSM, however, do not necessarily take into consideration the physical mechanisms responsible for sintering when analyzing the resulting models.[82-86, 90-91]

There is limited critique in the literature for using response surfaces based on partial factorial models, which assume continuous, non-asymptotic functions, to represent sintering systems, which in reality have non-continuous, asymptotic limits. It is proposed

that for asymptotic densification systems, a full factorial may be more appropriate to accurately model ceramic densification rather than "more efficient" partial factorial models.

An industrial Al_2O_3 system was selected for this work due to its common use as a liquid-phase-sintered (LPS) industrial ceramic, and the role of liquid phase properties on densification of industrial Al_2O_3 systems is not well understood.[15-20] The chemistry of the liquid phase has been demonstrated to strongly influence densification of Al_2O_3, but this effect has not been previously well described for industrial systems and is critical for understanding macroscopic properties such as strength, electrical resistivity, and thermal conductivity.[9, 13-14, 54] The CaO-Al_2O_3-SiO_2 (CAS) system was chosen for this study because CaO and SiO_2 are two common additives in industrial Al_2O_3, and previous work has developed methods to well-quantify the liquid (and corresponding glass) phase chemistry in this system during sintering.[41, 61]

3.3 Experimental Procedure

3.3.1 Sample Preparation

Aqueous Al_2O_3 suspensions (CT 3000 LS SG, Almatis, Inc., Ludwigshafen, Germany) were combined with kaolin clay (EPK, Edgar Minerals, Inc., Hawthorne, FL) and calcium carbonate (Castle Carb 18, Oldcastle Industrial Minerals, Inc., Thomasville, PA) to generate samples with controlled SiO_2:CaO ratios. The batched molar ratios of SiO_2:CaO, and overall Al_2O_3 levels were calculated based on ICP-ES and loss on ignition (LOI) data for the batched components (Table 3.I). The seven molar SiO_2:CaO target compositions studied are represented on the CAS ternary system in Figure 3.2. Samples with no additional glass-forming additives (as-received 99.8% Al_2O_3) were also analyzed as a benchmark.

The measured physical and chemical characteristics of the components used in this study are presented in Table 3.I. The Al_2O_3 powder was characterized via BET specific surface area (TriStar II, Micromeritics Instrument Co., Norcross, GA), He-pycnometry (AccuPyc II, Micromeritics Instrument, Co., Norcross, GA), and particle size distribution (SediGraph III PLUS, Micromeritics Instrument, Co., Norcross, GA). Chemical compositions were measured using inductively coupled plasma spectroscopy

(ICP-ES) (Mineral Laboratories Canada, Bureau Veritas Commodities Canada, Ltd., Vancouver, BC, CA).

Table 3.I. Powder Characterization of As-received Al_2O_3 and Batched Components

Al_2O_3 Powder Properties								
BET Specific Surface Area: 5.76 m^2/g				D_{50} Particle Size: 0.45 μm				
Density: 3.92 g/cm^3				D_{90} Particle Size: 1.89 μm				
Composition of Batch Components (wt%)	**Al_2O_3**	**SiO_2**	**CaO**	**MgO**	**Na_2O**	**K_2O**	**Fe_2O_3**	**LOI**
Al_2O_3	99.06	<0.01	0.01	0.06	0.01	<0.01	<0.04	0.90
EPK (Kaolin)	35.45	49.44	0.15	0.17	0.11	0.45	0.78	14.21
Whiting ($CaCO_3$)			56.03					43.97

Note: LOI represents "loss on ignition" (i.e. the mass loss upon sintering, assumed to be structural water in the EPK clay and CO_2 in the $CaCO_3$).

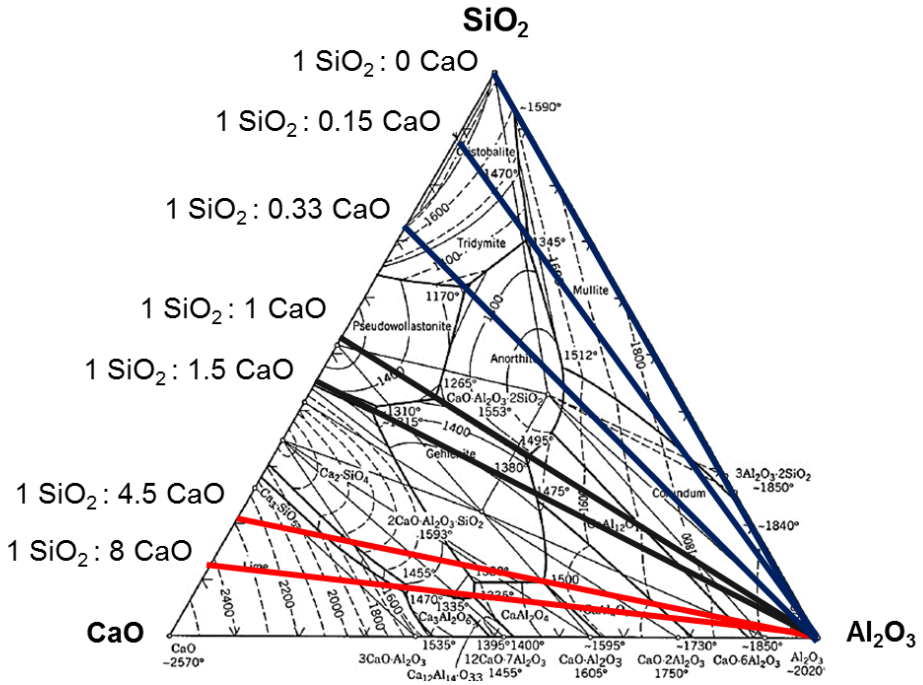

Figure 3.2. CAS ternary diagram (wt%) with target SiO_2:CaO glass phase composition molar ratios.

All suspensions were prepared at 30 vol% solids loading and dispersed using a NH_4-PMAA polyelectrolyte (Darvan C-N, Vanderbilt Minerals, LLC, Norwalk, CT). The suspensions were slightly under-dispersed at 0.3 mg/m^2 to prevent settling of the $CaCO_3$ particles during casting (where as the optimal dispersion level for Al_2O_3 is typically 0.4

mg/m^2).[125-126] Sample suspensions were vibratory milled using Al_2O_3 media for several hours for mixing, then slip cast onto gypsum molds into discs approximately 3.8 cm in diameter. Samples were then dried at 100°C overnight and heat treated in air using a resistance furnace for various times and temperatures based on the experimental design conditions.

3.3.2 Experimental Design

An experimental design software (Design Expert 11, Stat-Ease Inc., Minneapolis, MN) was used to develop both central composite partial factorial and full factorial experimental designs with factors of time (on a log scale), temperature, and Al_2O_3 level. The factors and levels investigated in the experimental design are presented in Table 3.II. The seven target glass phase SiO_2:CaO ratios were analyzed as separate experimental design spaces with identical factors and levels across each composition system.

Table 3.II. Experimental Design Factors and Levels for the Composition Systems Tested

Experiment Factor	**Levels Tested**		
	-1	0	1
Sintering Time (h)	1	3	10
Sintering Temperature (°C)	1450	1500	1550
Alumina Level (wt%)	88	92	96

Table 3.III lists the experimental design treatment conditions for the CCD partial factorial, consisting of twenty randomized runs. The experiment run order was randomized to assess run bias, and five replicate points were measured, indicated by asterisks in Table 3.III. The full factorial models include the same treatment points for the CCD with supplementary points to complete the factorial and the same five replicated points (not included in Table 3.III).

Table 3.III. Experimental Design Conditions for Partial Factorial Central Composite Design

Run	Time (hours)	Temperature (°C)	Alumina Level (wt%)
1	-1	-1	-1
2	-1	-1	0
3	-1	0	-1
4*	-1	0	1
5	-1	1	-1
6	0	-1	-1
7	0	-1	0
8	0	-1	1
9*	0	0	-1
10	0	0	1
11*	0	1	0
12	1	-1	-1
13**	1	0	0
14	1	1	-1
15	1	1	1

*Indicates replicate runs, ** indicates two replicates.

3.3.3 Sample Analysis

Sample bulk densities were measured via immersion, modified for a small sample size (approximately 1-3 g).[127] For skeletal density measurements, sintered samples were ground into powder and measured with a He-pycnometer (AccuPyc II 1340, Micromeritics Instrument Corp., Norcross, GA). Bulk densities were calculated as a percentage of the corresponding skeletal density to determine the reported relative density (%). Relative density values were used to create empirical densification models for each of the compositions studied for the factors of time, temperature, and Al_2O_3 level.

3.3.4 Statistical Analysis

A central composite partial factorial and full factorial ANOVA were completed for each of the seven glass phase compositions analyzed in the experiment to determine significant factors for densification (Design Expert 11, Stat-Ease, Inc., Minneapolis, MN). This analysis was used to generate empirical densification models for each composition

system, with the goal of optimizing the achievable relative densities for each SiO_2:CaO composition and comparing the results of the two experimental design types.

3.4 Results & Discussion

3.4.1 Partial Factorial Statistical Models

Table 3.IV presents an example ANOVA table for the full factorial DOE for samples with glass phase SiO_2:CaO = 1:0 (no added CaO). The ANOVA results were used to select the best-fit models for all experimental designs in this study. P-values < 0.05 (corresponding to a 95% confidence interval) indicate significant factor terms, of which in this case time (on a log scale), temperature, and Al_2O_3 level are significant variables. The statistical software identifies the ideal polynomial order model, and model terms are then reduced to find the optimized "best fit." Model significance is determined using the F-value, which is the ratio of the mean square of the model to the mean square of the residual. Since this value (175.99) is significantly larger than the designated F-statistic for the DOE conditions, the value indicates the model is significant for the data set, and there is no significant lack of fit based on the F-value for the residual error (4.29).[128-131]

Table 3.IV. ANOVA for Linear Model of Density for SiO_2:CaO = 1:0 (No CaO)

Source	Sum of Squares	Degrees of Freedom	Mean Square	F-value	p-value	Significance (p-value <0.05)
Model	2366.86	3	788.95	175.99	< 0.0001	significant
A-Time	609.40	1	609.40	135.94	< 0.0001	significant
B-Temperature	1712.86	1	1712.86	382.08	< 0.0001	significant
C-Alumina Level	65.79	1	65.79	14.68	0.0007	significant
Residual	125.52	28	4.48			
Lack of Fit	119.47	23	5.19	4.29	0.0560	not significant
Pure Error	6.05	5	1.21			
Std. Dev.	2.12		R^2	0.9496		
Mean	82.95		R^2 (Adj.)	0.9442		
C.V. (%)	2.55		R^2 (Pred.)	0.9358		
			Adeq. Precision	44.6601		

Values and significant figures presented as-generated (Design Expert 11, Stat-Ease, Inc., Minneapolis, MN). C.V. represents the coefficient of variation and is defined as the ratio of the standard deviation to the mean.

For each of the seven glass phase compositions, a best-fit model was selected and significant factors for densification were identified, summarized in Table 3.V. Residual error plots, such as Figure 3.3(a), represent the distribution of error between experimentally

measured values and those predicted by the models. Ideally, the plotted residuals should follow a normal distribution about the mean response value (i.e. density) and are used to compare the quality of fit for the model. Although the models were deemed statistically reasonable fits, there was some scatter in the residuals for most of the composition best-fit models, an example of which is presented in Figure 3.3(a) for one composition. External influences such as experimental biases due to run order effects were not observed, as demonstrated by within-range residual distributions versus run order number (Figure 3.3(b)).

There were no immediately discernable trends between the models of varying SiO_2:CaO ratios with the exception that the models appear to move towards higher order polynomials with increasing CaO content in the glass phase. A time dependence on densification was expected; however, it was only determined to be significant in two of the composition systems. This trend seems counter-intuitive, since other liquid-phase sintered ceramic systems are reported to have a time dependence during sintering.[132-133]

Table 3.V. Best Fit Models and Significant Factors for Partial Factorial Designs

SiO_2:CaO Ratio	**Best Fit Model**	**Significant Factors**
1:0 (No CaO)	Linear	**Time** Temperature Al_2O_3 Level
1 : 0.15	Linear	Al_2O_3 Level
1 : 0.33	2-FI	Temperature*
1 : 1.0	2-FI	**Time** Al_2O_3 Level**
1 : 1.5	Quadratic	Al_2O_3 Level*
1 : 4.5	Quadratic	Temperature Al_2O_3 Level**
1 : 8.0	Quadratic	Temperature Al_2O_3 Level**

Note: 2 FI indicates 2-factor interaction model. (*) indicates presence of interaction effect(s), (**) indicates multiple interaction effects.

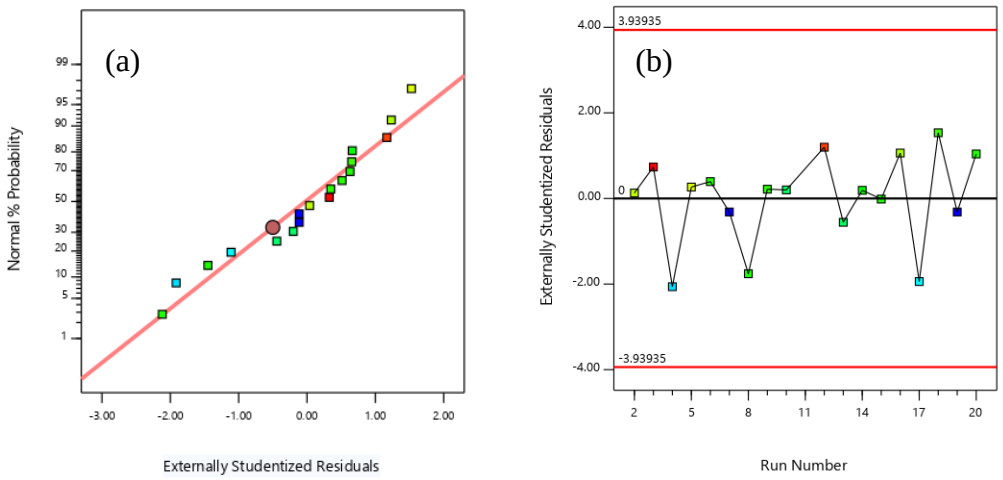

Figure 3.3. (a) Normal probability (%) versus externally studentized residuals and (b) externally studentized residuals versus run order (for 1 SiO_2 : 0.1.5 CaO).[134]

3.4.2 Comparing Full Factorial Models to Partial Factorials

Table 3.VI summarizes the statistical best fit models and significant factors for the seven SiO_2:CaO compositions, analyzed as both partial and full factorial designs. For several of the composition systems, the partial factorial models appear to predict densification behavior reasonably well compared to the full factorial results. In other cases, however, the partial factorial model identifies significant factors different from than the full factorial and, in some cases, even ignores entire factor significances. The composition model containing only SiO_2 did not appear to be significantly changed between the partial and full factorial models, but all of the other models observed did reveal a change in either the best-fit model-types and/or significant factors identified.

Table 3.VI. Best Fit Models and Significant Factors Identified for Partial and Full Factorial Designs

SiO_2:CaO Ratio	Partial Factorial		Full Factorial	
	Best Fit Model	**Significant Factors**	**Best Fit Model**	**Significant Factors**
1:0 (No CaO)	Linear	**Time** Temperature Al_2O_3 Level	Linear	**Time** Temperature Al_2O_3 Level
6.5 : 1	Linear	Al_2O_3 Level	2-FI	Temperature Al_2O_3 Level*
3 : 1	2-FI	Temperature*	2-FI	None**
1 : 1	2-FI	**Time** Al_2O_3 Level**	Linear	Al_2O_3 Level
1 : 1.5	Quadratic	Al_2O_3 Level*	Linear	Al_2O_3 Level
1 : 4.5	Quadratic	Temperature Al_2O_3 Level**	Linear	Temperature Al_2O_3 Level
1 : 8	Quadratic	Temperature Al_2O_3 Level**	Linear	Temperature Al_2O_3 Level

Note: 2 FI indicates 2-factor interaction model. (*) indicates presence of interaction effect, (**) indicates multiple interactions.

In general, it was observed that the full factorial designs resulted in better fit models based on the residual lack of fit, standard deviation and R^2 statistics, and the distribution of residuals. Figure 3.4(a) presents the distribution of residuals for the partial factorial model for samples with SiO_2:CaO = 1:0.15 compared to Figure 3.4(b) the full factorial model. Comparing across all seven compositions, the error in the full factorial models was normally distributed, determined by a better fit to the normal probability trend line than the scatter observed with the partial factorial models, and indicates better model fits. Figures 3.4(c) and (d) present corresponding density response surfaces of temperature versus Al_2O_3 level for the partial and full factorial models, respectively (also for SiO_2:CaO = 1:0.15). The highlighted points in Figures 3.4(c) and (d) at 96 wt% Al_2O_3 and 1550°C demonstrate the discrepancies which can exist between the partial and full factorial models. In this case, the particle factorial predicts the system will achieve <96% theoretical density, when in fact, the full factorial model predicts the system will almost fully densify at these conditions (98-99%). The partial factorial models in these situations may not drastically misrepresent

the data in all cases, but the representation of the data appears to be less complete when compared to the full factorial models.

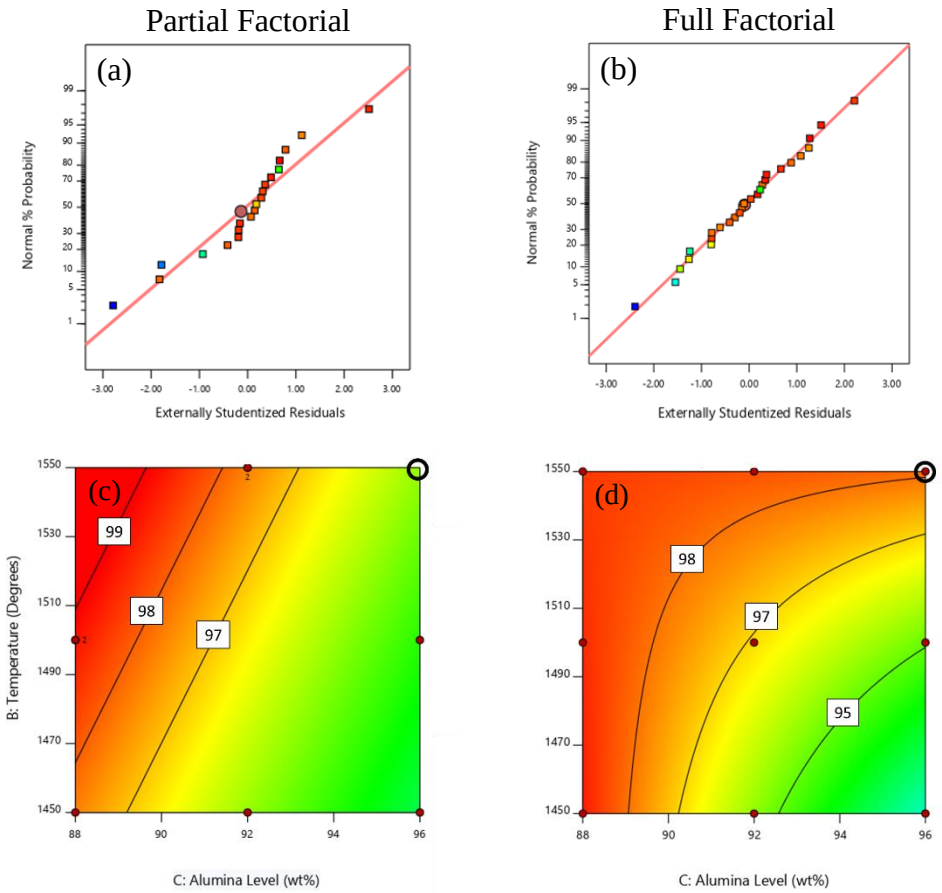

Figure 3.4. Normal probability (%) versus externally studentized residuals for (a) partial factorial and (b) full factorial models, and temperature versus Al_2O_3 level density response surfaces for (c) partial factorial and (d) full factorial models (all sintered for 3 hours with 1 SiO_2 : 0.15 CaO).[134]

Considering full factorial models as the more representative of asymptotic densification behavior, certain trends can be observed in the resulting data in Table 3.VI. Time was not observed to be a significant factor for any of the compositions containing CaO, which contrasts with the clear time dependence observed in the non-CaO system, as well as in the as-received Al_2O_3. The time dependence observed in the system with 1 SiO_2 : 0 CaO indicates this system behaves more like one without significant glass phase (i.e. as-received Al_2O_3). This result is possibly due to a higher glass viscosity from the lack of a modifier (CaO) in the system compared to the other compositions. The majority of the

compositions can be fit to linear models, wherein no significant interactions occur between the three factors. Temperature and Al_2O_3 level appear to be the most significant influences on the majority of the systems, except for SiO_2:CaO = 1 : 0.33, which has no statistically significant first order factors in the design space analyzed but exhibits several interaction effects. Also observable from the full factorial results in Table 3.VI are behaviors allowing grouping of the composition systems into three groups based on the ratio of SiO_2:CaO present: SiO_2:CaO >1, SiO_2:CaO ≈1, and SiO_2:CaO <1. These groupings agree with previously observed behaviors for glasses of similar SiO_2:(R_2O + RO) ratios, where glasses with greater than 50 mole% SiO_2 behave much differently than those with less than 50 mol% SiO_2. These molar ratios of SiO_2:(R_2O + RO) are referred to as invert glasses in the literature.[64]

In order to analyze the generated full factorial models, response surfaces were created to demonstrates the relative influences of the tested factors on densification (time, temperature, Al_2O_3 level). For example, Figure 3.5 presents densification response surfaces for the composition system with 1 SiO_2 : 0.15 CaO. These surfaces should demonstrate the usefulness of RSM for visualizing the effects of multiple factors on a response in the case of densification. With the model for this composition, both sintering temperature and Al_2O_3 level are designated as statistically significant factors, which can be easily observed in the progression of each of these factors at the low, medium, and high levels (Figure 3.5(a) and (c)). Sintering time, however, is not significant, which is apparent in the infinitesimal changes observed in the predicted density with varying sintering times (Figure 3.5(b)). These response surfaces can be used to predict densification behavior for the CAS system, as well as to optimize density conditions for future applications.

Treatment Level	-1 (Low)	0 (Middle)	1 (High)

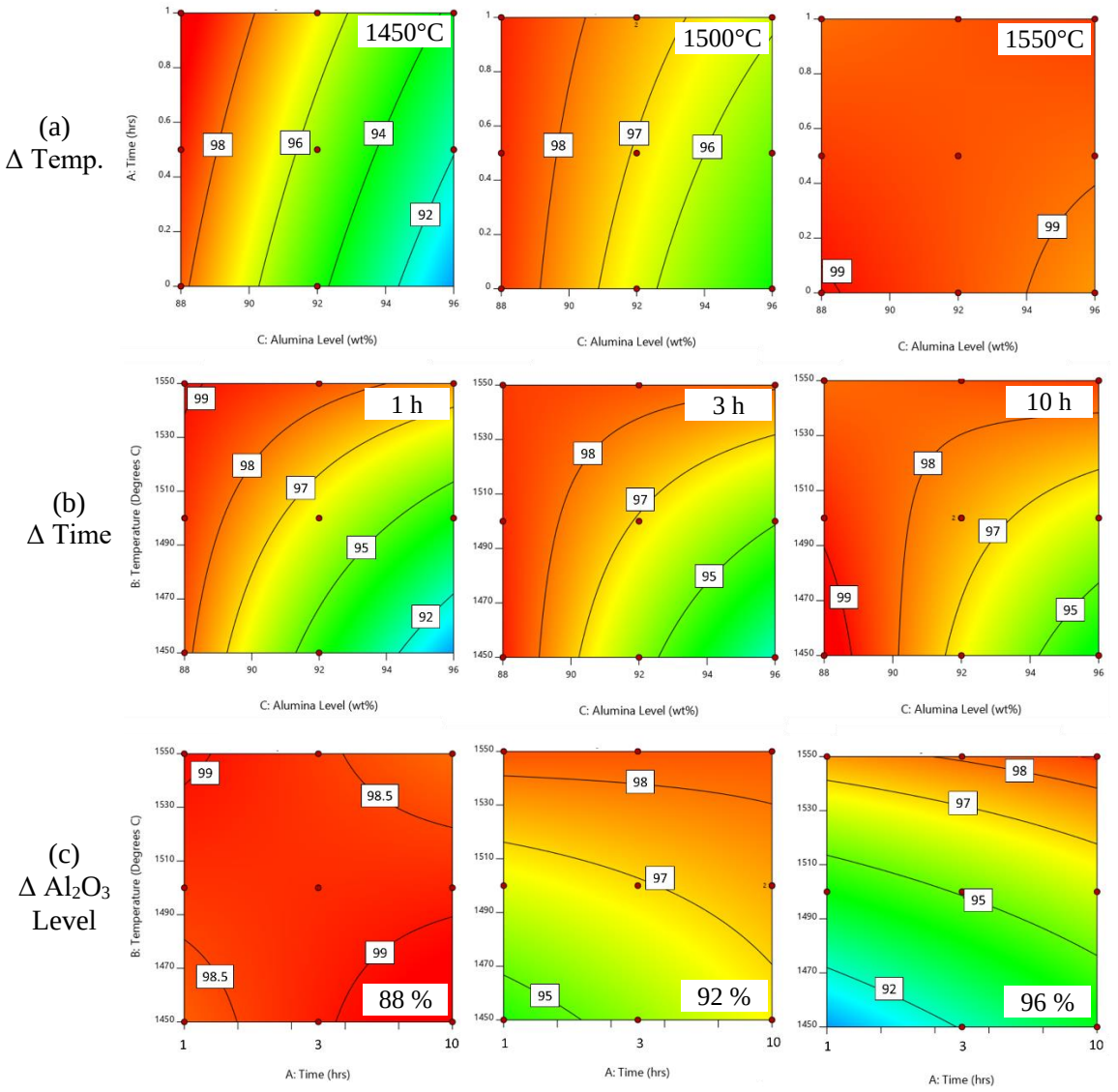

Figure 3.5. Densification response surfaces using various treatment conditions (for SiO_2:CaO = 6.5:1). (a) Time versus Al_2O_3 with varying temperature. (b) Temperature versus Al_2O_3 level with varying time. (c) Temperature versus Time with varying Al_2O_3 level.[134]

3.4.3 Model Validation

In order to compare the validity of each model generated, five confirmation runs were completed for each of the seven compositions. The measured densities were then compared to those predicted by both the partial factorial and full factorial models. Example data from one confirmation test is presented in Table 3.VII (complete data for all five confirmation runs can be found in Appendix 10.2). The differences in percent theoretical

density between both the partial and full factorial designs compared to the measured densities for the same conditions are presented graphically in Figure 3.6. For randomly assigned levels of each of the three factors, both the partial and full factorial models are capable of predicting the resulting density within a few percent. In general, however, the full factorial models predict the density more accurately than the partial factorial models, in some cases by several percent relative density. The confirmation runs reveal greater discrepancies between predicted and measured density values with increasing CaO content (lower SiO_2:CaO ratios) when compared to the high SiO_2 compositions. This trend is proposed to be due to the tendency of high CaO glass compositions to crystallize rather than remain a glass (attributed to the higher fragilities of high CaO glass melts compared to SiO_2 melts), which may complicate the models and explain the higher variability in these compositions.[57, 65-66] These observed differences, in combination with the inability of the partial factorial models to accurately detect all significant factors for densification, suggest full factorial models should be utilized over partial factorials when possible to analyze densification with statistical experimental design.

Table 3.VII**.** Sample Confirmation Run Data Comparing Partial and Full Factorial Model Density Predictions

Factor Conditions				Density Values				
Time (h)	Temp. (°C)	Al_2O_3 Level (wt%)	SiO_2:CaO Ratio	Measured (%)	Partial Fact. Predicted (%)	Difference from Measured (%)	Full Fact. Predicted (%)	Difference from Measured (%)
			1:0	82.85	85.05	2.20	83.78	0.93
			1:0.15	98.99	96.38	2.61	97.33	1.66
			1:0.33	96.61	98.85	2.24	98.38	1.77
1.5	1525	92	1:1.0	98.76	98.62	0.14	97.99	0.77
			1:1.5	96.04	97.71	1.67	97.4	1.36
			1:4.5	93.76	97.13	3.37	92.79	0.97
			1:8.0	90.10	94.85	4.75	90.52	0.42

% Error is noted as the difference between measured and predicted theoretical density.

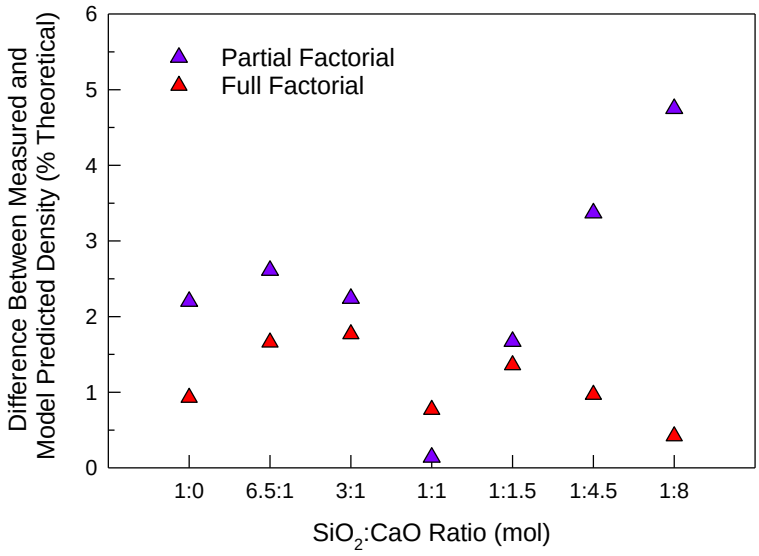

Figure 3.6. Percent difference between measured relative densities and those predicted by both partial and full factorial models for each glass phase composition for confirmation run conditions in Table 3.VII.

3.5 Conclusions

Empirical sintering models were created using both partial and full factorial designs for several glass phase chemistries with varying factors of sintering time, temperature, and Al_2O_3 level. A time dependence for densification was observed in the as-received Al_2O_3 powder (99.8%) and the glass phase system without additional CaO; however, time-independent densification was observed in all glass phase compositions containing CaO for the experimental design conditions investigated. It was also observed that densification behavior is significantly dependent on the glass phase chemistry, and the expected sintering behavior can be grouped by the relative ratios of SiO_2:CaO in the glass phase. Since densification behaves asymptotically with a limited achievable density, it is concluded that typical design of experiments approaches using partial factorials may not be sufficient to describe a liquid-phase sintered ceramic system. Instead, the statistical analyses should be interpreted in the context of the physical system, and a full factorial design over a specific region of interest may result in more accurate predictive sintering models.

4. MICROSTRUCTURE EVOLUTION OF SINTERED Al_2O_3 WITH GLASS CHEMISTRIES IN THE CaO-Al_2O_3-SiO_2 SYSTEM IN THE HIGH SILICA REGION

4.1 Abstract

This study investigates the microstructure evolution of industrial-grade alumina (88-98% Al_2O_3) with glass phase compositions within the CaO-Al_2O_3-SiO_2 system, specifically with SiO_2:CaO ratios > 1. Empirical statistical models were generated to determine the significance of time, temperature, and Al_2O_3 level on densification, and this behavior was compared to the as-received commercial Al_2O_3 (99.8%). Time dependent densification was observed for the as-received Al_2O_3 and samples containing SiO_2 (without CaO), but no time dependence was observed in glass phase systems containing both SiO_2 and CaO. The SiO_2:CaO ratio strongly influenced both densification and average grain size under identical sintering conditions. Grain growth measurements revealed higher average grain sizes in glass phase sintered samples when compared to as-received Al_2O_3; however, the quantity of glass present was not observed to influence grain growth rates.

4.2 Introduction

Alumina (Al_2O_3) is one of the most widely used industrial ceramics, typically sintered in the presence of about 5-14 wt% liquid phase. The chemistry of the liquid phase has previously been demonstrated to have a strong influence on densification and grain growth in high purity Al_2O_3 (>99.9%).[9-20, 26-27] The role of liquid phase properties on microstructure evolution of industrial Al_2O_3 (88-98%), however, has not been thoroughly investigated to date.

During liquid-phase sintering of ceramics, additives and impurities in the system (e.g. SiO_2, CaO, Na_2O, K_2O) melt at lower temperatures than the bulk ceramic and form a liquid, which is typically retained as a glass upon cooling.[2] Even with small impurity levels on the ppm scale, Al_2O_3 will sinter in the presence of a liquid phase, as impurities or additives with low solubility in Al_2O_3 will melt and migrate to the grain boundaries during sintering.[24] These impurities can be a residual product of Al_2O_3 production, as is common in Bayer-process Al_2O_3, or can be added intentionally to enhance densification or other

properties. This liquid phase is argued to allow for densification at lower temperatures and shorter times than would otherwise be possible with high purity systems.

Lam previously described the glass formation boundary approach to predicting sintering behavior of Al_2O_3 with glass phase chemistry in the CaO-Al_2O_3-SiO_2 (CAS) system (Figure 4.1).[41] Using this method, the initial grain boundary chemistry only depends on the impurities present, which melt at lower temperatures than the bulk and form a eutectic liquid into which Al_2O_3 rapidly dissolves.[61] Previous studies have measured this Al_2O_3 dissolution level to be in a constant proportion to the total flux present in the liquid/glass phase (i.e. alkali and alkaline earth oxides): (R_2O+RO): Al_2O_3 = 1:1.19.[61-63]

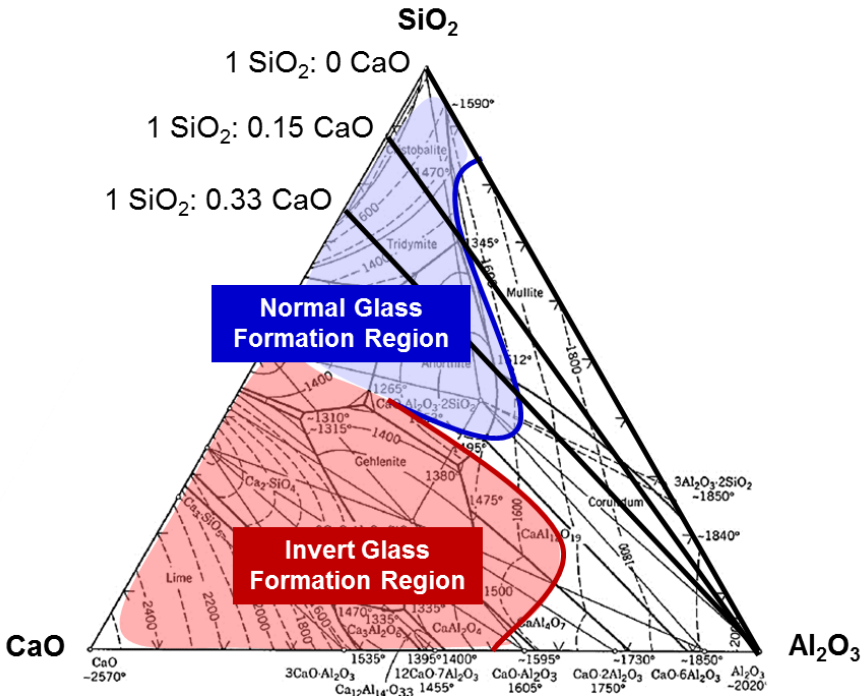

Figure 4.1. CaO-Al_2O_3-SiO_2 phase diagram (in wt%) with normal and invert glass formation regions, as proposed by Lam, and the three target glass phase SiO_2:CaO ratios investigated in this study (solid tie lines).[41]

Glass phase chemistries with SiO_2:CaO >1 are referred to as "normal" glasses. The corresponding glass formation boundary is outlined by the upper curved line in Figure 4.1. Glass phase chemistries with SiO_2:CaO <1 are referred to as "invert" glasses, outlined by the red line in Figure 4.1. This distinction is important, as invert glasses tend to have higher fragilities than normal glasses, and have been demonstrated to have dramatically different

properties, such as lower melting temperature, lower viscosity, greater thermal expansion coefficient, and increased density.[57, 65-66] These glass compositions are correspondingly expected to exhibit differences in densification behavior due to viscosity differences with composition. For example, it has been demonstrated in the CAS system within the normal glass chemistry region where SiO_2 acts as a glass former, that increasing CaO content reduces the viscosity due to increasing glass modifier content.[65-66, 135] Lower viscosities are expected to increase the ease of densification and therefore accelerate the onset of accelerated grain growth during sintering.[136] Only normal glass chemistries are considered throughout this chapter.

The glass formation boundary approach predicts that within the boundary, compositions will intrinsically form a glass when cooled at typical industrial cooling rates (0.12 - 1.7 K/sec). Glass compositions that fall outside this boundary will crystallize mineral phases consistent with the corresponding compositional phase field. This method can be used to predict steady-state, non-equilibrium behavior during liquid-phase sintering of Al_2O_3, which presents the potential for predicting other properties of these materials.

Assuming the previously determined constant dissolution level of Al_2O_3 in the CAS system, where (R_2O+RO): Al_2O_3 = 1:1.19, controlled ratios of SiO_2:CaO can be combined with bulk Al_2O_3 to produce predictable glass chemistries and to correlate these with the microstructure evolution of industrial Al_2O_3. The CAS system was chosen for this study because CaO and SiO_2 are two common impurities in industrial Al_2O_3 systems and significant work has already been performed on these constituents in high purity Al_2O_3 for ready comparison.[9-10, 14-15, 17-18, 25, 31, 33, 43-44] This work seeks to bridge the gap of microstructural evolution of Al_2O_3 between well-described high purity systems (>99.9%) and those commonly used for industrial applications such as high voltage electrical insulators, spark plugs, and refractories (88-98%).

4.3 Experimental Procedure

4.3.1 Sample Preparation

Aqueous Al_2O_3 suspensions (CT 3000 LS SG, Almatis, Inc., Ludwigshafen, Germany) were combined with kaolin clay (EPK, Edgar Minerals, Inc., Hawthorne, FL) and calcium carbonate (Castle Carb 18, Oldcastle Industrial Minerals, Inc., Thomasville,

PA) to generate samples with controlled SiO_2:CaO ratios. The batched molar ratios of SiO_2:CaO, and overall Al_2O_3 levels were calculated based on ICP-ES and loss on ignition (LOI) data for the batched components (Table 4.I). The three target glass phase compositions are represented by the tie lines of constant SiO_2:CaO molar ratios in Figure 4.1, including two aligned with eutectic points at 1512°C and 1345°C, and one composition with only SiO_2 added.

The measured physical and chemical characteristics of the components used in this study are presented in Table 4.I. The Al_2O_3 powder was characterized via BET specific surface area (TriStar II, Micromeritics Instrument Co., Norcross, GA), He-pycnometry (AccuPyc II, Micromeritics Instrument, Co., Norcross, GA), and particle size distribution (SediGraph III PLUS, Micromeritics Instrument, Co., Norcross, GA). Chemical compositions were measured using inductively coupled plasma spectroscopy (ICP-ES) (Mineral Laboratories Canada, Bureau Veritas Commodities Canada, Ltd., Vancouver, BC, CA).

Table 4.I. Powder Characterization of As-received Al_2O_3 and Batched Components

Al_2O_3 Powder Properties								
BET Specific Surface Area:	5.76 m^2/g			D_{50} Particle Size:	0.45 μm			
Density:	3.92 g/cm^3			D_{90} Particle Size:	1.89 μm			
Composition of Batch Components (wt%)	**Al_2O_3**	**SiO_2**	**CaO**	**MgO**	**Na_2O**	**K_2O**	**Fe_2O_3**	**LOI**
Al_2O_3	99.06	<0.01	0.01	0.06	0.01	<0.01	<0.04	0.90
EPK (Kaolin)	35.45	49.44	0.15	0.17	0.11	0.45	0.78	14.21
Whiting ($CaCO_3$)			56.03					43.97

All suspensions were prepared at 30 vol% solids loading and dispersed using a NH_4-PMAA polyelectrolyte (Darvan C-N, Vanderbilt Minerals, LLC, Norwalk, CT). The suspensions were slightly under-dispersed at 0.3 mg/m^2 to prevent settling of the $CaCO_3$ during casting (where the optimal dispersion level for Al_2O_3 is assumed to be 0.4 mg/m^2).[125-126] Sample suspensions were vibratory milled using Al_2O_3 media for several hours for mixing, then slip cast on gypsum molds into discs approximately 2.5 cm in diameter. Samples were then dried at 100°C overnight and sintered using an electric furnace in air at various times and temperatures (DT-29-FL-12-E3504, Deltech, Inc., Denver, CO).

4.3.2 Experimental Design Setup & Statistical Analysis

Statistical experimental design software was used to develop full factorial ANOVAs (analysis of variance) with factors of time, temperature, and Al_2O_3 level for each individual composition system.[134] The factors and levels investigated are presented in Table 4.II, which include twenty-seven randomized runs with five additional replicated points. This analysis was used to generate empirical densification models and determine significant factors for densification of each SiO_2:CaO ratio system. An analysis of the accuracy of using statistical models to represent densification of ceramics and justification of the selected factorial model for this experiment has been addressed in Chapter 3.

Table 4.II. Experimental Design Factors and Levels for the Composition Systems Tested

Experiment Factor	**Levels Tested**		
	-1	0	1
Sintering Time (h)	1	3	10
Sintering Temperature (°C)	1450	1500	1550
Alumina Level (wt%)	88	92	96

4.3.3 Sample Analysis

Bulk densities of post sintered samples were measured via immersion using modifications for small sample sizes of approximately 1-3 g.[127] Samples were then ground into powder and skeletal densities were measured using He-pycnometry (AccuPyc II 1340, Micromeritics Instrument Corp., Norcross, GA). Relative densities were then calculated as a percentage of bulk density to corresponding skeletal density and used to create empirical densification models with factors of time, temperature, and Al_2O_3 level. Ground samples were also analyzed using x-ray diffraction (XRD) (D2 PHASER, Bruker Corporation, Billerica, MA), and phase ID was conducted using Diffrac.EVA software (Bruker Corporation, Billerica, MA) and the PDF 4+ 2019 database (ICDD, Newton Square, PA). Chemical analysis was completed via ICP-ES (Mineral Laboratories Canada, Bureau Veritas Commodities Canada, Ltd., Vancouver, BC, CA).

Samples were prepared for microstructure analysis by grinding and subsequently polishing to a 1 µm finish (MetLab Corp., Niagara Falls, NY). As-received samples (99.8%

Al_2O_3) were thermally etched 50°C below the corresponding sintering temperature for 30 minutes. Samples with additional glass phase were first chemically etched in 10% HF for 10 seconds to remove the glass phase, then thermally etched to reveal grain boundaries 50°C below the initial sintering temperature, as described in Chapter 2. After etching, sample microstructures were analyzed via SEM (ESEM, Quanta 200, FEI Company, Hillsboro, OR) and average grain sizes were measured via the Abrams Three-Circle Procedure according to ASTM Standard E112, with a 95% relative confidence interval.[75]

4.4 Results & Discussion

4.4.1 Microstructure Evolution of As-received Al_2O_3

Presented in Figure 4.2(a) are densification curves for the as-received Al_2O_3 sintered for times between 0.1-30 hours at 1500 and 1550°C. Densification scales linearly with temperature and with the log of time; both variables were determined to be statistically significant for densification. This relationship is represented by the densification contour model in Figure 4.2(b), where the shaded areas are interpreted to predict full densification at 100% relative density, since greater than 100% densification is not physically possible.

Microstructures of the as-received powder sintered for various times (Figure 4.3) exhibit typically equiaxed grains with increasing grain size with longer sintering time. It should be noted that the bulk samples did not reach 100% relative density even after extended sintering times (>10 hours). This phenomenon is often observed in Bayer-process industrial Al_2O_3, but is frequently unaddressed in the literature. Previous work has proposed the limitations of full densification to be caused by agglomerates inherently produced from the Bayer powder synthesis, which are proposed to pin pores and prevent absolute densification. This topic will be addressed in more detail in Chapter 6.

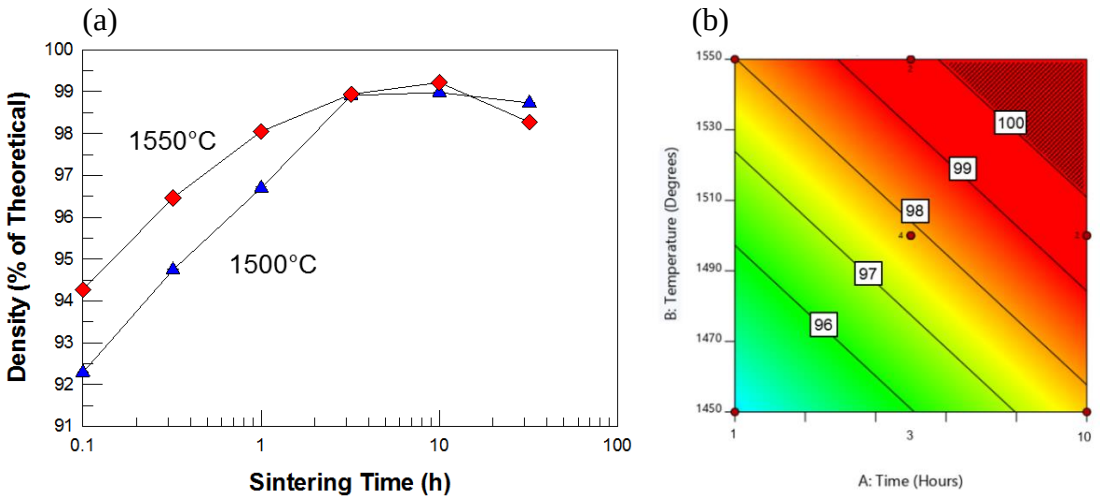

Figure 4.2. (a) Densification of as-received Al_2O_3 at various time/temperature conditions (standard deviations between 0.01-0.02 relative density for all points included but not visible); (b) Densification contour of as-received Al_2O_3. The red shaded region indicates highest achievable density (100%).

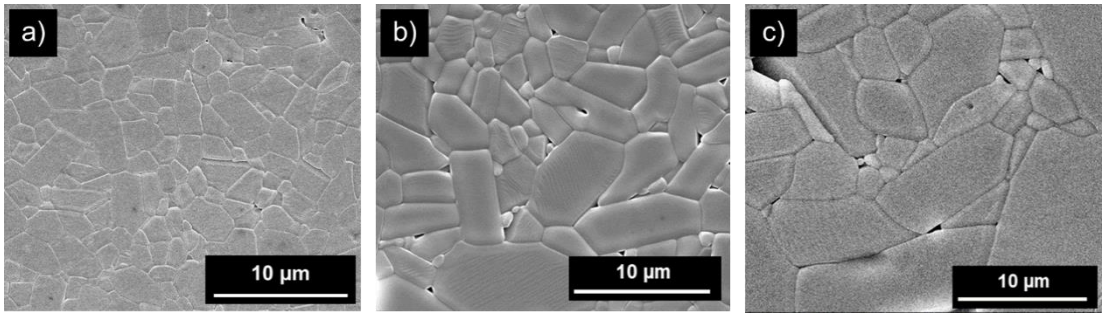

Figure 4.3. Microstructures of as-received Al_2O_3 (99.8 wt%) sintered at 1550°C for (a) 3 hours, (b) 10 hours, and (c) 30 hours. Samples were thermally etched at 1500°C for 30 minutes.

Figure 4.4 presents average grain size data for the as-received Al_2O_3 sintered at 1500 and 1550°C. Expected behavior of increasing grain size with increasing time and temperature is observed at both temperatures. A small change in the grain growth rates at 1500°C and 1550°C 1 hour, where an increased growth rate initiates. Correlating this change to the densification of the systems, the shift occurs at ≥98% theoretical density in both instances, where the systems essentially reach their maximum achievable relative densities. The grain growth rates (i.e. slopes) of the four line segments, two temperature segments both before and after the rate change, were calculated using linear regression. The growth rates before the shift for 1500°C and 1550°C were 0.14 and 0.16 µm/hour, and after the shift were 0.32 and 0.30 µm/hour, respectively. The similarities in slopes for

differing temperature in each region indicates the grain growth rate is independent of temperature, but is instead dependent on the elimination of porosity and grain pinning pores.

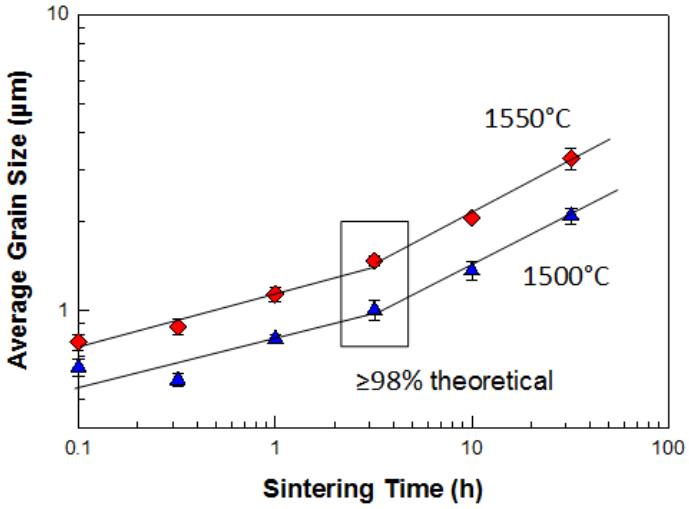

Figure 4.4. As-received Al_2O_3 (99.8%) sintered at 1500°C and 1550°C, thermally etched 50°C below the respective sintering temperature for 30 minutes.

4.4.2 Densification of Al_2O_3 with Varying Glass Phase Chemistries

Table 4.III summarizes the results of the ANOVA for the three SiO_2:CaO compositions tested. The composition without additional CaO follows a linear model, with statistically significant factors of temperature, time, and Al_2O_3 level on densification. Time was not a significant factor for the two compositions containing CaO, which contrasts with the time dependence observed in the as-received Al_2O_3. These two models also reveal more complicated interaction effects between factors compared to that of the all SiO_2 system, and the composition with 1 SiO_2 : 0.33 CaO displaying no direct significance on densification using any of the three factors tested. The empirical models can be used to predict and optimize densification behavior across these systems, as well as observe factor dependencies. Figure 4.5 displays densification contour maps from the generated models for three sintering temperatures, demonstrating the effects of time versus Al_2O_3 level on relative density (reported as a percentage of theoretical density of Al_2O_3). These models were generated from the experimental design and can be used to predict and optimize densification behavior across these systems, as well as observe dependencies of

densification on varying conditions, such as the significant dependence on temperature (Figure 4.5). Further details regarding the applicability of statistical experimental design to represent densification in the CAS system is discussed in Chapter 3.

Table 4.III. Best Fit Models and Significant Factors Identified for Full Factorial Designs

SiO_2:CaO Ratio	Best Fit Model	Significant Factors
1 : 0	Linear	Temperature Time Al_2O_3 Level
1 : 0.15	2 Factor Interaction	Al_2O_3 Level Temperature*
1 : 0.33	2 Factor Interaction	None*
Equation for Percent Relative Density (input in experimental units)		
1 : 0	= 249.76 + 10.79(Time) + 0.19(Temp.) + 0.45(Al_2O_3 Level)	
1 : 0.15	= 1104.99 + 0.98(Time) - 0.65(Temp) - 11.40(Al_2O_3 Level) + 0.01(Temp.*Al_2O_3 Level)	
1 : 0.33	= 449.96 + 41.04(Time) - 0.24(Temp.) - 4.13(Al_2O_3 Level) - 0.03(Time*Temp.) + 0.003(Temp.*Al_2O_3 Level)	

Note: (*) indicates the presence of interaction effects.

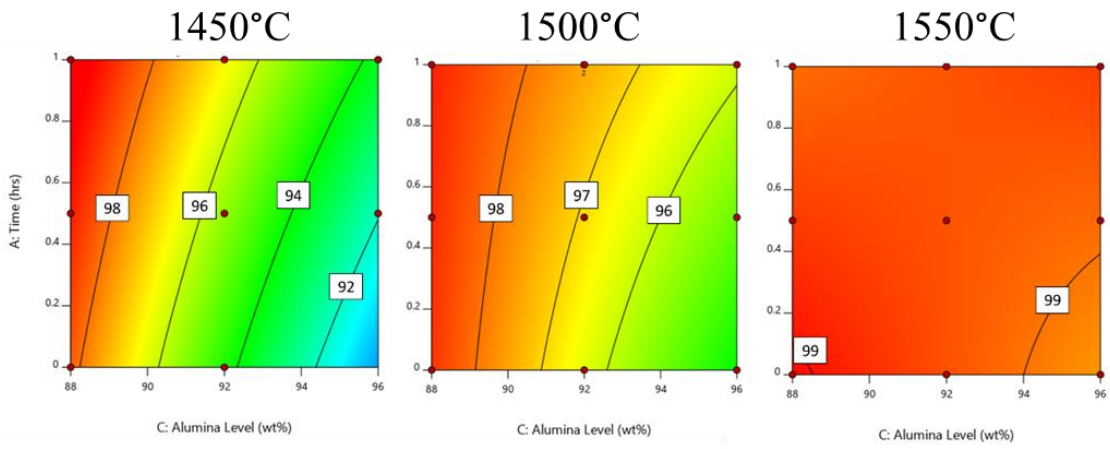

Figure 4.5. Time versus Al_2O_3 level densification contours with glass phase composition 1 SiO_2 : 0.15 CaO at varying sintering temperatures.

4.4.3 Chemical and Phase Analysis of Varying Glass Phase Compositions

Table 4.IV lists measured versus target Al_2O_3 levels for each of the three glass phase chemistries, measured via ICP-ES for samples sintered at 1500°C for one hour. Based on this data, the Al_2O_3 levels achieved during sintering were less than 2% error of the target values with the average error being ~1%. Also included in Table 4.IV are the target and measured SiO_2:CaO ratios for the sample compositions. Small deviations in the SiO_2 or CaO levels drastically change the resulting component ratio; however, those achieved are reasonably within range of the target values and follow the desired trends. Figure 4.6 presents the CAS diagram with the difference in target SiO_2:CaO ratios (solid lines) compared to those measured (dashed lines).

Table 4.IV. ICP-ES Chemistries of Selected Glass Phase Compositions with Measured-Target Al_2O_3 Levels and SiO_2:CaO Ratios (all samples fired at 1500°C for one hour)

Target Al_2O_3 Level (wt%)	**Measured Al_2O_3 Level (wt%)**		
	1 SiO_2 : 0 CaO	**1 SiO_2 : 0.15 CaO**	**1 SiO_2 : 0.33 CaO**
88	89.5	89.8	89.1
92	92.9	92.8	92.7
96	95.9	95.6	94.7
Target SiO_2:CaO Ratio (mol)	**Measured SiO_2:CaO Ratio (mol)**		
	88 wt% Al_2O_3	**92 wt% Al_2O_3**	**96 wt% Al_2O_3**
1 : 0	76.5	70.2	41.8
1 : 0.15	6.8	7.1	7.6
1 : 0.33	3.5	3.6	4.6

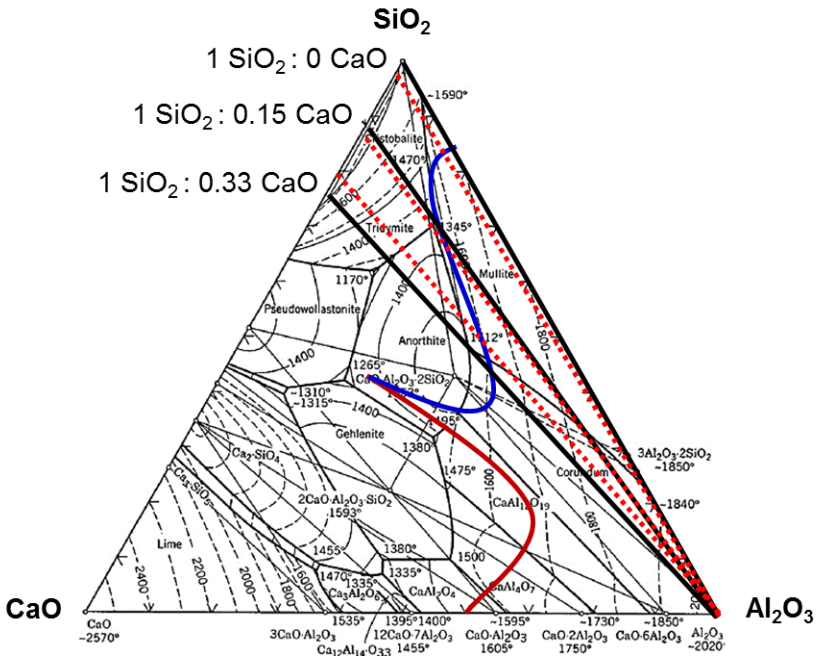

Figure 4.6. Target (solid line) versus achieved (dotted line) SiO_2:CaO ratios for the three target glass phase chemistries.

X-ray diffraction was used to confirm the presence of secondary phases from a selection of experimental sintering conditions from this study. Figure 4.7 displays a sampling of XRD patterns for the analyzed samples, including the as-received Al_2O_3, where only corundum (Al_2O_3) is present. The composition without additional CaO revealed the presence of mullite ($3Al_2O_3 \cdot 2SiO_2$), and a sample with 1 SiO_2 : 0.33 CaO revealed very small quantities of anorthite ($CaO \cdot Al_2O_3 \cdot 2SiO_2$). The secondary phases detected for various sintering conditions are summarized in Table 4.V. Alpha Al_2O_3 (corundum) and an amorphous hump indicating a glass phase are present in all samples but are omitted from the table.

For the glass phase composition with no additional CaO, mullite was present in all cases. This behavior is consistent with the CAS ternary diagram and the glass formation boundary for this composition (Figure 4.1), where mullite is predicted to form upon sintering. Samples with 1 SiO_2 : 0.15 CaO also reveal the presence of mullite, as the tie line for this composition in Figure 4.1 crosses through the invariant point (eutectic) of the tridymite, anorthite and mullite phase fields, then passes through the glass formation region into the mullite region. Samples with 1 SiO_2 : 0.33 CaO did not exhibit mullite, which was

expected since this SiO_2:CaO ratio resides outside the mullite phase region. Based on the GFB for 1 SiO_2 : 0.33 CaO, the only secondary phase expected to form is corundum (Al_2O_3); however, an additional anorthite phase was observed in every sample analyzed with this composition. Since the glass formation region for this composition lies to the right of the anorthite phase field, it is not believed that the anorthite formed from the glass during cooling, but instead formed through a solid state reaction at a lower temperature than the liquidus temperature where liquid/glass formation occurred. Previous work has demonstrated anorthite may form within the CAS system at temperatures as low as 954°C and has also been reported in studies of under-fired glazes, which have all been attributed to solid state reactions.[41, 60, 137-138] An observed case of anorthite formation for the composition with 1 SiO_2 : 0.15 CaO is unexpected, suggesting non-uniform component distribution within the sample.

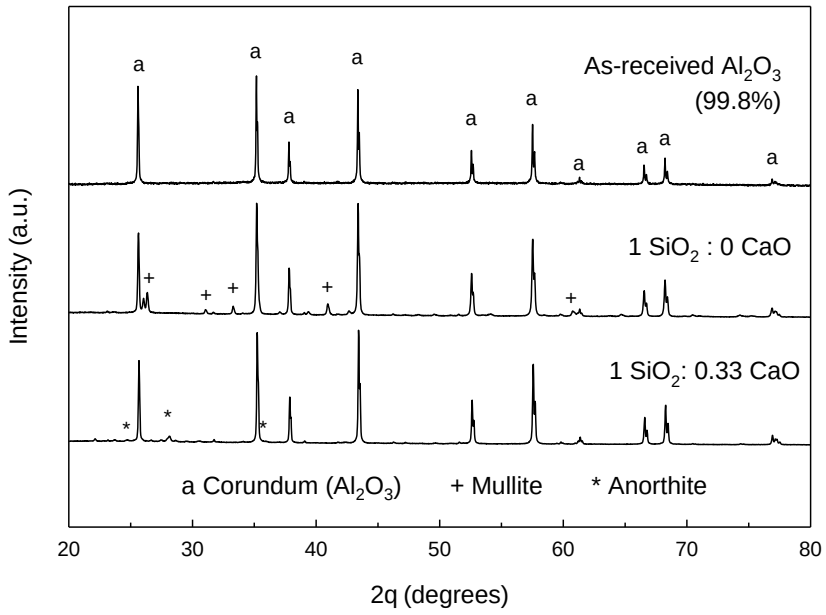

Figure 4.7. XRD patterns for samples sintered at 1450°C for 3 hours: (top) as-received Al_2O_3 (99.8%), (middle) 92 wt% Al_2O_3 with 1 SiO_2 : 0 CaO, and (bottom) 92 wt% Al_2O_3 with 1 SiO_2 : 0.33 CaO.

Table 4.V. Crystalline Phases Identified via XRD for Varying Sintering Conditions and Glass Phase Chemistries Investigated

SiO_2:CaO Ratio	Time (h)	Temp. (°C)	Al_2O_3 Level (wt %)	Mullite ($3Al_2O_3 \cdot 2SiO_2$)	Anorthite ($CaO \cdot Al_2O_3 \cdot 2SiO_2$)
1:0 (No CaO)	1	1550	88	X	
	3	1450	88	X	
	3	1450	92	X	
	3	1500	88	X	
	3	1500	96	X	
	10	1550	88	X	
1:0.15	1	1550	88	X	
	3	1450	88	X	
	3	1450	92	X	
	3	1500	88	X	X
	3	1500	96	X	
	10	1550	88	X	
1:0.33	1	1550	88		X
	3	1450	88		X
	3	1450	92		X
	3	1500	88		X
	3	1500	96		X
	10	1550	88		X

α-Al_2O_3 (corundum) and an amorphous hump indicating glass phase were present in all samples but are omitted in table.

4.4.4 Grain Size Analysis of Varying Glass Phase Compositions

Figure 4.8 presents microstructures for glass phase samples with the three SiO_2:CaO ratios investigated at 1450, 1500, and 1550°C (all samples at 92 wt% Al_2O_3). The average grain size values presented in the figure represent an equivalent spherical diameter. It should be noted that the combined chemical-thermal etch process results in no visibility of the glass phase in any of the following images, as discussed in Chapter 2.

In Figure 4.8, grain size is observed to increase with increasing sintering temperature, which is expected due to an increased driving force for grain growth at elevated temperatures. The Al_2O_3 grains are relatively equiaxed and appear to possess a normal size distribution, indicative of normal grain growth. The grain size data is represented graphically in Figure 4.9(a). The average grain sizes increase with increasing CaO content, and the composition without additional CaO displays the smallest grain size. The same trend of increasing grain size with increasing CaO content is also observed with varying Al_2O_3 levels (Figure 4.9(b)), and visually in the micrographs in Figure 4.10.

Varying Al_2O_3 level, however, was not observed to have a significant effect on grain size for the compositions investigated (Figure 4.9(b)).

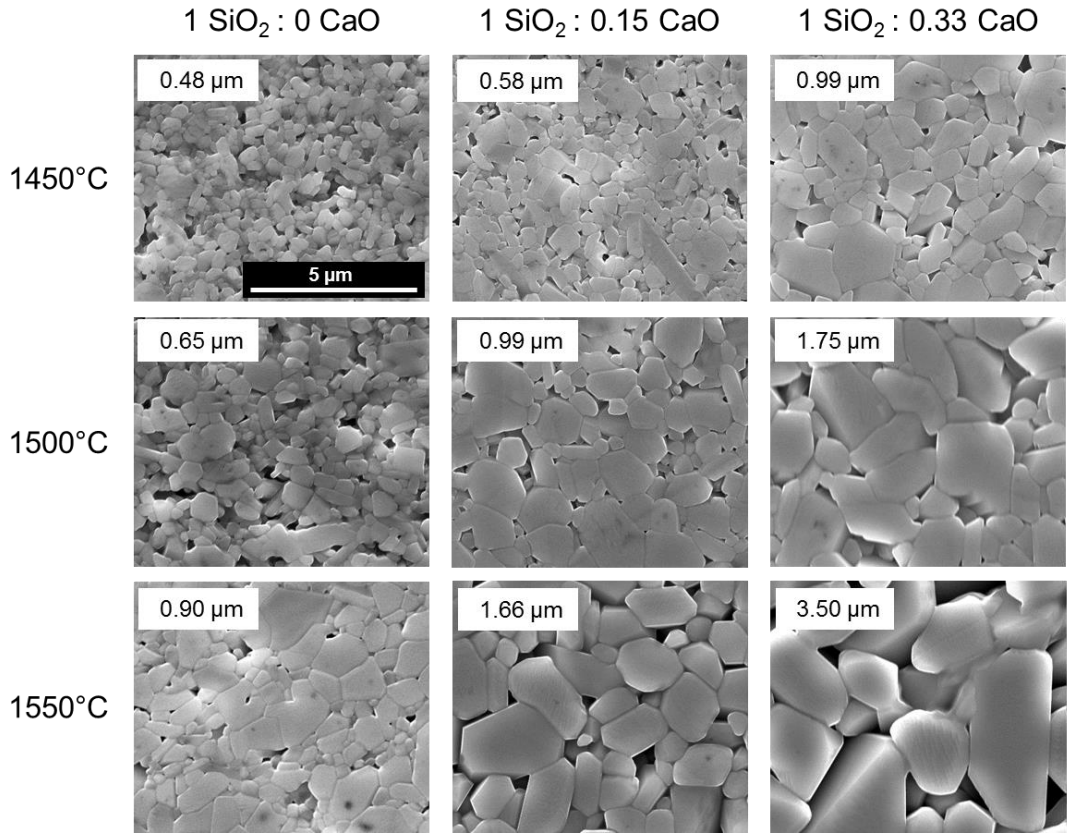

Figure 4.8. Microstructures for 92 wt% Al_2O_3 samples sintered for 3 hours at varying temperatures and SiO_2:CaO ratios (average grain sizes in upper left box). All images presented at the same magnification.

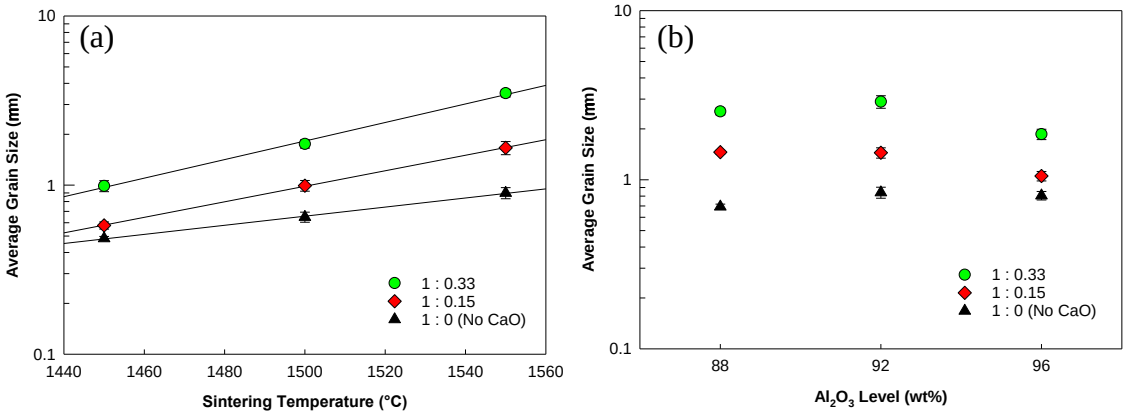

Figure 4.9. (a) Average grain size versus sintering temperature for 92 wt% Al_2O_3 samples sintered for 3 hours and (b) Average grain size versus Al_2O_3 level for samples sintered at 1500°C for 3 hours. The ratios listed are SiO_2:CaO composition ratios.

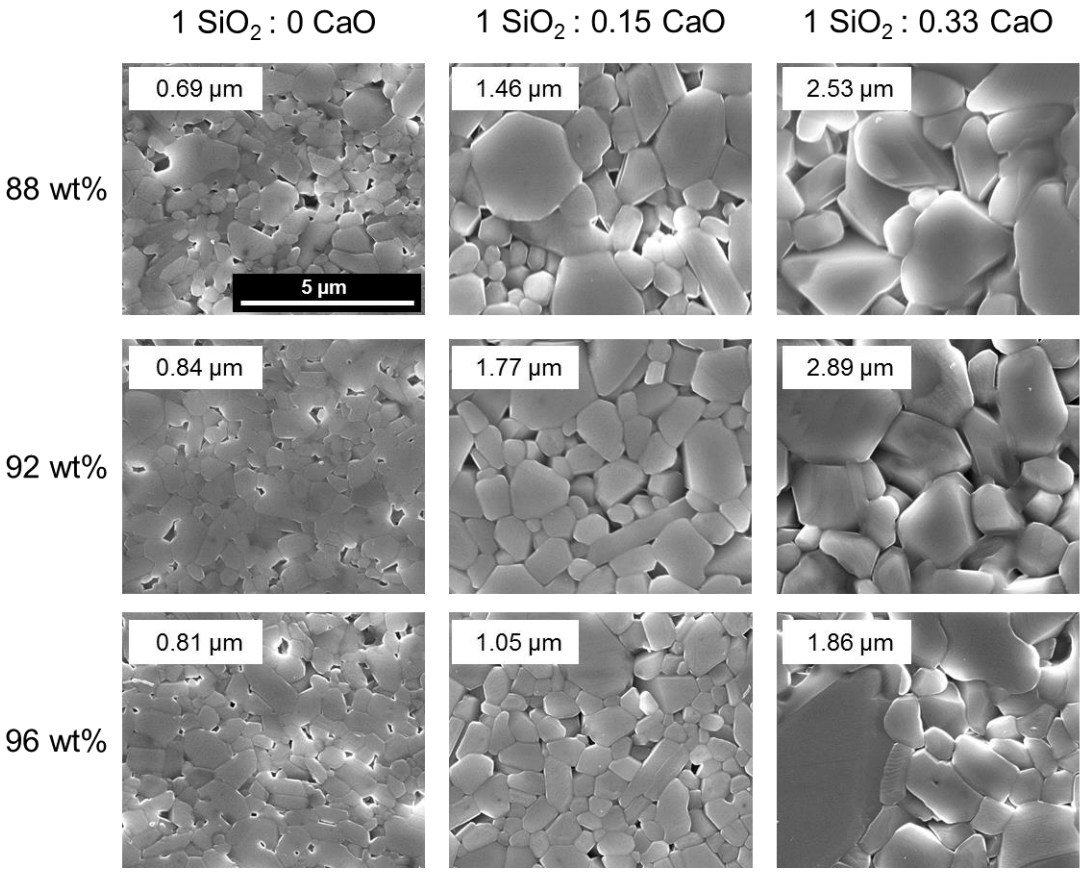

Figure 4.10. Microstructures and average grain sizes for samples sintered for 10 hours at 1500°C with varying wt% Al_2O_3 and SiO_2:CaO ratios. All images presented at the same magnification.

Microstructures for the three glass phase compositions sintered for various times are presented in Figure 4.11. Similar to Fig. 4.8, average grain size increases with increasing CaO content and sintering time (Figure 4.12). Evaluated grain growth rates obtained from using regression analysis are presented in Table 4.VI. The composition with no additional CaO had the slowest growth rate, which is proposed to be caused by poor densification. Traditional sintering theory predicts significant grain growth starts during the final stage of sintering, approximately 85-90% relative density; however, this shift in growth rate in the as-received Al_2O_3 was observed to occur at ≥98%.[136] The composition without additional CaO is expected to have a higher viscosity due to the lack of glass modifier compared to the compositions containing CaO, thus slowing down densification, diffusion, and reducing significant grain growth.

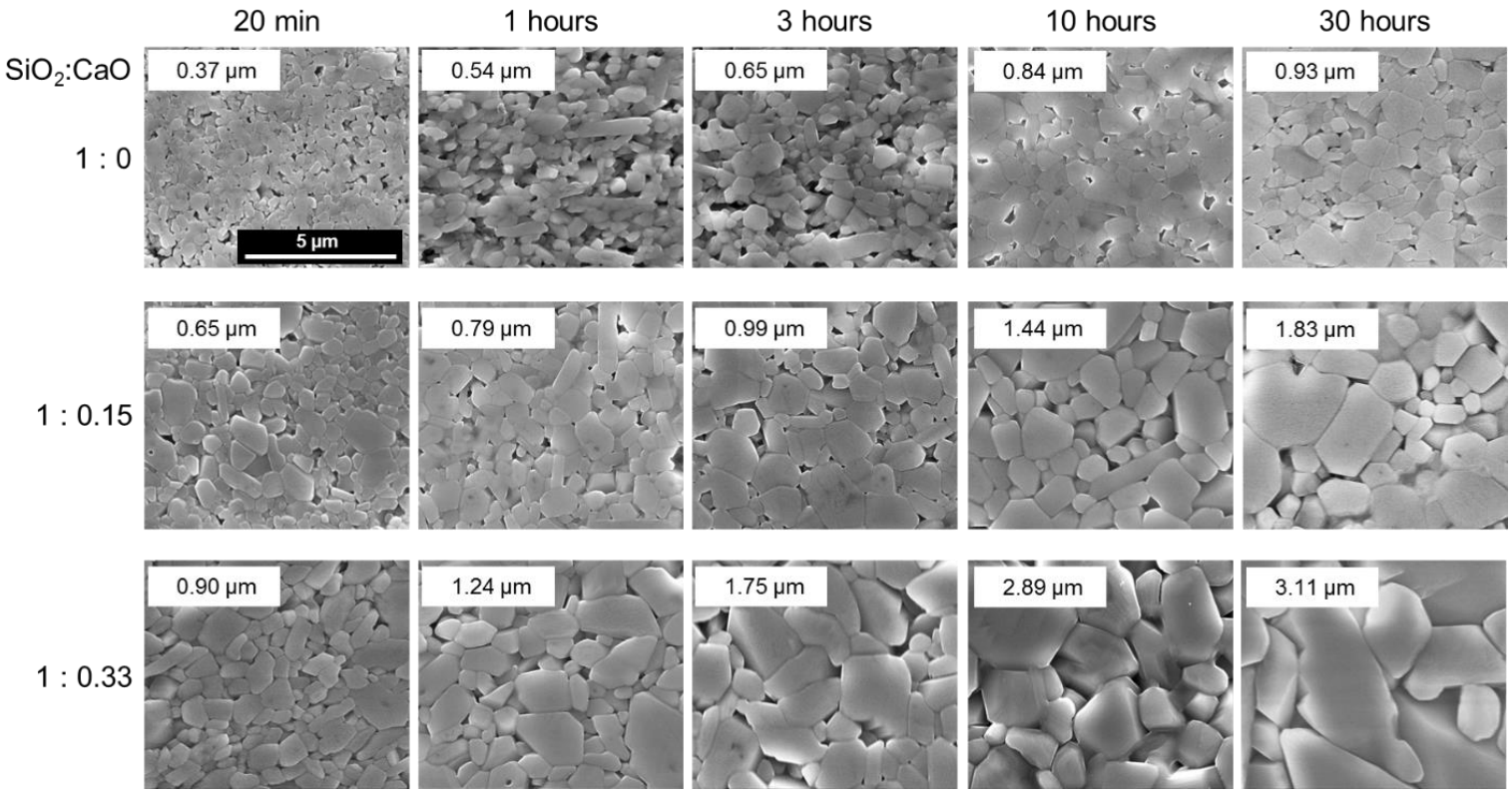

Figure 4.11. Microstructures for 92 wt% Al_2O_3 samples sintered at 1500°C at various time and SiO_2: CaO ratios (average grain sizes in upper left box). All images presented at the same magnification.

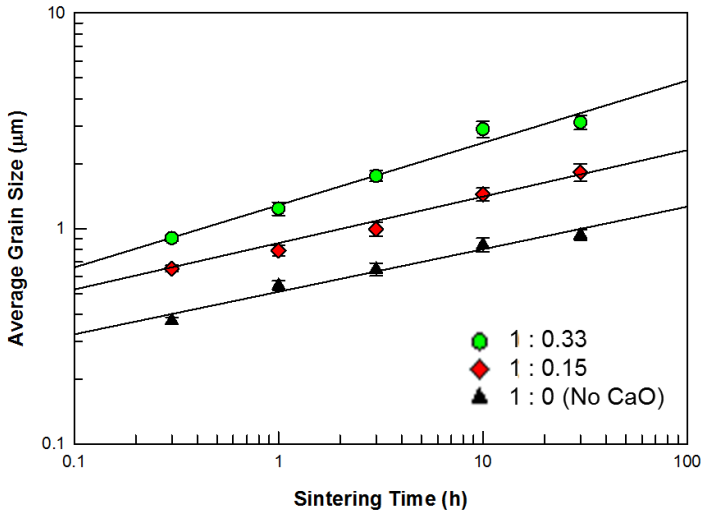

Figure 4.12. Average grain size versus sintering time for 92 wt% Al_2O_3 with varying SiO_2: CaO ratios, all sintered at 1500°C.

Table 4.VI. Measured Grain Growth Rates for Samples in Figure 4.12

SiO_2:CaO Ratio	**Grain Growth Rate (µm/h)**
1:0.33	0.289
1:0.15	0.231
1:0	0.197

The grain growth rates in Table 4.VI for the two compositions with CaO (0.289 and 0.231 µm/hour) are similar to the growth rate observed in the as-received Al_2O_3 after the point of 98% relative density was achieved (0.32 µm/hour), so it is predicted that these two compositions are close to or have surpassed this point of densification. Using the statistical densification models generated in Section 4.2, these relative densities can in fact be predicted for times between 1 and 10 hours (Figure 4.13). The glass phase composition without additional CaO is not fully densified, with only 87.9% relative density achieved even after 10 hours. Lower densification is attributed to the lack of glass modifiers present (i.e. CaO), which results in a higher viscosity and correspondingly lower densification rate. Since this system has not reached the point of densification where accelerated grain growth occurs, argued to be ≥98%, the remaining pores pin grains, so an accelerated grain growth rate is not observed. The composition with 1 SiO_2 :

0.33 CaO has already reached 98%, so an accelerated grain growth rate, and larger average grain size, as expected in this case, is observed.

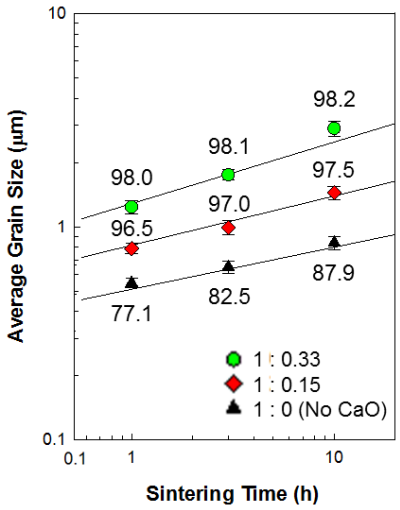

Figure 4.13. Predicted density values (% theoretical density) for 92 wt% Al_2O_3 samples sintered at 1500°C.

4.5 Conclusions

This study investigated the densification and grain growth behavior of industrial grade Al_2O_3 sintered in the presence of a glass phase in the CaO-Al_2O_3-SiO_2 system. A clear time and temperature dependence was observed for densification of the as-received powder (99.8 wt%), but a discontinuity emerged with the addition of significant glass phase, where time-independent densification occurred. A strong effect of glass phase chemistry on both densification behavior and grain growth was observed for varying SiO_2:CaO ratios. As-received Al_2O_3 was observed to have a variable grain growth rate, where the rate change occurred near the highest density achieved (≥98% theoretical); however, this rate change was not observed for the grain growth of samples containing significant glass phase for the sintering times investigated. On average, it was observed that average grain size increased with increasing CaO content, and the system with no additional CaO (all SiO_2) exhibited smaller grain sizes than the as-received Al_2O_3. The increased grain size with CaO content is attributed to a faster densification rate in the presence of these glass phases, where the onset of accelerated grain growth occurs earlier during sintering, resulting in larger grain sizes.

5. MICROSTRUCTURE EVOLUTION OF SINTERED Al_2O_3 WITH GLASS CHEMISTRIES IN THE CaO-Al_2O_3-SiO_2 SYSTEM IN THE HIGH CALCIUM REGION

5.1 Abstract

This study investigates the microstructure evolution of industrial Al_2O_3 (99.8%) sintered with glass phase chemistries in the CaO-Al_2O_3-SiO_2 system, specifically with SiO_2:CaO ratios ≤ 1 (high CaO content). Both Al_2O_3 level and sintering temperature were determined to be statistically significant for densification; however, time was not significant within the range tested (1-10 hours). The SiO_2:CaO ratio strongly influenced both densification and grain size under identical sintering conditions, and behaviors could be grouped by the relative ratios of SiO_2:CaO≈1 and SiO_2:CaO <1, recognized as the "invert" glass region. Secondary phases were observed to form during sintering, most frequently hibonite ($CaO·6Al_2O_3$), which was predicted based on the presented Glass Formation Boundary theory. Other crystalline phases observed are proposed to form through a solid state reaction at lower temperatures. Al_2O_3 grains exhibited normal grain growth, but significant secondary crystallization with increasing CaO content limited the growth of Al_2O_3 grains. Combined with data presented in previous work, the average grain size of Al_2O_3 grains increased with increasing CaO content until the SiO_2:CaO ratio fell below 1:1.5, where excessive secondary phase formation occurred.

5.2 Introduction

Alumina (Al_2O_3) is one of the most widely used industrial ceramics, and it is typically sintered with approximately 5-14 wt% liquid forming additives. The liquid phase chemistry has been revealed to have a strong influence on microstructure evolution in high purity Al_2O_3 (>99.9%)[9-20, 26-27]; however, the role of the liquid phase chemistry on densification and grain growth of industrial-grade Al_2O_3 (88-98%) has been minimally studied.

During liquid-phase sintering of ceramics, additives and impurities in the system such as SiO_2, CaO, Na_2O, and K_2O form eutectic melts with SiO_2 at lower temperatures than the bulk ceramic and form a liquid, which is typically retained upon cooling.[2] Even with impurity levels on the ppm scale, Al_2O_3 will sinter in the presence of a liquid phase,

as these constituents have low solubility in Al_2O_3 and therefore melt and migrate to grain boundaries.[24] These impurities can be residual from the production of Al_2O_3, as is common in Bayer-process Al_2O_3, or can be added intentionally to enhance densification or other properties. The presence of a liquid phase is argued to allow for densification at lower temperatures and with shorter sintering times than is possible with a higher purity powder.

Work by Lam previously described the glass formation boundary (GFB) approach to predict the sintering behavior of Al_2O_3 with glass phase chemistries in the CaO-Al_2O_3-SiO_2 (CAS) system (Figure 5.1).[41] According to the GFB theory, the initial grain boundary chemistry only depends on the impurities present, which form a eutectic liquid during sintering into which Al_2O_3 rapidly dissolves.[61] Previous studies have demonstrated the Al_2O_3 dissolution is in constant proportion to the total flux present in the liquid/glass phase (i.e. alkali and alkaline earth oxides), obeying the ratio of (R_2O+RO): Al_2O_3 = 1:1.19.[61-63] The GFB predicts that to the left of the boundary, compositions will intrinsically form a glass when cooled at typical industrial cooling rates (1.7 - 0.12 K/sec). Glass compositions that fall outside this boundary will crystallize mineral phases consistent with the corresponding compositional phase field. This method can be used to predict steady-state, non-equilibrium behavior during liquid-phase sintering of Al_2O_3, and further presents the potential to predict elastic, thermal, and electrical properties.

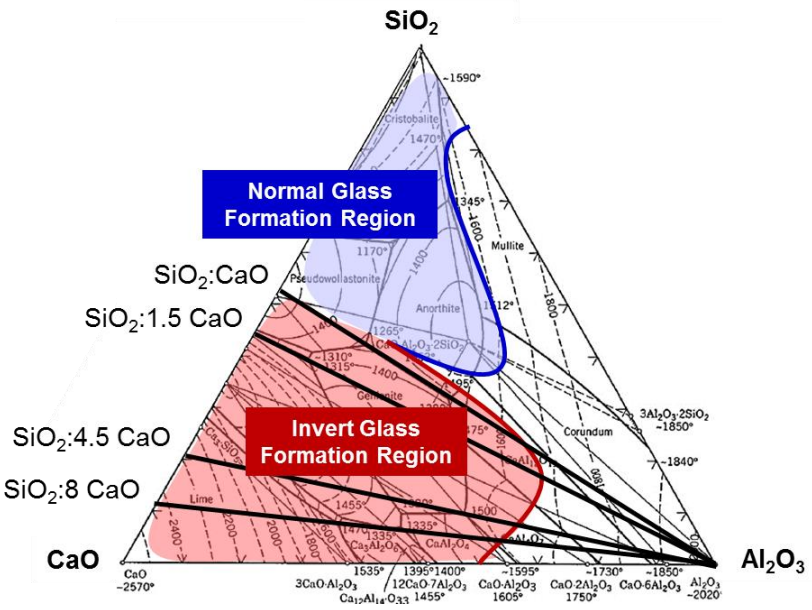

Figure 5.1. CaO-Al_2O_3-SiO_2 phase diagram with normal (blue) and invert (red) glass formation boundaries, as proposed by Lam.[41]

The GFB is further divided into "normal" and "invert" regions (Figure 5.1), where glass phase chemistries with SiO_2:CaO >1 are referred to as "normal" glasses, and glass phase chemistries with SiO_2:CaO <1 are referred to as "invert" glasses. Invert glasses are differentiated from normal glasses as the calcium ions structurally act more like glass formers in invert glass than modifiers, as in the case with normal glasses with SiO_2 as the glass former.[64] Invert glasses tend to have significantly higher fragilities than normal glasses and have been shown to have dramatically different properties, such as melting and glass transition temperatures, thermal expansion coefficient, refractive index, and density.[57, 65-67] These varying glass compositions are correspondingly expected to influence the microstructure evolution of Al_2O_3 in dissimilar ways. A third category of glass composition is considered in this work with SiO_2:CaO ~1, referred to as "boundary" glasses, where pockets of glass with both normal and invert compositions may exist in a sample, which has resulted in unpredictable behavior of these compositions in work to date. Only "boundary" and "invert" glass chemistries are considered in this study. The microstructure evolution of glass phase compositions in the "normal" region (SiO_2:CaO >1) was discussed in Chapter 4.

The addition of CaO has previously been observed to induce abnormal grain growth in Al_2O_3, producing plate-like grains as opposed to more uniform, equiaxed grains indicative of normal grain growth, such as those observed in Al_2O_3 with the addition of MgO.[14, 33, 35] Opposing the claim that the addition of CaO triggers abnormal grain growth in Al_2O_3, Chapter 4 demonstrated that when CaO is combined with SiO_2 in ratios of SiO_2:CaO > 1, normal rather than abnormal grain growth was observed, in addition to secondary crystallization of mullite ($3Al_2O_3 \cdot 2SiO_2$). Apart from grain growth behavior, secondary crystallization is also a concern for influencing macroscopic properties, as the formation of these phases and the varying properties they exhibit can influence properties such as strength, density, and electrical resistivity. In the sintering of Al_2O_3 with glass phase compositions in the CAS system, a wide variety of secondary phases have been reported to form in the grain boundaries, including anorthite ($CaO \cdot Al_2O_3 \cdot 2SiO_2$), gehlenite ($2CaO \cdot Al_2O_3 \cdot SiO_2$), mullite ($3Al_2O_3 \cdot 2SiO_2$), grossite ($CaO \cdot 2Al_2O_3$), and calcium hexaluminate ($CaO \cdot 6Al_2O_3$), also referred to as hibonite and CA_6 in the literature.[9, 14, 25, 36-38, 41, 43-44, 137-141] These reports do not always agree, as sintering conditions, glass phase

compositions and oftentimes justification for why particular secondary phases form over others, or if they form at all, vary widely.

The CAS system was selected for investigation because CaO and SiO_2 are two common impurities in industrial Al_2O_3 and many works have studied the effects of these oxides in high purity Al_2O_3 for comparison.[9-10, 14-15, 17-18, 25, 31, 33, 43-44] Considerable past work has also described the bulk forming ability of glasses in the CAS system, which can be compared to the predictions made using the GFB method.[56-57, 65, 67-68]

5.3 Experimental Procedure

5.3.1 Sample Preparation

Aqueous Al_2O_3 suspensions (CT 3000 LS SG, Almatis, Inc., Ludwigshafen, Germany) were combined with kaolin clay (EPK, Edgar Minerals, Inc., Hawthorne, FL) and calcium carbonate (Castle Carb 18, Oldcastle Industrial Minerals, Inc., Thomasville, PA) to generate samples with controlled SiO_2:CaO ratios. The batched molar ratios of SiO_2:CaO, and overall Al_2O_3 levels were calculated based on ICP-ES and loss on ignition (LOI) data for the batched components (Table 5.I). The four target glass phase compositions are represented by the tie lines of constant SiO_2:CaO molar ratios in Figure 1, including two aligned with eutectic points at 1512 and 1345°C, and one composition with only SiO_2 added.

The measured physical and chemical characteristics of the components used in this study are presented in Table 5.I. The Al_2O_3 powder was characterized via BET specific surface area (TriStar II, Micromeritics Instrument Co., Norcross, GA), He-pycnometry (AccuPyc II, Micromeritics Instrument, Co., Norcross, GA), and particle size distribution (SediGraph III PLUS, Micromeritics Instrument, Co., Norcross, GA). Chemical compositions were measured using inductively coupled plasma spectroscopy (ICP-ES) (Mineral Laboratories Canada, Bureau Veritas Commodities Canada, Ltd., Vancouver, BC, CA).

Table 5.I. Powder Characteristics of As-received Al_2O_3 and Batch Components

Al_2O_3 Powder Properties								
BET Specific Surface Area: 5.76 m^2/g				D_{50} Particle Size: 0.45 μm				
Density: 3.92 g/cm^3				D_{90} Particle Size: 1.89 μm				
Composition of Batch Components (wt%)	**Al_2O_3**	**SiO_2**	**CaO**	**MgO**	**Na_2O**	**K_2O**	**Fe_2O_3**	**LOI**
Al_2O_3	99.06	<0.01	0.01	0.06	0.01	<0.01	<0.04	0.90
EPK (Kaolin)	35.45	49.44	0.15	0.17	0.11	0.45	0.78	14.21
Whiting ($CaCO_3$)			56.03					43.97

Aqueous Al_2O_3 suspensions were combined with kaolin clay (EPK Kaolin, Edgar Minerals, Inc., Hawthorne, FL) and calcium carbonate (Castle Carb 18, Oldcastle Industrial Minerals, Inc., Thomasville, PA) to generate samples with controlled SiO_2:CaO ratios upon sintering. The batched molar ratios of SiO_2:CaO, and overall Al_2O_3 levels were calculated based on ICP-ES and loss on ignition (LOI) data for the batched components. The four target glass phase compositions are represented by the tie lines of constant molar SiO_2:CaO ratios in Figure 5.1 and are listed in Table 5.II.

All suspensions were prepared at 30 vol% solids loading and dispersed using a NH_4-PMAA polyelectrolyte (Darvan C-N, Vanderbilt Minerals, LLC, Norwalk, CT). The suspensions were slightly under-dispersed to prevent settling of the $CaCO_3$ during casting (0.3 mg/m^2 dispersion level). Sample suspensions were vibratory milled using Al_2O_3 media for several hours for mixing then slip cast into gypsum molds of discs approximately 2.5 cm in diameter. Samples were then dried at 100°C overnight and sintered in air for various time and temperature conditions (DT-29-FL-12-E3504, Deltech, Inc., Denver, CO).

Table 5.II. Target Glass Phase Compositional Molar Ratios of SiO_2:CaO

	SiO_2:CaO Ratio
Composition 1	1:1
Composition 2	1:1.5
Composition 3	1:4.5
Composition 4	1:8

5.3.2 Experimental Design Setup & Statistical Analysis

Statistical experimental design software was used to develop full factorial ANOVAs (analysis of variance) with variables of time, temperature, and Al_2O_3 level for each individual composition system.[134] The variables and levels investigated are presented in Table 5.III, which included twenty-seven randomized runs with five replicated points. This analysis was used to generate empirical densification models and determine significant variables for densification of each SiO_2:CaO ratio system. An analysis of the accuracy of using statistical models to represent densification of ceramics and justification of the selected factorial model for this experiment was discussed in Chapter 3.

Table 5.III. Experimental Design Factors and Levels for the Composition Systems Tested

Experiment Factor	**Levels Tested**		
	-1	0	1
Sintering Time (hours)	1	3	10
Sintering Temperature (°C)	1450	1500	1550
Alumina Level (wt%)	88	92	96

5.3.3 Sample Analysis

Bulk densities of post sintered samples were measured via immersion in water, corrected for small sample size (2-4 g).[127] Samples were ground into powder and skeletal densities were measured with a He-pycnometer (AccuPyc II 1340, Micromeritics Instrument Corp., Norcross, GA). Relative densities were then calculated as a percentage of bulk density to corresponding skeletal density and used to create empirical densification models with variables of time, temperature, and Al_2O_3 level. Ground samples were analyzed using powder x-ray diffraction (XRD) (D2 PHASER, Bruker Corporation, Billerica, MA), and phase ID was conducted using Diffrac.EVA software (Bruker Corporation, Billerica, MA) and the PDF 4+ 2019 database (ICDD, Newton Square, PA). Chemical analysis was completed via ICP-ES (Mineral Laboratories Canada, Bureau Veritas Commodities Canada, Ltd., Vancouver, BC, CA).

Samples were prepared for microstructure analysis by grinding and subsequent polishing to a 1 µm finish (MetLab Corp., Niagara Falls, NY), chemically etched in 10%

HF for 10 seconds to remove the glass phase, then thermally etched 50°C below the initial sintering temperature to reveal grain boundaries, as described in Chapter 2. After etching, sample microstructures were analyzed via scanning electron microscopy (SEM) (ESEM, Quanta 200, FEI Company, Hillsboro, OR).

5.3.4 Grain Size Analysis

For samples with no secondary crystallization visible in SEM micrographs, average grain sizes were measured via the Abrams Three-Circle Procedure following ASTM Standard E112.[75] For microstructures with significant secondary crystallization, the standards for linear intercept methods do not adequately account for multi-phase systems, the majority of which assume microstructures consist of equiaxed, polyhedral grains that exhibit normal grain growth.[77] Other standards, such as ASTM E1181, account for samples with multiple distributions of a single phase, and literature recommendations for multi-phase systems only suggest measuring volume fractions via a point count method, neither of which apply to this study.[73, 80] Instead, for samples with significant secondary phase(s) present, a variation of the Abrams Three-Circle Procedure was used. Figure 5.2 is a schematic of an example microstructure from this study consisting of Al_2O_3 grains and an interspersed $CaO{\cdot}6Al_2O_3$ secondary phase. Table 5.IV outlines the method used to calculate the average Al_2O_3 grain size using a proportion of the total intercepts between the two phases.

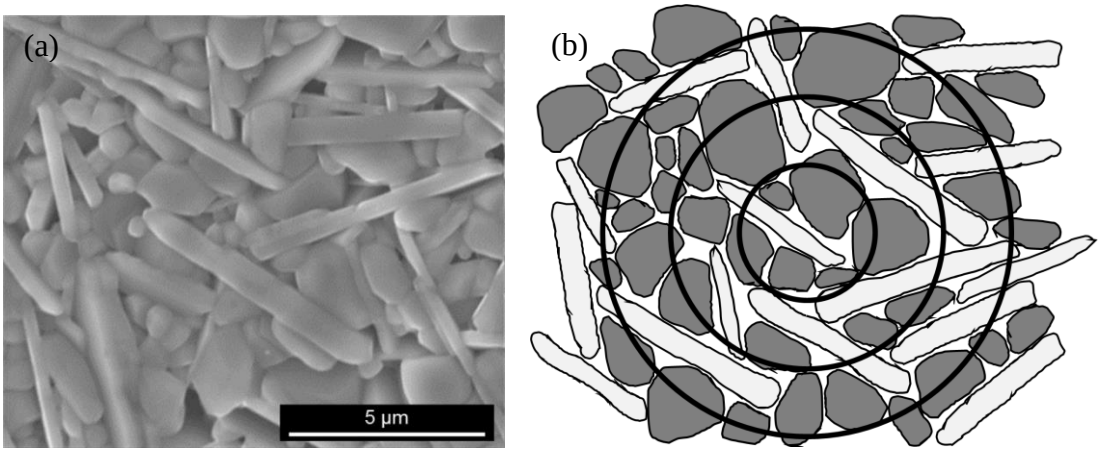

Figure 5.2. (a) Example Al_2O_3 microstructure with interspersed $CaO{\cdot}6Al_2O_3$ secondary phase and (b) a schematic representation of the method used to approximate Al_2O_3 grain sizes.

Table 5.IV. Outline of the Method Used to Calculate Average Grain Size of Al_2O_3 Grains with an Interspersed Secondary Phase

Number of intercepts Al_2O_3 grains over all circles	35
Number of intercepts secondary phase over all circles	17
Total number of intercepts	52
Fraction of total intercepts of Al_2O_3 grains	$\frac{35}{52} = 0.67$
Total length of test circles	714.8 mm
Proportion of test circle length to Al_2O_3	(0.67) 714.8 mm = 481.12 mm
Scale conversion (length of scale bar)	$\frac{5\ \mu m}{64\ mm}$
Number of Al_2O_3 intercepts per length proportion Al_2O_3 (μm)	$\frac{35\ ints}{481.12\ mm}\frac{64\ mm}{5\ \mu m} = 0.93$ ints/μm
Average length of Al_2O_3 grain (diameter)	$\frac{1\ \mu m}{0.93\ ints} = 1.08\ \mu m$
Average Al_2O_3 grain diameter (Proportioned using Mendelson 3-dimensional factor[77])	1.08 μm (1.56) = **1.68 μm**

5.4 Results & Discussion

5.4.1 Densification Behavior

Table 5.V summarizes the results of the statistical analysis/ANOVA for the four SiO_2:CaO compositions evaluated. All compositions follow linear models for densification and their respective significant variables can be grouped using the relative ratios of SiO_2:CaO. The "boundary" compositions with SiO_2:CaO ≈ 1 revealed only Al_2O_3 to be significant for densification while compositions with SiO_2:CaO < 1 indicated both Al_2O_3 level and temperature were significant. No time dependence was observed on the scale investigated in this study, which was modelled to mimic sintering times commonly used in industry (approximately 1-10 hours). A further discussion of how the statistical models can be used to predict and optimize sintering conditions for these systems was addressed in Chapter 3.

Table 5.V. Best Fit Models, Significant Factors, and Density Equations Determined from Full Factorial Designs

		Best Fit Model	Significant Factors
Boundary Region	1 SiO_2 : 1 CaO	Linear	Al_2O_3 Level
	1 SiO_2 : 1.5 CaO	Linear	Al_2O_3 Level
Invert Region	1 SiO_2 : 4.5 CaO	Linear	Temperature Al_2O_3 Level
	1 SiO_2 : 8 CaO	Linear	Temperature Al_2O_3 Level
Equations for Percent Relative Density (input in experimental units)			
1 SiO_2 : 1 CaO	= 90.93 + 0.08(Al_2O_3 Level)		
1 SiO_2 : 1.5 CaO	= 89.19 - 0.43(Time) + 0.09(Al_2O_3 Level)		
1 SiO_2 : 4.5 CaO	= -95.60 + 0.07(Temp.) + 0.81(Al_2O_3 Level)		
1 SiO_2 : 8 CaO	= 62.84 + 0.06(Temp.) - 0.75(Al_2O_3 Level)		

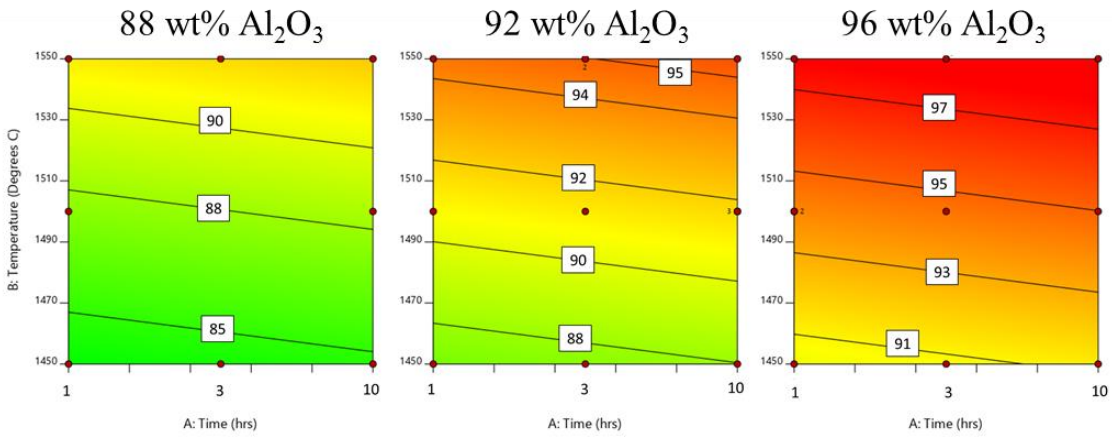

Figure 5.3. Temperature versus time densification contours with glass phase composition 1 SiO_2 : 4.5 CaO at varying Al_2O_3 levels.

5.4.2 Chemical and Phase Analysis

Table 5.VI presents chemical compositions for the sample chemistries generated, measured via ICP-ES, compared to the target sample compositions. Based on this data, the Al_2O_3 levels achieved during sintering were within ~0.1-2.5% error of the target values. Also listed in Table 5.VI are the achieved and target ratios of SiO_2:CaO for the various sample compositions, which can also be seen on the CAS diagram in Figure 5.5.

Even small deviations in SiO_2 or CaO levels can significantly change the resulting component ratio; however, those achieved are within reasonable agreement with the target values and follow the desired trends with respect to changing composition. The known chemical compositions of these samples combined with XRD can be used to determine secondary phases formed in these samples during sintering.

Table 5.VI. ICP-ES Chemistries of Selected Glass Phase Compositions with Measured and Target Al_2O_3 Levels and SiO_2:CaO Ratios (all samples fired at 1500°C for 1 hour)

Target Al_2O_3 Level (wt%)	**Measured Al_2O_3 Level (wt%)**			
	1 SiO_2 : 1 CaO	**1 SiO_2 : 1.5 CaO**	**1 SiO_2 : 4.5 CaO**	**1 SiO_2 : 8 CaO**
88	89.47	90.55	91.61	91.58
92	92.18	92.72	93.95	94.2
96	95.27	95.15	96.71	96.86
Target SiO_2:CaO Ratio (mol)	**Measured SiO_2: CaO Ratio (mol)**			
	88 wt% Al_2O_3	**92 wt% Al_2O_3**	**96 wt% Al_2O_3**	
1:1 (1)	1.56	1.87	1.87	
1:1.5 (0.67)	0.97	1.32	1.91	
1:4.5 (0.22)	0.27	0.42	0.37	
1:8 (0.12)	0.16	0.26	0.18	

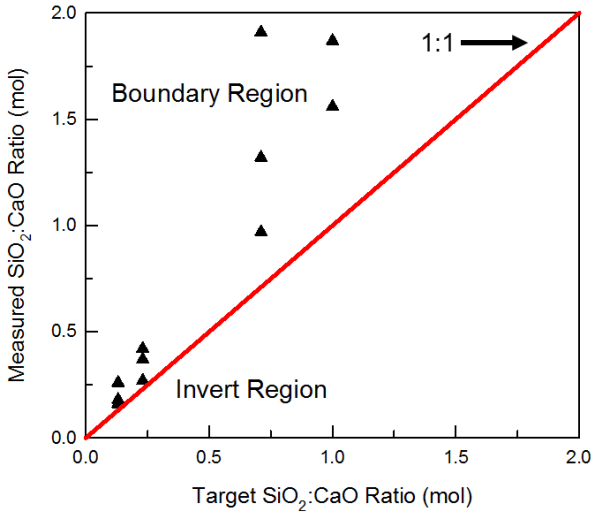

Figure 5.4. Measured versus target SiO_2 ratios for the four composition systems investigated, measured under the same conditions as in Table VI.

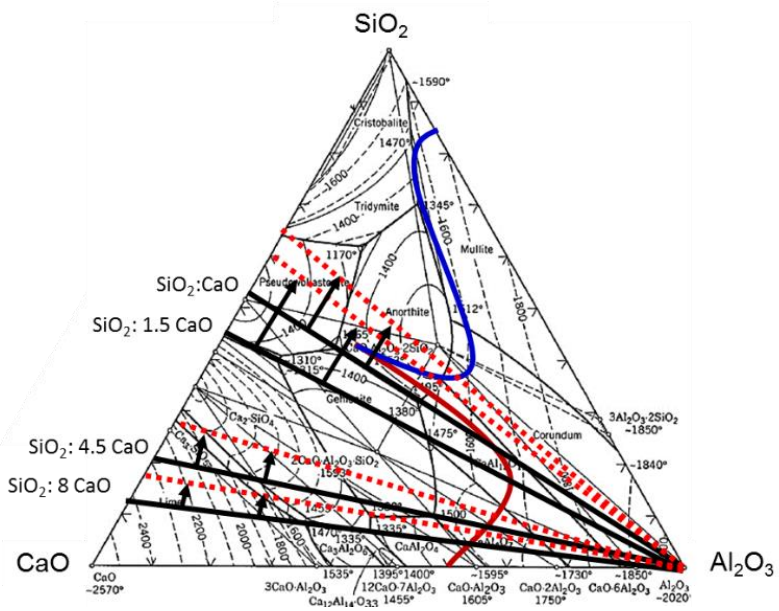

Figure 5.5. CAS phases diagram with SiO_2:CaO ratios of target compositions (bold lines) and those achieved (dashed lines).

Since other alkali and alkaline earth oxides such as Na_2O and K_2O have been observed to volatilize over time at elevated temperatures, samples with high CaO levels (1 SiO_2 : 8 CaO) were analyzed to ensure no volatilization occurred for the temperature and time ranges investigated. Samples of the same composition were sintered for 0.3 (20 minutes), 1, and 30 hours and chemically analyzed via ICP-ES (Figure 5.6). No significant decline in CaO content or change in composition was observed.

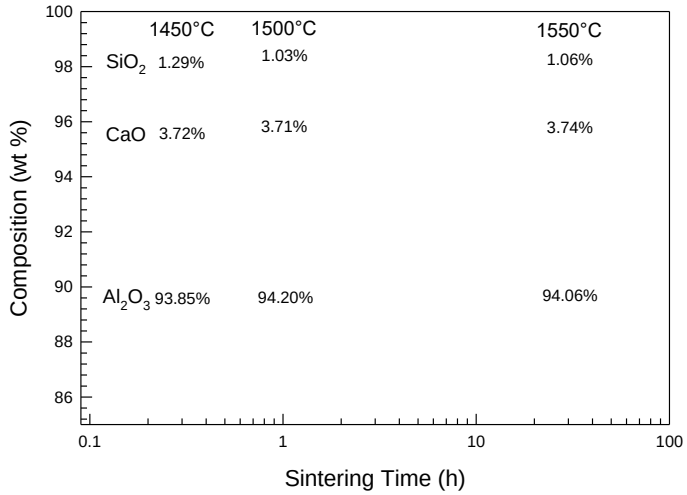

Figure 5.6. ICP-ES data with measured chemical compositions as a function of sintering time and temperature for samples with 1 SiO_2 : 8 CaO.

XRD was used to confirm the presence of secondary phases in a selection of samples with conditions from this study (time, temperature, Al_2O_3 levels and SiO_2:CaO ratios), summarized in Table 5.VII. Corundum (α-Al_2O_3) and a small amorphous hump indicative of a glass phase were present in all samples analyzed, but are omitted in Table 5.VII. The amorphous hump was observed to increase in intensity with decreasing Al_2O_3 level (i.e. more liquid/glass forming additives present in the material). The most likely phase expected to crystallize from the liquid melt based on the CAS diagram for the compositions under investigation (Figure 5.1) and the GFB is hibonite ($CaO{\cdot}6Al_2O_3$). The hibonite phase field lies outside of the glass formation region for this system, as shown by the shaded region in Figure 5.7, and was present in roughly 32 out of 35 analyzed samples.

Table 5.VII. Crystalline Phases Identified via XRD for Varying SiO_2:CaO Ratios and Sintering Conditions

SiO_2:CaO Ratio	Time (h)	Temp. (°C)	Al_2O_3 Level (wt%)	Hibonite ($CaO·6Al_2O_3$)	Anorthite ($CaO·Al_2O_3·2SiO_2$)	Gehlenite ($2CaO·Al_2O_3·SiO_2$)	Grossite ($CaO·2Al_2O_3$)
1:1	1450	1	96	x	x	x	
	1450	3	88	x	x	x	
	1450	3	92	x	x	x	
	1450	3	96	x			
	1450	10	92	x	x	x	
	1500	1	96	x	x	x	
	1500	3	88	x	x	x	
	1500	3	96	x	x		
	1500	10	88	x	x	x	
	1550	10	88	x			
1:1.5	1450	1	96	x		x	
	1450	3	88	x	x	x	
	1450	3	92	x	x	x	
	1450	3	96	x			
	1450	10	92	x	x	x	
	1500	1	92	x	x	x	
	1500	3	88		x		x
	1500	3	96	x		x	
	1500	10	88	x	x	x	
	1550	10	88	x	x		
	1550	10	96	x	x		
1:4.5	1450	3	88	x			
	1450	3	92	x			
	1450	3	96	x			x
	1500	3	88	x			x
	1500	3	96			x	x
	1550	10	88	x			
	1550	10	96	x			
1:8	1450	3	88	x			x
	1450	3	96	x		x	
	1500	3	88	x			
	1500	3	96			x	x
	1550	10	88	x			
	1550	10	96	x			

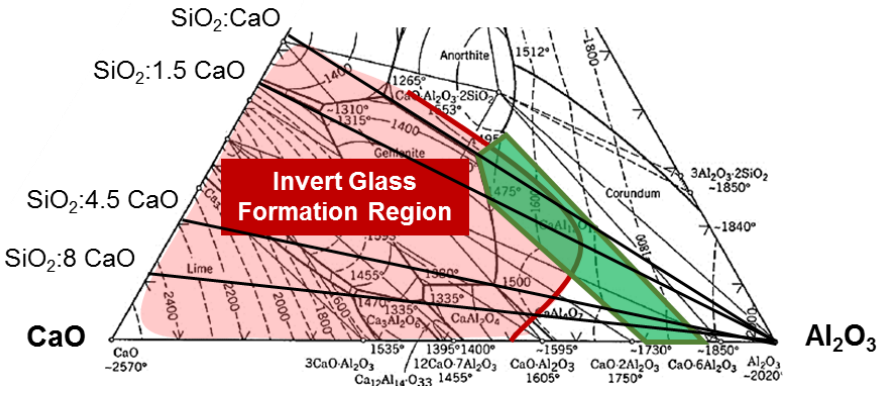

Figure 5.7. Hibonite ($CaO \cdot Al_2O_3$) phase field (green shaded region) within the CAS system.

Example XRD patterns are presented in Figure 5.8 for two samples to demonstrate the various crystalline phases detected. Both samples were sintered at 1500°C for 3 hours with 88 wt% Al_2O_3. The bottom pattern in Figure 5.8 is within the invert range and reveals only corundum (Al_2O_3) and hibonite present. For the boundary compositions (SiO_2:CaO ≈1), anorthite ($CaO \cdot Al_2O_3 \cdot 2SiO_2$) and gehlenite ($2CaO \cdot Al_2O_3 \cdot SiO_2$) were present in addition to hibonite in many samples (the top pattern in Figure 5.8). Since the glass formation regions for these compositions lie to the right of both the anorthite and gehlenite phase fields, it is proposed these secondary phases formed during solid state reactions at temperatures below liquid formation, rather than as reaction products from the liquid melt. Previous work has demonstrated anorthite and gehlenite formation within the CAS system at temperatures as low as 954°C and 933°C, respectively, and anorthite has also been reported in studies of under-fired glazes.[41, 60, 137-138] Because the formation of these phases occurred at lower temperatures than corresponding eutectic temperatures for anorthite (1345°C) and gehlenite (1380°C), these results have all been attributed to solid state reactions.

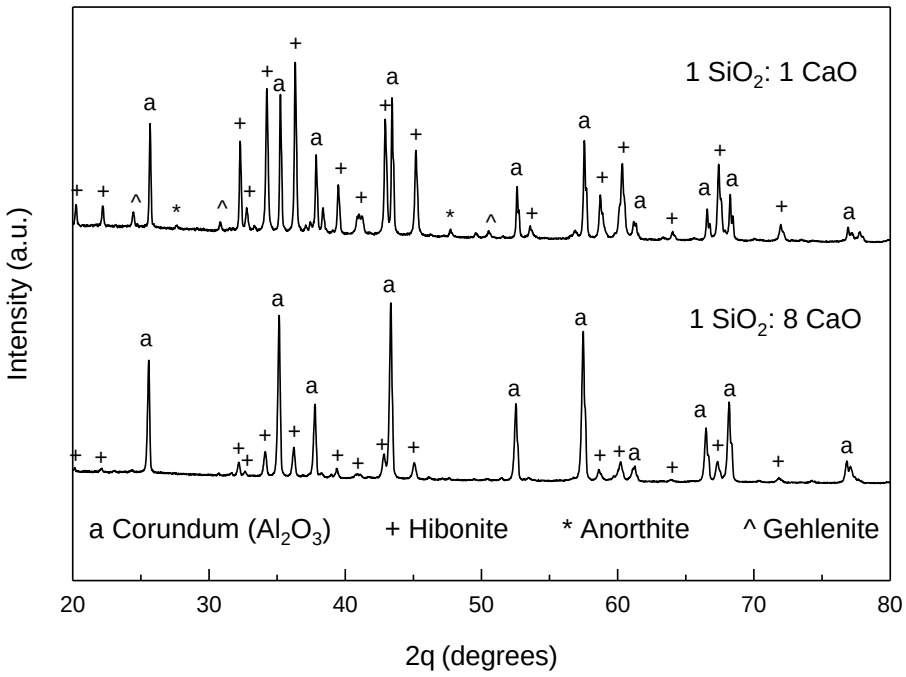

Figure 5.8. Sample XRD patterns with identified secondary phases.

Grossite ($CaO{\cdot}2Al_2O_3$) was also detected in several samples in the invert glass composition range (SiO_2:CaO < 1) at 1450 and 1500°C. Based on the GFB, grossite is also predicted to form due to a solid state reaction rather than crystallizing from the liquid melt upon cooling. Svancarek et al. observed the secondary formation of anorthite, gehlenite, and grossite in Al_2O_3 at 1450°C, which corresponds with the formation temperatures observed in this study.[9, 139] Lam predicted that within the CAS system, a temperature of around 1550°C or higher would be required to cause increased Al_2O_3 dissolution in the liquid phase necessary to breakdown secondary phases such as anorthite.[41] In samples sintered at 1550°C, only hibonite was observed to form in all but one case, which supports the proposal that anorthite, gehlenite, and grossite are dissolved into the liquid phase near 1550°C.

Another topic to note is the high intensity of the hibonite phase detected in most samples, especially in the invert glass compositions (SiO_2:CaO < 1). The intensities of the hibonite phase were significantly greater than those of the other secondary phases detected in all cases, as shown in Figure 5.8, implying there is significantly more hibonite present in the samples than any of the other phases. With the solid state reactions of anorthite, gehlenite, and grossite, combined with significant hibonite crystallization, the composition

of the glass phase would be expected to shift from the compositions predicted by the GFB. Hibonite formation would remove significant CaO from the glass/liquid phase, resulting in a higher SiO_2:CaO ratio than predicted for each composition. In addition, regions of non-uniform chemistry may occur during sintering due to the large particle size of the batched CaO powder source ($CaCO_3$) compared to the smaller particle size of the SiO_2 source (EPK clay). This discrepancy may result in pockets of high CaO concentrations, which may have also contributed to the high hibonite crystallization levels observed.

5.4.3 The Role of Temperature on Grain Growth

Figures 5.9 and 5.10 present microstructures and average grain sizes for the SiO_2:CaO chemistry ratios investigated with varying sintering temperature. Due to the significant extent of secondary phase crystallization in the two compositions with the greatest CaO content (SiO_2:CaO = 1:4.5 and 1:8), no reliable Al_2O_3 grain size measurements could be made on these samples, so only qualitative micrograph comparisons are presented. The included grain size data in Figures 5.9 and in the proceeding figures for SiO_2:CaO ratios in the normal glass formation region (SiO_2:CaO = 1:0, 1:0.15, and 1:0.33) were prepared and measured using the same method as described in this chapter and their influence on microstructure evolution was discussed in Chapter 4.

As can be observed in Figure 5.9, secondary crystallization increases with increasing CaO content and the grain size of Al_2O_3 grains is visibly reduced. In cases where no visible significant secondary crystallization occurred (SiO_2:CaO = 1:1 and 1:1.5), the Al_2O_3 grains exhibit equiaxed shape and normal grain growth, and increasing grain size with increasing temperature. For the compositions with higher CaO content (SiO_2:CaO = 1:4.5 and 1:8), the increased crystallization of hibonite ($CaO{\cdot}6Al_2O_3$) occupies increasing fractions of Al_2O_3 for the formation of hibonite, which then impinge on the Al_2O_3 grains and appear to hinder their growth. These trends are observable quantitatively in Figure 5.10 for the two "boundary" compositions, as well as three compositions in the "normal" glass formation chemistry region (SiO_2:CaO>1). The Al_2O_3 grain size increases with increasing CaO content to the point where excessive secondary phase formation takes place, where a decrease in Al_2O_3 grain size then occurs. The invert compositions follow similar trends to the normal compositions, with increasing grain size with temperature; however, the rate of

grain size change appears to be smaller than the rate for the normal glass composition samples with SiO_2:CaO = 1:0.15 and 1:0.33. Instead, the growth rates more closely resemble the glass phase composition with no additional CaO (SiO_2:CaO = 1:0).

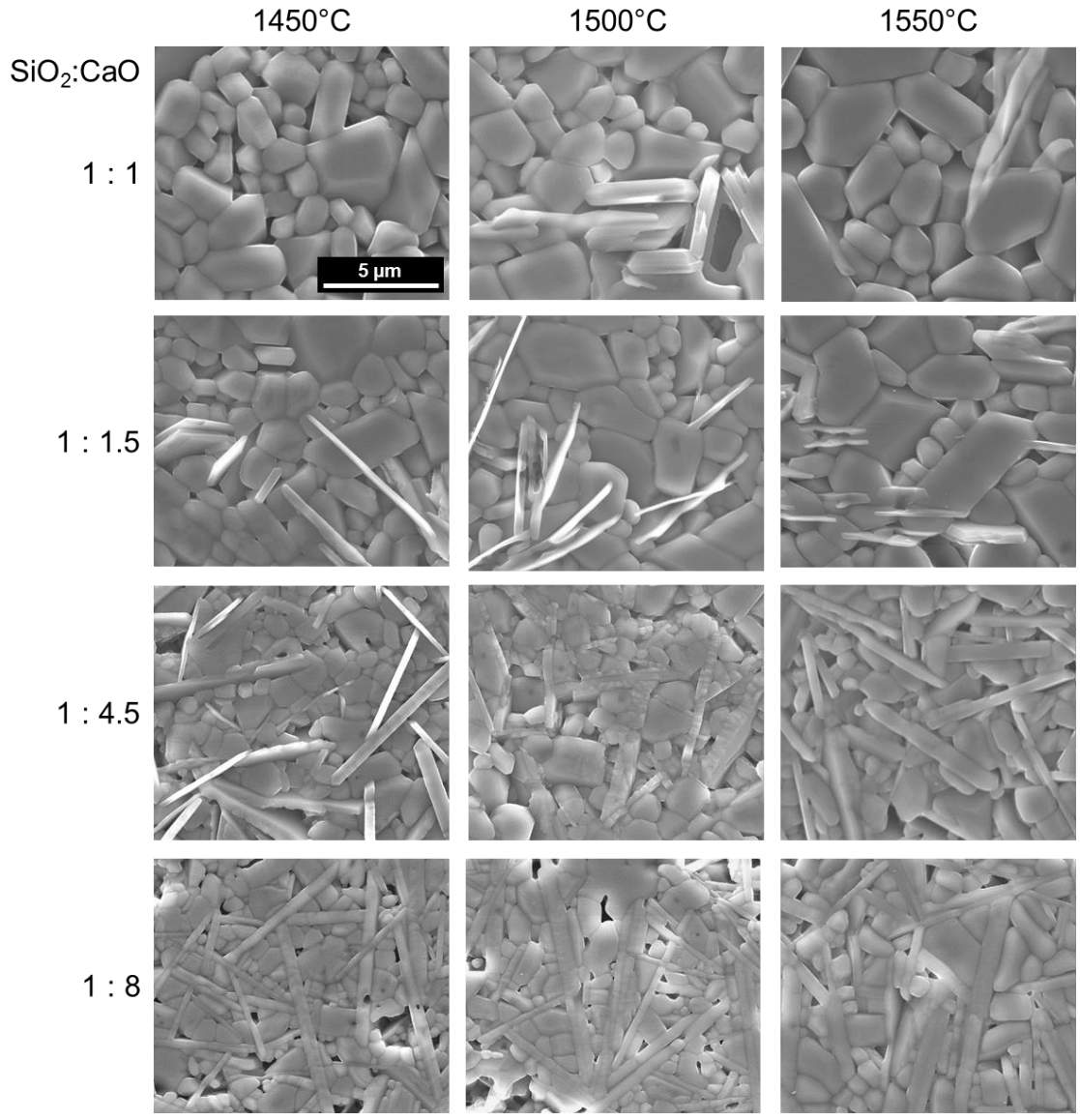

Figure 5.9. Microstructures of varying SiO_2:CaO ratios sintered for 3 hours at 1450, 1500, and 1550°C, all 92 wt% Al_2O_3 level (all images at the same magnification).

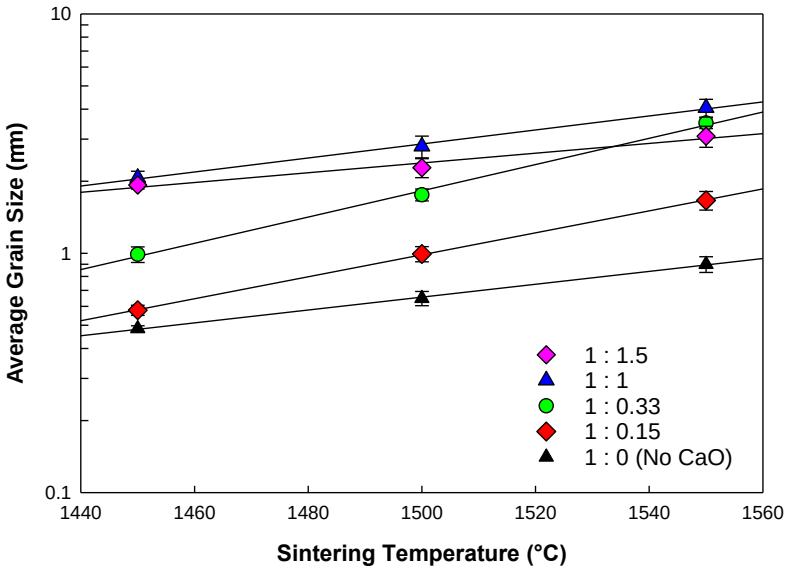

Figure 5.10. Average grain size versus sintering temperature for varying SiO_2:CaO ratios, all sintered for 3 hours with 92 wt% Al_2O_3.

5.4.4 The Role of Time on Grain Growth

Figures 5.11 and 5.12 present microstructures and average grain sizes for varying SiO_2:CaO compositions for sintering times between 20 minutes and 30 hours. Similar to the observation in Figure 5.9, Figure 5.11 displays increasing quantities of secondary phase (mainly hibonite and anorthite) with increasing CaO content, to the extent where few Al_2O_3 grains remain in the microstructures for SiO_2:CaO = 1:8. In every case, larger overall Al_2O_3 grain sizes can be observed with longer sintering times, since there is a longer duration for grain growth to take place during sintering. Figure 5.12 presents average grain size data for SiO_2:CaO = 1:1 and 1:1.5, as well as several SiO_2:CaO ratios in the "normal" glass forming region of the CAS diagram. Al_2O_3 grain size is observed to increase with increasing CaO content up until the point where excessive secondary crystallization occurs in the SiO_2:CaO = 1:8 composition, where average grain size then decreases.

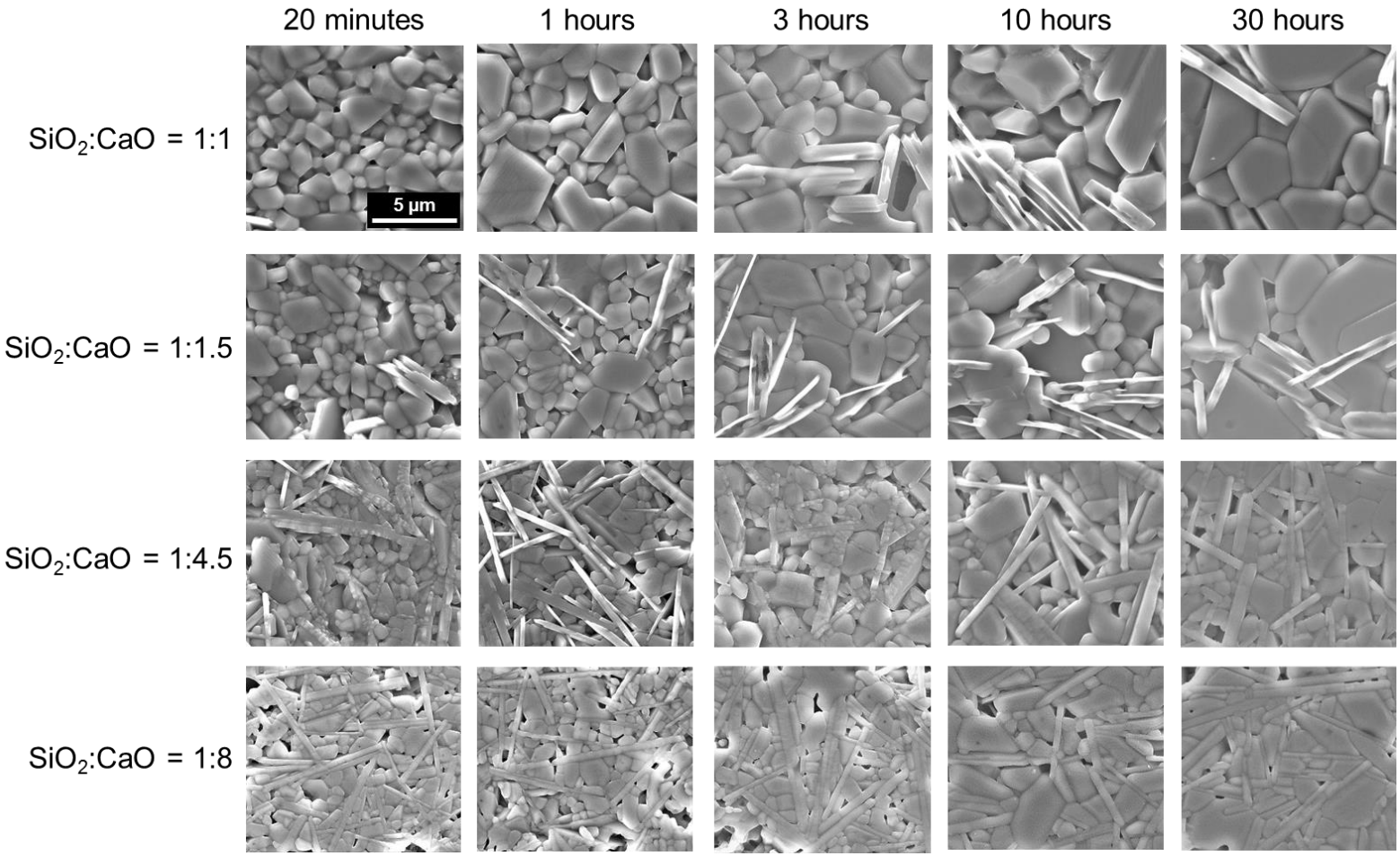

Figure 5.11. Microstructures of varying SiO_2:CaO ratios sintered at 1500°C for times between 20 minutes and 30 hours, all at 92 wt% Al_2O_3 (all images at the same magnification).

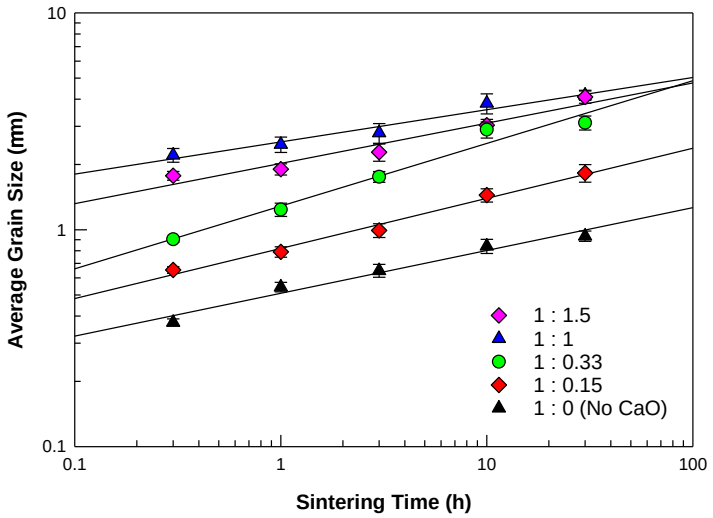

Figure 5.12. Average grain size versus sintering time for glass phase compositions of varying SiO_2:CaO ratios, all sintered at 1500°C with 92 wt% Al_2O_3.

Table 5.VII lists grain growth rates for the data presented in Figure 5.12 from linear regression best-fit lines. The three compositions in the normal glass region (SiO_2:CaO > 1) have relatively similar grain growth rates of about 0.2 μm/hour, while the two boundary compositions (SiO_2:CaO ≤ 1) exhibit lower grain growth rates. This grain growth behavior is likely related to the densification trends observed, where the behavior of the varying compositions can be grouped by the relative ratios of SiO_2:CaO in the system. The reduction in growth rates observed in the invert compared to the normal compositions is proposed to be due to increased secondary phase formation in the invert cases, which removes CaO from the glass. Reduced CaO quantities will increase the viscosity of the glass and slow diffusion processes that contribute to grain growth, resulting in smaller grain sizes.

Table 5.VIII. Measured Grain Growth Rates for Samples in Figure 5.12

SiO_2:CaO Ratio	**Grain Growth Rate (μm/hour)**
1:1.5	0.186
1:1	0.149
1:0.33	0.289
1:0.15	0.231
1:0	0.197

5.4.5 The Role of Al_2O_3 Level on Grain Growth

Microstructures and average grain sizes for varying SiO_2:CaO ratios at the three Al_2O_3 levels investigated are presented in Figures 5.13 and 5.14, where the remaining wt% of the composition is assumed to be liquid-phase forming constituents. In the case of varying Al_2O_3 levels, there does not appear to be a significant change in microstructure with changing Al_2O_3 level. This lack of a definitive trend was also observed in the glass phase compositions with SiO_2:CaO >1 (Figure 5.14). Similarly to the previous figures, grain size increases with increasing SiO_2:CaO content to the point where significant secondary phase formation occurs at SiO_2:CaO = 1:1.5. Beyond this point with increasing CaO content, the secondary phase formation is so prevalent that it hinders the growth of Al_2O_3 grains, as supported by observing Figure 5.13, moving from top to bottom. The secondary phase formation also appears to severely hinder densification with decreasing Al_2O_3 level and increasing CaO content, which is evident for the 88% Al_2O_3 sample in Figure 5.13 in the two bottom SiO_2:CaO ratios.

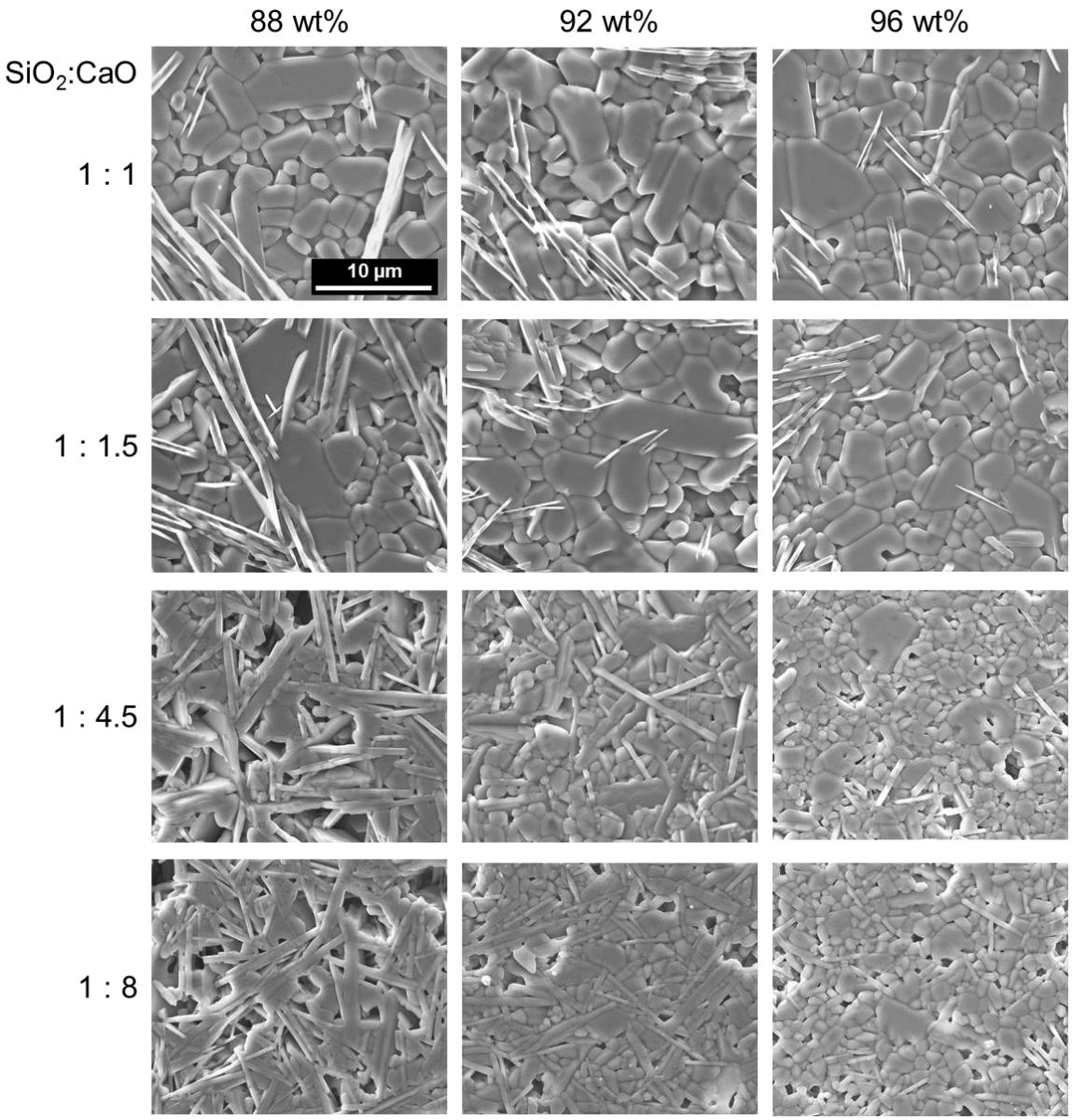

Figure 5.13. Microstructures of varying SiO_2:CaO ratios at each of the three investigated Al_2O_3 levels, all sintered for 10 hours at 1500°C (all images at the same magnification).

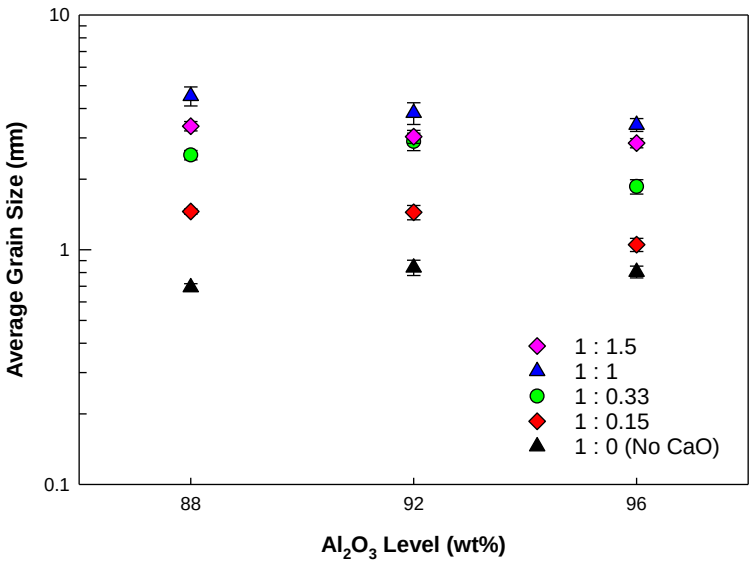

Figure 5.14. Average grain size versus Al_2O_3 level for varying SiO_2:CaO ratios, all sintered for 10 hours at 1500°C.

5.5 Conclusions

This study investigated the densification and grain growth behavior of industrial grade Al_2O_3 sintered with glass phase chemistries in the CaO-Al_2O_3-SiO_2 system containing SiO_2:CaO ≤ 1. A strong effect of glass phase chemistry on both densification and grain growth behavior was observed for varying SiO_2:CaO ratios. The behavior of these compositions could be grouped by the relative ratios of SiO_2:CaO. A variety of secondary phases were observed to form from the liquid phase during sintering, the most common of which being hibonite ($CaO \cdot 6Al_2O_3$), which is predicted to crystallize based on the Glass Formation Boundary theory. The other detected phases are believed to form during a solid state reaction at a lower temperature than when the liquid phase forms. No abnormal grain growth was observed in the Al_2O_3 grains, however, significant secondary crystallization hinders the grain growth of Al_2O_3 with increasing CaO content. When compared to systems with SiO_2:CaO > 1, as presented in Chapter 4, the average grain size of Al_2O_3 grains was observed to increase with increasing CaO content up to the point where excessive secondary crystallization occurred (SiO_2:CaO < 1:1).

6. THE EFFECTS OF AGGLOMERATION ON SINTERING OF BAYER PROCESS Al_2O_3 COMPARED TO NON-BAYER PROCESS Al_2O_3

6.1 Abstract

While the majority of alumina (Al_2O_3) used in industry is produced via the Bayer process, a typical pitfall of these powders is an inability to achieve full relative density during sintering. This work proposes this failure to densify is due to large hard-agglomerates inherit in Bayer process Al_2O_3. Two Al_2O_3 powders, both a Bayer process Al_2O_3 and high purity Al_2O_3 produced via a chemical synthesis route, were analyzed for the presence of agglomerates and their corresponding densification behavior. A new method was proposed to analyze particle size distributions, derived from how flaw distributions are represented in fracture mechanics on a probability axis. By using this method of representing particle size, it was demonstrated that agglomeration can be more easily detected than by using a traditional cumulative mass percent approach. Both wet milling and sedimentation techniques were demonstrated to be effective methods to remove the agglomerates in Bayer process Al_2O_3 and to effectively normalize the particle size distributions.

6.2 Introduction

More than 90% of alumina (Al_2O_3) used for industrial applications is derived from bauxite, produced via the Bayer process, which typically produces a powder with purities in the range of 99.0-99.9%.[1, 51, 142] It is commonly observed in Bayer-process Al_2O_3 that powder systems sintered in air do not reach full relative density, but rather follow an asymptotic relationship below 100% density.[5, 7, 13, 26-27, 52-53] An example of this effect is presented in Figure 6.1 through the densification curves for a Bayer process Al_2O_3 sintered for various times at 1500 and 1550°C. Even after extensive sintering times (10-30 hours), this system only achieves a maximum of 99% relative density. This trend of incomplete densification is proposed to be due to agglomerates inherent in the powder synthesis process, which are suggested to pin pores during sintering and prevent full densification. The effect of large pores becoming "trapped" in Al_2O_3 microstructures is seen in cast bodies of both as-received Al_2O_3 (Figure 6.2(a)) and when significant liquid forming

additives are added into the system (Figure 6.2(b)). The pores in Figure 6.2 are in the range of 10-20 μm in diameter, which is an order of magnitude larger than the 0.5 μm average particle size for the Al_2O_3 powder. The presence of such large porosity in both sample types suggests the pore-pinning mechanism originates from the powder rather than an effect from gas trapping or bubble formation from the liquid constituents during sintering. Hard agglomerates such as those proposed in Bayer-process Al_2O_3 can only be further reduced or removed by subsequent processing such as milling or grinding after production, as methods to break up soft agglomerates such as ultra-sonication is not effective. Whereas lower purity and less desirable powder uniformity are shortcomings of Bayer-process Al_2O_3, an advantage over powders synthesized through other methods is a significant reduction in cost.

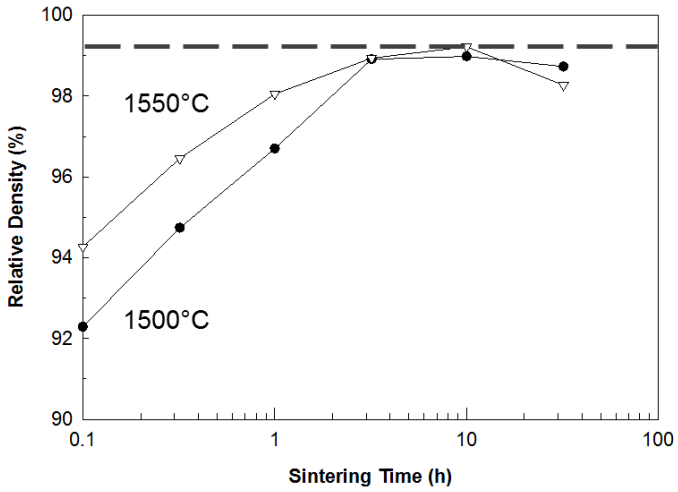

Figure 6.1. Densification curves for Bayer-process Al_2O_3 sintered for times between 0.1-30 hours at 1500 and 1550°C. Samples dispersed at 30 vol% and slip cast before sintering.

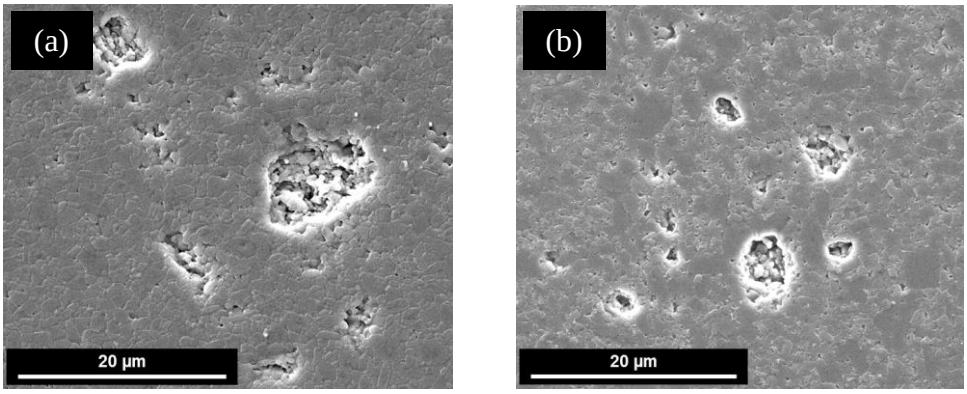

Figure 6.2. (a) 99.8 wt% Al_2O_3 sintered at 1500°C for 10 hours and (b) 86 wt% Al_2O_3 sintered at 1400°C for 30 hours. Samples dispersed at 30 vol%, ultrasonicated, and slip cast before sintering.

It has been proposed previously that particle size distributions (PSDs) can be represented similarly to flaw distributions in fracture mechanics by using a probability axis.[79, 143-144] If plots of probability versus log of particle size are linear in nature, this indicates the PSD follows a log-normal statistical distribution (Figure 6.3(a)). Correspondingly, if the PSD plotted on a Weibull probability scale versus log of particle size is linear, the PSD follows a Weibull distribution. Figure 6.3 demonstrates how various particle size distributions appear when plotted on both a normal (Gaussian) and (Weibull) probability axes.

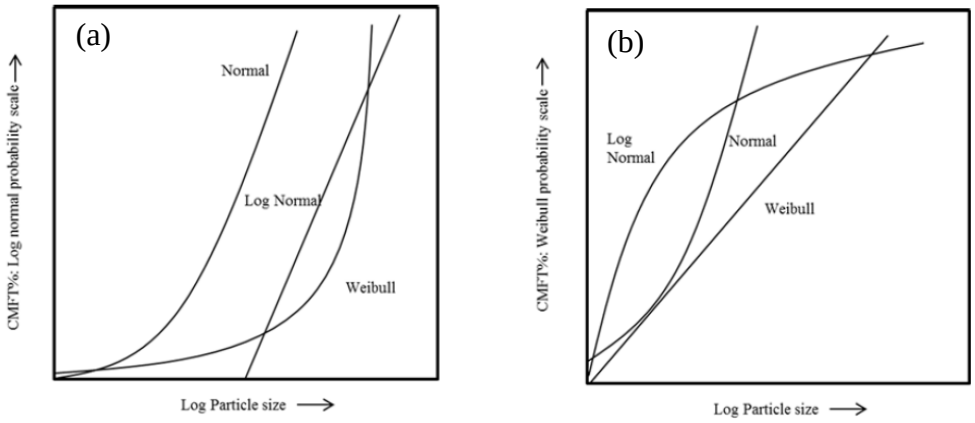

Figure 6.3. Distributions of particle sizes represented on (a) a Gaussian (normal) probability axis and (b) a Weibull probability axis.[144]

This method of analyzing statistical distributions of particle sizes was used in a study of various milled industrial powders to analyze their distributions, some of the results of which are presented in Figure 6.4.[144] Particle size distributions are represented on both a traditional cumulative mass finer than (CMFT) axis (Figure 6.4(a)) and on Gaussian (normal probability) axes (Figure 6.4(b)). Traditionally, particle size distributions have been represented on a CMFT linear scale with the assumption that all ground powders follow a log-normal distribution; however, Figure 6.4(a) demonstrates that this is clearly not always the case.[145-151]

While the traditional method of analyzing PSDs reports the average particle size by mass when plotted on a CMFT axis (D_{50}, D_{90} etc.), an easy determination of the normality or abnormality of a PSD can be determined by the linearity (or non-linearity) of fit when plotted on a probability axis. It was observed that powder statistical distributions can be grouped by the method in which powders were prepared (i.e. milling, precipitation) and by the cleavage planes the materials exhibit during fracture. Ground powders with well-defined cleavage planes (calcium carbonate, crystalline calcium fluoride, garnet, silicon carbide, etc.) were observed to follow a log-normal distribution, while powders without well-defined cleavage systems (tabular Al_2O_3, glass frit, quartz, etc.) were reported to follow a Weibull distribution. An interesting finding from this study revealed that calcined Al_2O_3 did not follow normal distributions like the other ground powers. The tail end of these distribution at higher mass percentages deviated from linear, log-normal, or Weibull behavior, as can be observed in Figure 6.4(b) for calcined alumina. This deviation is proposed to be due to agglomerates present in calcined Al_2O_3, which this study attempts to address.

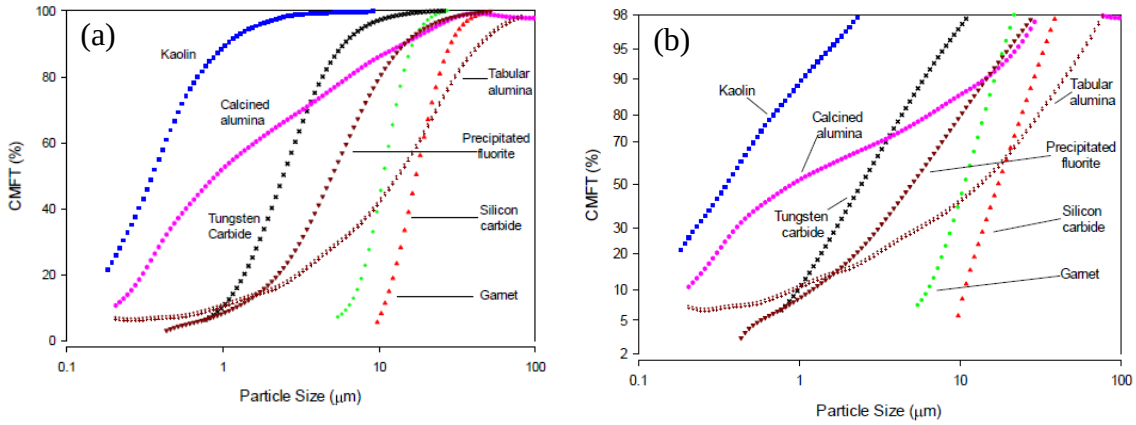

Figure 6.4. Cumulative Mass Finer Than (CMFT) particle size distributions plotted on (a) a linear axis versus log particle size, and (b) a Gaussian (normal) probability axis versus log particle size.[144]

6.3 Experimental Procedure

The physical and chemical characteristics of the two Al_2O_3 powders used in this study are listed in Table 6.I (CT 3000 LS SG, Almatis, Inc., Ludwigshafen, Germany; APA-0.5, Sasol North America, Inc., Ceralox Division, Tucson, AZ). The two powders were selected as examples of a typical Bayer-process Al_2O_3 (99.8%) and a high purity Al_2O_3 (>99.9%) derived from an alumina alkoxide precursor. All PSD measurements were performed using aqueous suspensions at 3 vol% solids loading and dispersed at 0.4 mg/m^2 with a NH_4-PMAA polyelectrolyte (Darvan C-N, Vanderbilt Minerals, LLC, Norwalk, CT). Particle suspensions were then measured using an X-ray particle size analyzer after ultra-sonication for approximately one minute (SediGraph III PLUS, Micromeritics Instrument, Co., Norcross, GA). For samples sintered and measured for achieved density, sample bulk densities were first measured using an immersion method modified for a small sample size (2-5 grams).[127] Samples were then ground into powder and skeletal densities were measured using He-pycnometry (AccuPyc II 1340, Micromeritics Instrument Corp., Norcross, GA). Relative densities were then calculated as a percentage of the bulk density achieved to the skeletal density.

Table 6.I. Powder Characteristics of As-received Powder for a Bayer Process and Non-Bayer Process Al_2O_3 (as reported from suppliers)

Bayer Process Al_2O_3		**Non-Bayer Process Al_2O_3**	
SSA (m^2/g)	8.9	SSA (m^2/g)	7.5
D_{50} (μm)	0.5	D_{50} (μm)	0.3
Composition (wt%)		**Compositions (wt%)**	
Al_2O_3	99.8	Al_2O_3	99.96
Na_2O	0.07	Na_2O	0.001
Fe_2O_3	0.02	Fe_2O_3	0.01
MgO	0.05	MgO	0.03
SiO_2	0.03	SiO_2	0.006
CaO	0.02	CaO	0.001

For both the Bayer process and non-Bayer process Al_2O_3, particle size distributions were measured for the as-received powders, and then after various times using a sedimentation technique with traditional Imhoff settling cone and sedimentation cylinders. Assuming spherical shape, particles in a viscous medium settle according to Stokes' Law (Eq. 2),[152] where particles of similar density settle in a fluid with a velocity in proportion to the diameter of the particle according to $v \propto d^2$:

$$v = \frac{(\rho_p - \rho_f) g d^2}{18\eta} \quad (2)$$

Sample suspensions were mixed and allowed to settle in either Imhoff cones or sedimentation cylinders for various times between 1 and 100 hours to observe reductions in agglomeration (if any); then the liquid was carefully decanted from the sediment at the bottom of the settling container. Depending on the sample, either the decanted suspension and/or the sediment was then ultra-sonicated and the particle size distribution analyzed.

For the Bayer-process Al_2O_3, an additional investigation using wet ball milling was completed. Sample suspensions were created at 30 vol% solids loading and dispersed at 0.4 mg/m^2 using a NH_4-PMAA polyelectrolyte (Darvan C-N, Vanderbilt Minerals, LLC, Norwalk, CT). Suspensions were removed at various milling times and diluted to 3 vol%, then the PSD was measured as described above.

6.3.1 Imaging Powder Agglomerates in Dry Powders

Several complications exist for imaging dry ceramic powders, including a tendency for the powders to spontaneously agglomerate in air due to Van der Waals attractive forces, and their propensity to develop an electrical charge when placed in vacuum under an SEM beam. This study utilized a method to coat a glass microscope slide with Al_2O_3 powder based on a heterocoagulation method previously developed to electrostatically and homogeneously coat Al_2O_3 particles with SiO_2.[153-154] This method utilizes opposing electrostatic charges to disperse the Al_2O_3 particles onto the SiO_2 slide, where the zeta (ζ) potentials of the two species are opposite over the pH range of 2 to 9 (Figure 6.5). Hydrochloric acid (HCl) was used to lower the pH of an Al_2O_3 suspension at 3 vol% into this buffer, then a glass slide was dipped into the suspension, removed, and dried. This method resulted in a thin layer of Al_2O_3 particles on the slide from which large agglomerates could be imaged (Figure 6.6). Sample slides with the dispersed Al_2O_3 particles were then coated using a gold sputter coater (108, Cressington, Watford, England) and imaged via SEM (JSM-7800F, JOEL USA, Inc., Peabody, MA).

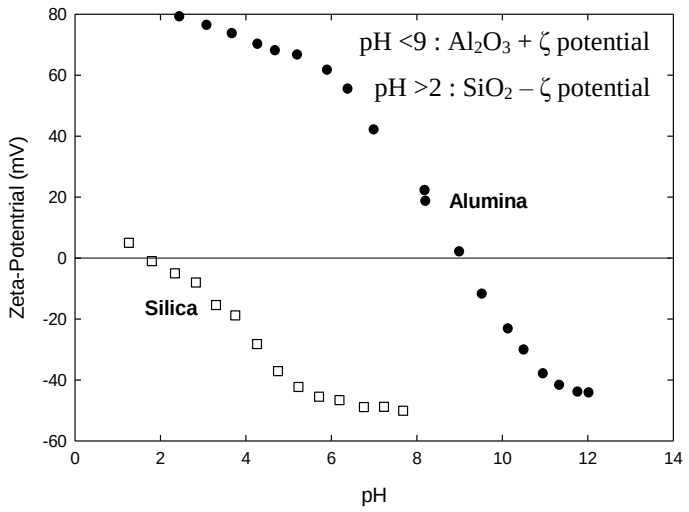

Figure 6.5. ζ-potentials for Al_2O_3 and SiO_2 at various pH values.[153]

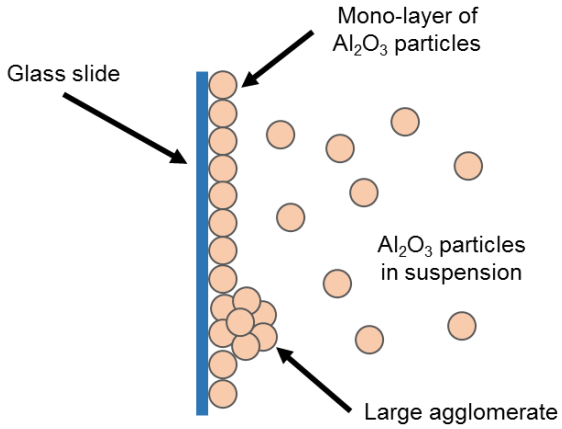

Figure 6.6. Heterocoagulation process for imaging dispersed Al_2O_3 powders on a glass slide.

6.4 Results and Discussion

Figure 6.7 presents SEM images of as-received Al_2O_3 powder for (a) Bayer-process Al_2O_3 and (b) an Al_2O_3 derived from an aluminum alkoxide precursor. The Bayer-process Al_2O_3 reveals large agglomerates in the range of 5-15 μm in size, on the scale of 10-30x larger than the reported D_{50} particle size for this powder. The high purity Al_2O_3 produced via chemical synthesis methods was not observed to have significant agglomeration, as can be observed in Figure 6.7(b), revealing homogenous Al_2O_3 particles.

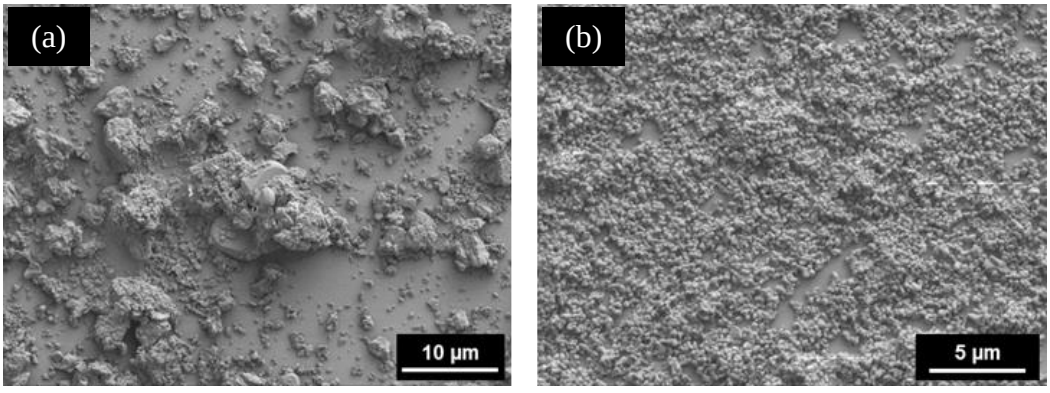

Figure 6.7. As-received powder for (a) a Bayer-process Al_2O_3 (99.8%) and (b) a non-Bayer process Al_2O_3 derived from aluminum alkoxide (99.96%).

6.4.1 Sedimentation-Decanting Process to Remove Agglomeration

A sedimentation technique was used to observe the differences in agglomeration and particle size distributions with settling time for both the Bayer-process and non-Bayer process Al_2O_3 powders. Figure 6.8 presents the Bayer-process powder after sedimentation for 100 hours for (a) the decanted powder with agglomerates reduced and/or eliminated, and (b) the powder sediment with the settled agglomerates. Particle size distributions were measured for an as-received, a decanted, and a sediment suspension for both Al_2O_3 powders (Figure 6.9). As observed in Figure 6.9(a), sedimentation narrows the PSD and shifts the average particle size (D_{50}) to the left by ~0.1 μm, whereas the sediment powder exhibits a wider distribution with a larger average particle size, indicative of agglomerates of varying size. Seen in the PSD of the non-Bayer-process Al_2O_3 (Figure 6.9(b)), 100 hours of sedimentation essentially does not alter the PSD, with identical D_{50} values across the as-received, decanted, and sediment powder suspensions. This constant distribution implies little to no agglomeration in the case of this powder, and supports the lack of agglomeration observed in Figure 6.8.

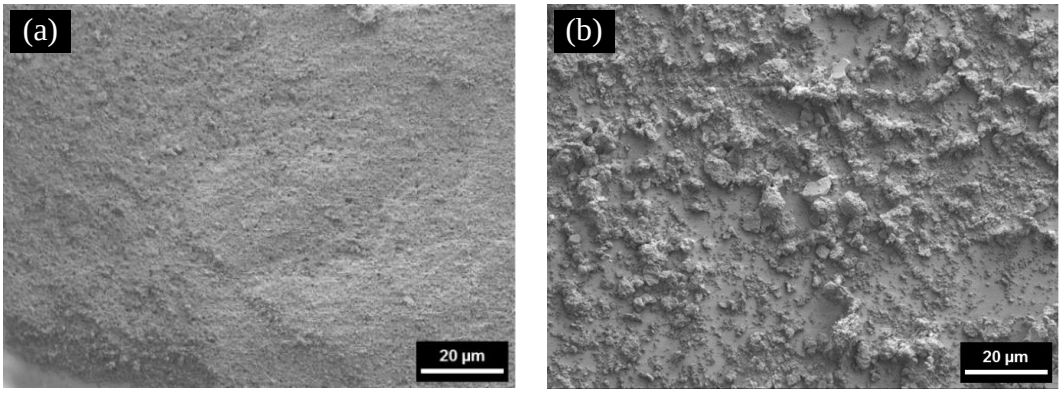

Figure 6.8. Industrial-grade Bayer process Al_2O_3 (99.8%) after sedimentation for 100 hours: (a) the decanted powder and (b) the powder sediment.

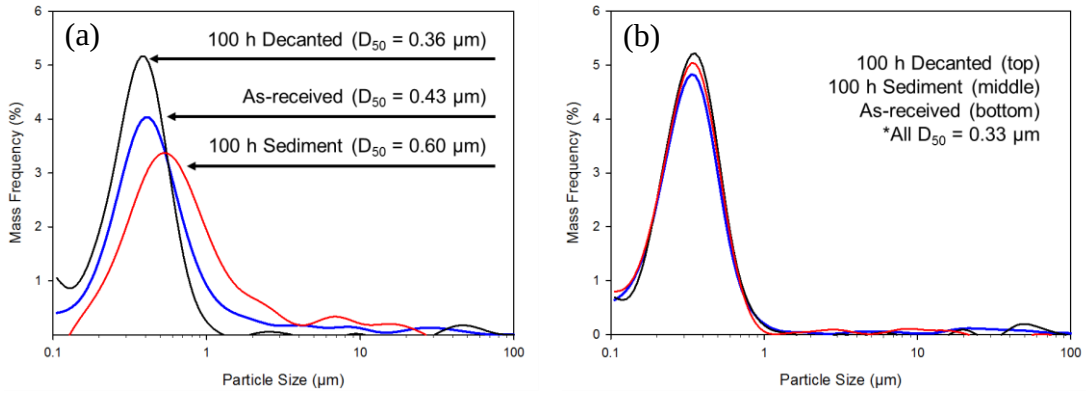

Figure 6.9. Mass frequency versus particle size for (a) Bayer process Al_2O_3 and (b) non-Bayer process Al_2O_3. The distributions include the as-received and both the decanted and powder sediment after 100 hours of sedimentation.

The measured particle size distributions were then plotted on a cumulative mass finer than (CMFT) linear axis versus log particle size, which is typical industrial practice for analyzing and reporting particle sizes (Figure 6.10). From these plots, the D_{50} average particle sizes can be determined for each sample, meaning 50% of the powder by mass is that size or smaller. For the Bayer-process Al_2O_3 (Figure 6.10(a)), the D_{50} value changes only slightly with sedimentation time until 100 hours, where a further decrease in D_{50} occurs. For the non-Bayer-process Al_2O_3 (Figure 6.10(b)), there is no discernable difference in D_{50} values with sedimentation time up to 100 hours. While each of these particle size distribution curves appear "normal" regarding their general curvature shape on the CMFT linear axis, the two as-received curves begin to show concavity well below 100% mass, which typically suggests the presence of agglomeration. It is difficult however, to discern the extent of agglomeration using the CMFT graphs.

These deviations in the distributions are more clearly observed when plotted on a probability (Gaussian) axis versus log particle size (Figure 6.11). Using a probability axis, it can be easily determined if a particle size distribution follows a normal distribution based on the linearity of the curve, or in this case, a log-normal distribution since the x-axis is presented on a log scale. From these plots, an estimate of how much agglomeration is present in a powder can be made based on where the curves deviate from linearity, approximately 70% for the Bayer-process Al_2O_3 and 88% for the non-Bayer-process Al_2O_3 in this case. The result indicates approximately 30% by mass of the Bayer-process Al_2O_3

sample consists of agglomerates, which range anywhere from 1 to greater than 30 μm in size. While the D_{50} values change by a miniscule amount with sedimentation time, the shift from the asymmetrical curve to a linear trend line indicates that the sedimentation is successful to significantly remove the agglomerates and normalize the particle size distribution, as indicated by the shift towards linearity with increasing sedimentation time in both powder cases.

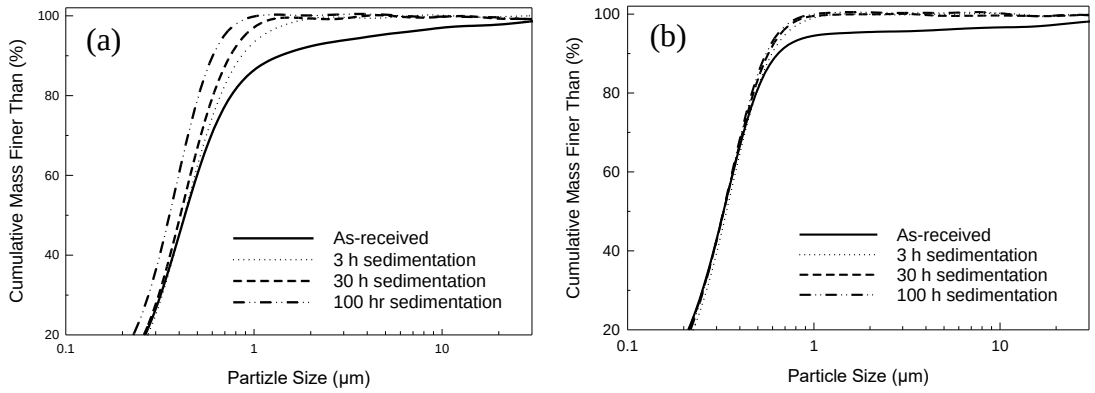

Figure 6.10. Particle size distributions on a CMFT linear axis versus log particle size for (a) Bayer-process Al_2O_3 and (b) non-Bayer-process Al_2O_3.

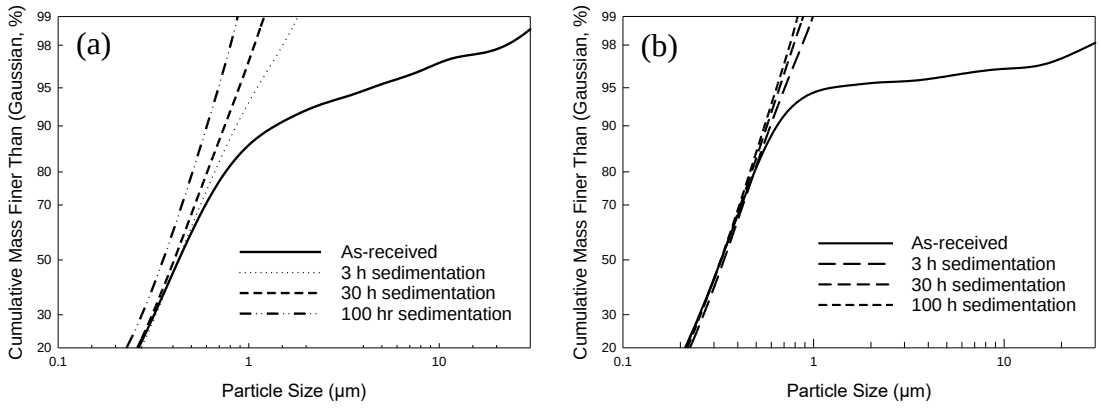

Figure 6.11. Particle size distributions on a CMFT Gaussian probability axis versus log particle size for (a) Bayer-process Al_2O_3 and (b) non-Bayer-process Al_2O_3.

The observed differences in agglomeration between the two Al_2O_3 powder types have been further investigated to observe the influence the agglomeration may have on

densification during sintering. Powder suspensions after various sedimentation times were slip cast and fired at 1500°C for 1 and 10 hours; then their relative densities were measured (Figure 6.12). For the as-received powders, identified by the points on the y-axis in Figure 6.12, the Bayer-process Al_2O_3 densified to several percent relative density lower (approximately 2-5%) than the non-Bayer-process Al_2O_3 for both sintering times. Sedimentation was not observed to improve the densification of the non-Bayer-process Al_2O_3, with a relatively constant relative density achieved even up to 100 hours of sedimentation in both sintering cases. Such densification was expected behavior since very little (if any) agglomeration was detected in this powder, so sedimentation is expected to have an insignificant effect on densification. For short sintering times (1 hour), there does not appear to be a significant difference in densification for the Bayer-process Al_2O_3; however, for the 10 hour case (6.12(b)), there was a significant increase in achievable relative density observed for sedimentation times of 10 hours and above. With longer sedimentation times and therefore greater reduction in the presence of agglomerates, the achievable relative densities can be seen to increase by several percent when compared to the as-received Al_2O_3.

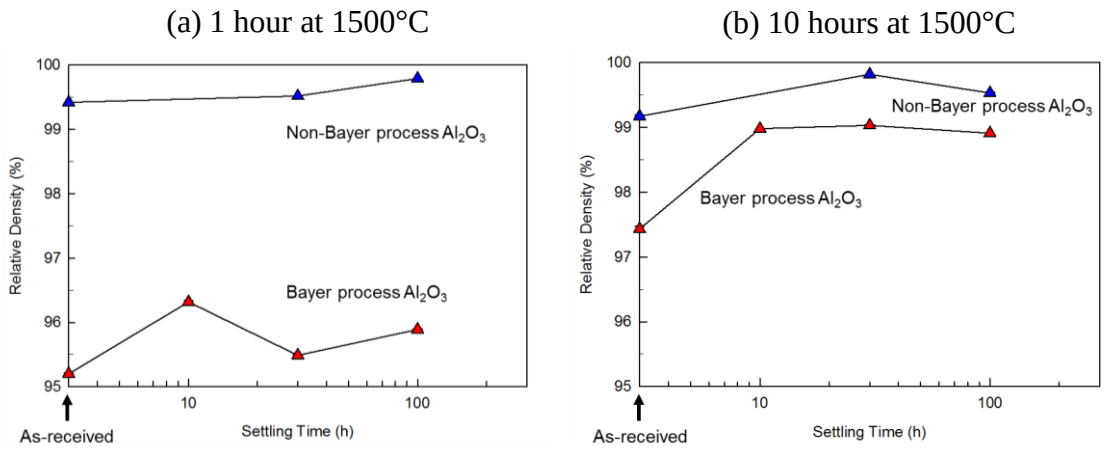

Figure 6.12. Relative density versus sedimentation time for decanted Al_2O_3 suspensions for a Bayer process Al_2O_3 (99.8%) and a high purity Al_2O_3 (non-Bayer process) produced from an aluminum alkoxide process (99.96%). All sample suspensions were dried, slip cast and sintered for (a) 1 hour at 1500°C and (b) 10 hours at 1500°C.

6.4.2 Sedimentation versus Milling for Elimination of Agglomerates

As discussed above, sedimentation was demonstrated to be an effective method to reduce the agglomeration commonly observed in Bayer-process Al_2O_3. Although it is effective, sedimentation on a larger scale for industrial production methods, may not be practical. Milling, which is commonly used in industry for both mixing and grinding, was therefore investigated to see if this method could also effectively reduce agglomeration in Al_2O_3.

The effects of both wet ball milling and sedimentation on PSD of Bayer-process Al_2O_3 can be observed in Figure 6.13. PSDs are represented on a probability (Gaussian) axis as this method is more conducive to observing the state of agglomeration in powders, as proposed an shown previously. After milling for as little as 1 hour, a change in D_{50} particle size can be observed (Figure 6.13(a)). This average particle size essentially remains the same until a prolonged milling time (100 hours) is achieved. As can be seen with the shift from a curved to a linear relationship with longer milling times, this method appears to be effective in normalizing the particle size distribution as agglomerates are eliminated. This trend is also observed with sedimentation, as longer sedimentation time results in a more linear PSD and a shift towards a log-normal distribution. This distribution is more representative of typical milled ceramic powder distributions, which have been previously classified, and would therefore be expected for Al_2O_3 powders where no (or very little) agglomeration is present.[144]

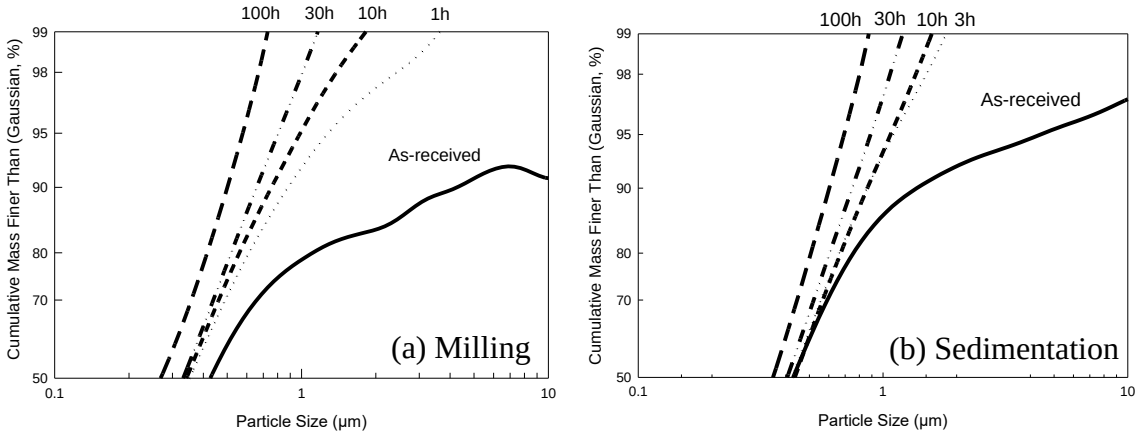

Figure 6.13. Particle size distributions of Bayer process Al_2O_3 on a probability axis for (a) as-received Al_2O_3 and after milling for various times and (b) as-received Al_2O_3 and after sedimentation for various times.

6.5 Conclusion

This study demonstrated the systemic agglomeration inherent in Bayer-process Al_2O_3 compared to a high purity Al_2O_3 from an alternative production method. It was revealed that plotting particle size distributions on a probability axis as opposed to the traditional cumulative mass percent plots is more effective for identifying and representing agglomeration in a powder system. Both milling and sedimentation techniques effectively reduced (or eliminated) large agglomerates; however, these methods can be energy intensive and may not be practical on an industrial scale, which should be taken into consideration when deciding if further processing is necessary for a Bayer-process Al_2O_3. The presence of agglomerates should be taken into consideration when analyzing and reporting particle size distributions, as the most commonly reported D_{50} mass percent value may not accurately represent the distribution of the system if significant agglomeration is present.

7. CONCLUSIONS

This study investigated the densification and grain growth behavior of industrial grade Al_2O_3 sintered in the presence of a glass phase with compositions in the CaO-Al_2O_3-SiO_2 (CAS) system. One study was conducted to investigate the applicability of using statistical experimental design to represent densification in liquid phase sintered ceramics, specifically for Al_2O_3 with liquid phase chemistries in the CAS system (Chapter 3). A clear time and temperature dependence was observed for densification of the as-received powder (99.8 wt%), but a discontinuity emerged with the addition of significant glass phase, where no time dependence was observed. Statistical experimental designs using partial factorial models were less complete in describing asymptotic systems for densification than full factorial models. In some cases, the partial models were unable to detect individual factor significances that the full factorial models identified. It was determined that densification behavior can be grouped by the relative compositions of the glass phase, more specifically the SiO_2:CaO ratios.

A strong effect of glass phase chemistry on grain growth was also observed for varying SiO_2:CaO ratios, as was observed with densification behavior (Chapters 4 and 5). Normal grain growth shown in glass phase chemistries with SiO_2:$CaO>1$, and normal grain growth accompanied by significant secondary phase formation was observed in chemistries with SiO_2:$CaO \leq 1$. Average Al_2O_3 grain size was observed to increase with increasing CaO content up to a point where excessive secondary phase formation occurred, where there was then a decrease in Al_2O_3 grain size. The differences in average grain sizes are proposed to be due to differences in densification across these systems and not differences in grain growth rates, as the corresponding growth rates were comparable. The differences in grain size are instead claimed to be due to a critical point of densification, where the onset of accelerated grain growth begins approximately ≥98% relative density. The secondary phases observed to form during sintering within the CAS system studied can be explained using the Glass Formation Boundary approach to predict sintering behavior. The discrepancies observed regarding crystalline phases predicted to form within the formation region are proposed to be due to solid state reactions which occur at lower temperatures than glass phase formation.

Two subsequent studies were conducted in relation to this work: (1) an investigation of how to best represent and etch Al_2O_3 microstructures with significant glass phase (Chapter 2), and (2) the detection and removal of agglomerates inherent in Bayer-process Al_2O_3 powder (Chapter 6). The results of the etching study determined that a chemical etch, followed by a high temperature thermal etch was the most effective in order to maximize contrast between Al_2O_3 grains and prevent secondary crystallization on the sample surface. While this method removes the glass from the grain boundaries of all samples, it allows for unobstructed imaging of Al_2O_3 grain boundaries for improved grain size analysis. The agglomeration study showed that, while the use of industrial-grade Al_2O_3 (99.8 wt%) is widespread, typical Bayer-process Al_2O_3 includes large agglomerates which limit the achievable densification of these powders. Both milling and sedimentation were demonstrated to be effective techniques to reduce the extent of this agglomeration and to effectively normalize the particle size distributions of Al_2O_3 powders.

8. FUTURE WORK

In regard to modeling densification, as discussed in Chapter 3, it may be useful to investigate a shorter timescale for the varying glass phase compositions to determine if a time dependence on densification is present at shorter times. For the study conducted, time was expected to be a significant factor for densification; however, it was not to be the case for the industrial ceramics time scale investigated (1-10 hours). This finding opposes historical arguments for liquid phase sintering, where the liquid phase is believed to aid the system in densifying at shorter times during sintering. It is proposed that a shorter sintering time may reveal time to be significant on the scale of minutes rather than hours, which might suggest some ceramic sintering schedules "over-fire" their products if a specific achieved density is the goal.

Another topic that might warrant further investigation involves associating the glassy grain boundary phase chemistries investigated in this work with physical properties (viscosity, density, etc.) and relating those properties to the densification and grain growth behaviors observed. The glass phase viscosity upon sintering is believed to influence the densification behavior, at least before full densification is achieved, by easing or hindering particle rearrangement during sintering. It is argued that glass with a higher viscosity will densify at a higher temperature (and potentially a longer time, if observed on a short enough scale) than glass phases with a lower viscosity. This would relate to the poor densification seen in the glass phase chemistry with only additional SiO_2 added, which would be expected to have a higher viscosity than the other compositions with added CaO, and would act as a glass modifier in the "normal" glass phase range.

A major anomaly observed in the glass formation boundary approach to predicting grain boundary phases was the crystallization of anorthite and gehlenite observed in many samples in Chapters 4 and 5. Rather than form as secondary products which crystallize from the glass phase, these phases are argued to form during solid state reactions at lower temperatures than when the glass phase forms during sintering. Solid state sintering trials would be useful in order to confirm or deny this explanation for their formation, possibly using high temperature XRD to determine the temperatures when anorthite and gehlenite (and in some cases grossite) form at intervals up to the sintering temperatures investigated

in this work. Previous work within the CAS system has attributed anorthite and gehlenite formation to solid state reactions as low as 954 and 933°C, respectively, so it would be anticipated that their presence would be detected between these temperatures and the temperatures of this work where their presence was also detected (1450 and 1550°C).[41, 60, 137-138]

A future area of interest regarding grain size analysis involves developing an automated method for measuring and representing grain sizes in liquid-phase sintered ceramics. Preliminary work has been performed using ImageJ to convert micrographs to a binary image for analysis, outlined in Figure 8.1; however, the contrast quality of samples with significant glass phase further complicate automated processes. Using an automated method, it would be possible to measure the average grain size, as well as the size of individual grains, and observe trends in grain size distributions. For the samples observed in this study, no abnormal grain growth of Al_2O_3 grains was visually observed. Therefore, statistical distributions of these microstructures are expected to follow a normal distribution, such as that demonstrated in Figure 1.7(a), if further analyzed. With an automated method, comparisons could also be made between the distributions of Al_2O_3 grains and the secondary phases observed, mainly hibonite ($CaO{\cdot}6Al_2O_3$), none of which is possible with the linear intercept methods utilized in this work.

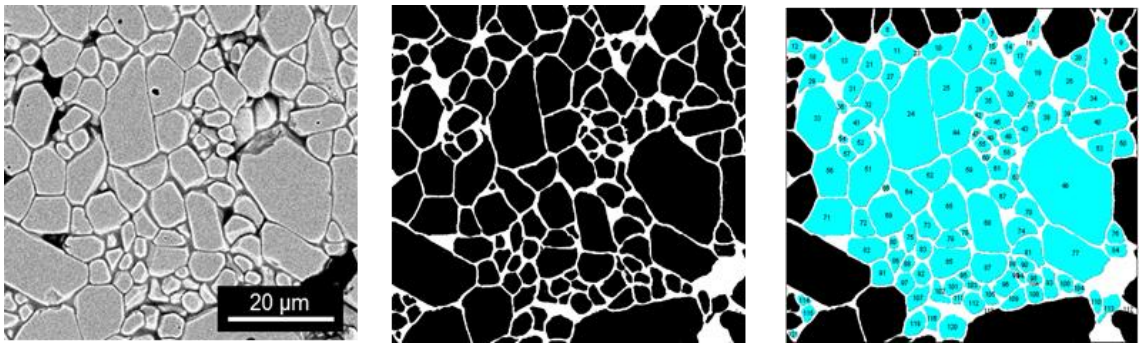

Figure 8.1. Al_2O_3 microstructure BSE image (left) converted to a binary image (middle) and analyzed for average grain size by area (right).

9. REFERENCES

1. Frueh, T. Mechanisms of Sintering and Second Phase Formation in Bayer Alumina. Ph.D. Thesis, The Pennsylvania State University, State College, PA, 2017.

2. Rahaman, M. N. Liquid-Phase Sintering. In *Ceramic Processing and Sintering*, CRC Press: Boca Raton, 2003; pp 620-687.

3. Coble, R. L. Sintering Crystalline Solids. I. Intermediate and Final State Diffusion Models. *J. Appl. Phys.* **1961,** *32* (5), 787-792.

4. Coble, R. L. Sintering Crystalline Solids. II. Experimental Test of Diffusion Models in Powder Compacts. *J. Appl. Phys.* **1961,** *32*, 793-799.

5. Berry, K. A.; Harmer, M. P. Effect of MgO Solute on Microstructure Development in Al_2O_3. *J. Am. Ceram. Soc.* **1986,** *69* (2), 143-149.

6. Handwerker, C. A.; Morris, P. A.; Coble, R. L. Effects of Chemical Inhomogeneities on Grain Growth and Microstructure in Al_2O_3. *J. Am. Ceram. Soc.* **1989,** *72*, 130-136.

7. Frueh, T.; Marker, C.; Kupp, E. R.; Compson, C.; Attria, J.; Gray, J. L.; Liu, Z. K.; Messing, G. L. Powder Chemistry Effects on the Sintering of MgO-Doped Specialty Al_2O_3. *J. Am. Ceram. Soc.* **2018,** *101* (7), 2739-2751.

8. Gavrilov, K. L.; Bennison, S. J.; Mikeska, K. R.; Chabala, J. M.; Levi-Setti, R. Silica and Magnesia Dopant Distributions in Alumina by High-Resolution Scanning Secondary Ion Mass Spectroscopy. *J. Am. Ceram. Soc.* **2004,** *82* (4), 1001-1008.

9. Svancarek, P.; Galusek, D.; Calvert, C.; Loughran, F.; Brown, A.; Brydson, R.; Riley, F. A Comparison of the Microstructure and Mechanical Properties of Two Liquid Phase Sintered Aluminas Containing Different Molar Ratios of Calcia-Silica Sintering Additives. *J. Eur. Ceram. Soc.* **2004,** *24*, 3453-3463.

10. Koyama, T.; Nishiyama, A.; Niihara, K. Effect of a Small Amount of Liquid-Forming Additives on the Microstructure of Al_2O_3. *J. Mater. Sci.* **1993,** *28*, 5953-5956.

11. Park, S. Y. Influence of a Liquid Phase on the Microstructure Development of Al_2O_3. *J. Mater. Sci. Lett.* **1996,** *15*, 878-880.

12. Rossi, G.; Burke, J. E. Influence of Additives on the Microstructure of Sintered Al_2O_3. *J. Am. Ceram. Soc.* **1973,** *56* (12), 654-659.

13. Dong, W.; Jain, H.; Harmer, M. P. Liquid Phase Sintering of Alumina I. Microstructure Evolution and Densification. *J. Am. Ceram. Soc.* **2005,** *88* (7), 1702-1707.

14. Brydson, R.; Chen, S. C.; Riley, F. L.; Milne, S. J.; Pan, X.; Ruhle, M. Microstructure and Chemistry of Intergranular Glassy Films in Liquid-Phase Sintered Alumina. *J. Am. Ceram. Soc.* **1998,** *81* (2), 369-379.

15. Bae, S. I.; Baik, S. Determination of Critical Concentrations of Silica and/or Calcia for Abnormal Grain Growth in Alumina. *J. Am. Ceram. Soc.* **1993,** *76* (4), 1065-1067.

16. Rodel, J.; Glaeser, A. M . Anisotropy of Grain Growth in Alumina. *J. Am. Ceram. Soc.* **1990,** *73*, 3292-3301.

17. Ahn, J. H.; Lee, J. H.; Hong, S. H.; Hwang, N. M.; Kim, D. Y. Effect of the Liquid-Forming Additive Content on the Kinetics of Abnormal Grain Growth in Alumina. *J. Am. Ceram. Soc.* **2003,** *86* (8), 1421-1423.

18. Park, C. W.; Yoon, D. Y. Effects of SiO_2, CaO_2, and MgO Additions on the Grain Growth of Alumina. *J. Am. Ceram. Soc.* **2000,** *83* (10), 2605-2609.

19. Yoo, J. H.; Nam, J. C.; Baik, S. Quantitative Evaluation of Glass-Forming Impurities in Alumina: Equivalent Silica Concentration (ESC). *J. Am. Ceram. Soc.* **1999,** *82* (8), 2233-2238.

20. Bateman, C. A.; Bennison, S. J.; Harmer, M. P. Mechanism for the Role of Magnesia in the Sintering of Alumina Containing Small Amounts of a Liquid Phase. *J. Am. Ceram. Soc.* **1989,** *72* (7).

21. Rahaman, M. N. Grain Growth and Microstructure Control. In *Sintering of Ceramics*, CRC Press: Boca Raton, 2008; pp 105-176.

22. Rahaman, M. N. Sintering of Ceramics: Fundamentals. In *Sintering of Ceramics*, CRC Press: Boca Raton, 2008; pp 1-43.

23. Shaw, T. M. Liquid Redistribution During Liquid-Phase Sintering. *J. Am. Ceram. Soc.* **1986,** *69* (1), 27-34.

24. Kaysser, W. A.; Sprissler, M.; Handwerker, C. A.; Blendell, J. E. Effect of a Liquid Phase on the Morphology of Grain Growth in Alumina. *J. Am. Ceram. Soc.* **1987,** *70* (5), 339-343.

25. Kostic, E.; Boskovic, S.; Kiss, S. J. Reaction Sintering of Al_2O_3 in the Presence of the Liquid Phase. *Ceram. Int.* **1993,** *19*, 235-240.

26. Dong, W.; Jain, H.; Harmer, M. P. Liquid Phase Sintering of Alumina III. Effect of Trapped Gases in Pores on Densification. *J. Am. Ceram. Soc.* **2005,** *88* (7), 1714-1719.

27. Dong, W.; Jain, H.; Harmer, M. P. Liquid Phase Sintering of Alumina II. Penetration of Liquid Phase into Model Microstructures. *J. Am. Ceram. Soc.* **2005,** *88* (7), 1708-1713.

28. Paladino, A. E.; Kingery, W. D. Aluminum Ion Diffusion in Aluminum Oxide. *J. Chem. Phys.* **1962,** *37* (5), 957-962.

29. Bennison, S. J.; Harmer, M. P. Grain-Growth Kinetics for Alumina in the Absence of a Liquid Phase. *J. Am. Ceram. Soc.* **1985,** *68* (1), C-22-C-24.

30. Chan, T. Y.; Liu, S. J.; Lin, S. T. Effects of High Concentrations of Liquid Phase and Magnesia on the Grain Growth of Alumina. *Ceram. Int.* **1997,** *24*, 617-625.

31. Goswami, A. P.; Roy, S.; Mitra, M. K.; Das, G. C. Impurity-Dependent Morphology and Grain Growth in Liquid-Phase-Sintered Alumina. *J. Am. Ceram. Soc.* **2001,** *84* (7), 1620-1626.

32. Echeberria, J.; Castro, F.; Riley, F. L. Grain Growth in Liquid-Phase-Sintered Alumina. *Mater. Sci. Forum* **1993,** *113-115*, 579-584.

33. Altay, A.; Gulgun, M. A. Microstructural Evolution of Calcium-Doped α-Alumina. *J. Am. Ceram. Soc.* **2003,** *86* (4), 623-629.

34. Hong, S. H.; Kim, D. Y. Effect of Liquid Content on the Abnormal Grain Growth of Alumina. *J. Am. Ceram. Soc.* **2001,** *84* (7), 1597-1600.

35. Altay, A.; Gulgun, M. A. Calcium in Alpha-Alumina: The Myth and Some EM Observations. *Key Eng. Mater.* **2004,** *264-268*, 219-224.

36. Mallamaci, M. P.; Sartain, K. B.; Carter, C. Barry. Crystallization of Calcium Hexaluminate on Basal Alumina. *Philos. Mag. A* **1998,** *77* (3), 561-575.

37. Kaplan, W. D.; Mullejans, H.; Ruhle, M.; Rodel, J.; Claussen, N. Ca Segregation to Basal Surfaces in α-Alumina. *J. Am. Ceram. Soc.* **1995,** *78* (10), 2841-2844.

38. Mullejans, H.; Kaplan, W. D.; Ruhle, M. Interfaces Between α-Al_2O_3 in Melt-Infiltrated Alumina. *Mater. Sci. Forum* **1996,** *207-209*, 405-408.

39. Dillon, S. J.; Harmer, M. P.; Rohrer, G. S. Influence of Interface Energies on Solute Partitioning Mechanisms in Doped Aluminas. *Acta Mater.* **2010,** *58* (15), 5097-5108.

40. Nakajima, A.; Messing, G. L. Liquid-Phase Sintering of Alumina Coated with Magnesium Aluminosilicate Glass. *J. Am. Ceram. Soc.* **1998,** *81* (5), 1163-1172.

41. Lam, T. Glass Formation Boundary Approach to the Sintering of Alumina. Ph.D. Thesis, Alfred University, Alfred, NY, 2010.

42. Phillips, D.; Shiue, Y. In *Adv. in Cer.*, The American Ceramic Society: Columbus, OH, 1984.

43. Powell-Dogan, C. A.; Heuer, A. H. Microstructure of 96% Alumina Ceramics: III, Crystallization of High-Calcia Boundary Glasses. *J. Am. Ceram. Soc.* **1990,** *73* (12), 3684-3691.

44. Seabaugh, M. M.; Messing, G. L.; Vaudin, M. D. Texture Development and Microstructure Evolution in Liquid-Phase-Sintered α-Alumina Ceramics Prepared by Templated Grain Growth. *J. Am. Ceram. Soc.* **2000,** *82* (12), 3109-3116.

45. Lawrence, A. K.; Kundu, A.; Harmer, M. P.; Compson, C.; Atria, J.; Spreij, M. Influence of Complexion Transitions on Microstructure Evolution in Specialty Aluminas. *J. Am. Ceram. Soc.* **2015,** *98* (4), 1347-1355.

46. Dillon, S. J.; Tang, M.; Carter, W. Craig; Harmer, M. P. Complexion: A New Concept for Kinetic Engineering in Materials Science. *Acta Mater.* **2007,** *55*, 6208-6218.

47. Dillon, S. J.; Harmer, M. P. Relating Grain Boundary Complexion to Grain Boundary Kinetics I: Calcia-Doped Alumina. *J. Am. Ceram. Soc.* **2008,** *91* (7), 2304-2313.

48. Dillon, S. J.; Harmer, M. P. Relating Grain Boundary Complexion to Grain Boundary Kinetics II: Silica-Doped Alumina. *J. Am. Ceram. Soc.* **2008,** *91* (7), 2314-2320.

49. Dillon, S. J.; Harmer, M. P. Demystifying the Role of Sintering Additives with "Complexion". *J. Eur. Ceram. Soc.* **2008,** *28*, 1485-1493.

50. Dillon, S. J.; Harmer, M. P.; Rohrer, G. S. The Relative Energies of Normally and Abnormally Growing Grain Boundaries in Alumina Displaying Different Complexions. *J. Am. Ceram. Soc.* **2010,** *93* (6), 1796-1802.

51. Adamson, A. N.; Bloore, E. J.; Carr, A. R. Basic Principles of Bayer Process Design. In *Essential Readings in Light Metals: Alumina and Bauxite*, John Wiley and Sons: 2013; Vol. 1, pp 100-117.

52. Louet, N.; Gonon, M.; Fantozzi, G. Influence of the Amount of Na_2O and SiO_2 on the Sintering Behavior and in the Microstructural Evolution of a Bayer Alumina Powder. *Ceram. Int.* **2005,** *31* (7), 981-987.

53. Frueh, T.; Kupp, E. R.; Compson, C.; Attria, J.; Messing, G. L. The Effects of Na_2O and SiO_2 on Liquid Phase Sintering of Bayer Al_2O_3. *J. Am. Ceram. Soc.* **2016,** *99* (7), 1-6.

54. Powell-Dogan, C. A.; Heuer, A. H. Microstructure of 96% Alumina Ceramics: I, Characterization of the As-Sintered Materials. *J. Am. Ceram. Soc.* **1990,** *73* (12), 3670-3676.

55. Powell-Dogan, C. A.; Heuer, A. H. Microstructure of 96% Alumina Ceramics: II, Crystallization of High-Magnesia Boundary Glasses. *J. Am. Ceram. Soc.* **1990,** *73* (12), 3677-3683.

56. Uhlmann, D. R. Glass Formation, A Contemporary View. *J. Am. Ceram. Soc.* **1983,** *66* (2), 95-100.

57. Shelby, J.E. Formation and Properties of Calcium Aluminosilicate Glasses. *J. Am. Ceram. Soc.* **1985,** *68* (3), 155-158.

58. Lam, Thomas. Glass Melts as Indicators for Liquid Phase Sintering in Alumina. M.S. Thesis, Alfred University, Alfred. NY, 2007.

59. Varshneya, A.K. *Fundamentals of Inorganic Glasses*. 2nd ed.; Society of Glass Technology: Sheffield, 2013.

60. Quinlan, B. The Unity Molecular Formula Approach to Glaze Development. M.S. Thesis, Alfred University, Alfred, NY, 2002.

61. DeCarlo, K. J.; Lam, T. F.; Carty, W. M. In *Advances in Sintering Science and Technology - International Conference on Sintering,* The American Ceramic Society: 2010.

62. Carty, W. M. Observations on the Glass Phase Composition in Porcelains. *Ceram. Eng. Sci. Proc.* **2002,** *23* (2), 79-94.

63. DeCarlo, K. Dissolution of Alumina in Silicate Glasses. M.S. Thesis, Alfred University, Alfred, NY, 2008.

64. Rawson, H. In *Inorganic Glass Forming Systems,* Academic Press: New York, 1967; pp 91-94.

65. Moesgaard, M.; Yue, Y. Compositional Dependence of Fragility and Glass Forming Ability of Calcium Aluminosilicate Melts. *J. Non-cryst. Solids* **2009,** *355* (14), 867-873.

66. Otminski, J. Predicting Glass Formation from Melt Viscosity and Fragility. B.S. Thesis, Alfred University, Alfred, NY, 2013.

67. Hafner, H. C.; Kreidl, N. J.; Weidel, R. A. Optical and Physical Properties of Some Calcium Aluminate Glasses. *J. Am. Ceram. Soc.* **1958,** *41* (8), 315-323.

68. Richet, P.; Roskosz, M.; Roux, J. Glass Formation in Silicates: Insights from Composition. *Chem. Geol.* **2006,** *225,* 388-401.

69. Varshneya, A. K.; Cooper, A. R.; Cable, M. Changes in Composition During Electron-Microprobe Analysis of K_2O-SrO-SiO_2 Glass. *J. Appl. Phys.* **1966,** *75* (4), 2199.

70. Taffner, U.; Carle, V.; Schafer, U. Preparation and Microstructural Analysis of High-Performance Ceramics. In *ASM Handbook*, ASM International: Materials Park, OH, 2004; Vol. 9, pp 1057-1066.

71. Zipperian, D. C.; Diaz, D. Metallographic Specimen Preparation. *Adv. Mater. Process.* **2000,** *158* (4), 52-54.

72. Chinn, R.E. Etching. In *Ceramography*, ASM International: Materials Park, OH, 2002; pp 45-68.

73. Vander Voort, G. F. In *Practical Applications of Quantitative Metallography, ASTM STP 839*: 1984.

74. van der Berg, N. G.; Malherbe, J. B.; Botha, A. J.; Friedland, E. Thermal Etching of SiC. *Appl. Surf. Sci.* **2012,** *258*, 5561-5566.

75. E112. Standard Test Methods for Determining Grain Size. ASTM International: West Conshohocken, PA, 2013.

76. Chinn, R. E. Quantitative Ceramography. In *Ceramography*, ASM International: Materials Park, OH, 2002; pp 145-175.

77. Mendelson, M. I. Average Grain Size in Polycrystalline Ceramics. *J. Am. Ceram. Soc.* **1969,** *52* (8), 443-446.

78. German, R. M.; Olevsky, E. A. Modeling Grain Growth Dependence on the Liquid Content in Liquid-Phase-Sintered Materials. *Metall. Mater. Trans. A* **1998,** *29A*, 3057-3067.

79. Johnson, C.A.; Tucker, W.T. *Fracture Statistics in Design and Application*; General Electric Company, Corporate Research and Development: Schenectady, NY, 1979; pp 1-13.

80. E1181. Standard Test Methods for Characterizing Duplex Grain Sizes. ASTM International: West Conshohocken, PA, 2008.

81. Hassanzadeh-Tabrizi, S. A.; Taheri-Nassaj, E. Modeling and Optimization of Densification of Nanocrystalline Al_2O_3 Powder Prepared by a Sol-Gel Method Using Response Surface Methodology. *J. Sol-Gel. Sci. Technol.* **2011,** *57* (2), 212-220.

82. Marchi, J.; Bressiani, J. C.; Bressiani, A. H. A. Experimental Design Applied to Silicon Carbide Sintering. *J. Am. Ceram. Soc.* **2003,** *86* (7), 1208-10.

83. Marchi, J.; Bressiani, J. C.; A. H. A. Bressiani; Bruns, R. E. Mixture Design and Response Surface Analysis of Densification of Silicon Carbide Ceramics with (SiO_2-Dy_2O_3-Al_2O_3) Additives. *Int. J. Appl. Ceram. Technol.* **2010,** *7* (4), 493-501.

84. Hurst, J. B.; Millard, M. L. Evaluation of α-SiC Sintering Using Statistical Methods. *J. Am. Ceram. Soc.* **1985,** *68* (7), 178-181.

85. Li, J.; Peng, J.; Guo, S.; Zhang, L. Application of Response Surface Methodology (RSM) for Optimization of Sintering Process for the Preparation of Magnesia Partially Stabilized Zirconia (Mg-PSZ) Using Natural Baddeleyite as Starting Material. *Ceram. Int.* **2013,** *39* (1), 197-202.

86. Azadbeh, M.; Mohammadzadeh, A.; Danninger, H.; Gierl-Mayer, C. On the Densification and Elastic Modulus of Sintered Cr-Mo Steels. *Metall. Mater. Trans. B* **2015,** *46* (3), 1471-1483.

87. Box, G. E. P.; Hunter, W. G.; Hunter, J. S. Response Surface Methods. In *Statistics for Experimenters*, Sons, J. W., Ed. John Wiley & Sons, Inc.: New York, 1978; pp 510-539.

88. Bezerra, M. A.; Santelli, R. E.; Oliviera, E. P.; Villar, L. S.; Escaleira, L. A. Response Surface Methodology (RSM) as a Tool for Optimization in Analytical Chemistry. *Talanta* **2008,** *76* (5), 965-977.

89. Mason, R. L.; Gunst, R. F.; Hess, J. L. Response-Surface Designs. In *Statistical Design and Analysis of Experiments*, John Wiley & Son, Inc.: New York, 1989; pp 204-233.

90. Ujah, C. O.; Popoola, A. P. I.; Popoola, O. M.; Aigbodion, V. S. Optimisation of Spark Plasma Sintering Parameters of Al-CNTs-Nb Nano-Composite Using Taguchi Design of Experiment. *Int. J. Adv. Manuf. Technol.* **2018,** *100* (5-8), 1563-1573.

91. Correia, S. L.; Hotza, D.; Segadães, A. M. Simultaneous Optimization of Linear Firing Shrinkage and Water Absorption of Triaxial Ceramic Bodies Using Experiments Design. *Ceram. Int.* **2004,** *30* (6), 917-922.

92. Box, G. E. P.; Hunter, W. G.; Hunter, J. S. Significance Tests and Confidence Intervals for Means, Variances, Proportions, and Frequencies. In *Statistics for Experimenters*, Sons, J. W., Ed. John Wiley & Sons, Inc.: New York, 1978; pp 107-150.

93. Mason, R. L.; Gunst, R. F.; Hess, J. L. Polynomial Models. In *Statistical Design and Analysis of Experiments*, John Wiley & Son, Inc.: New York, 1989; pp 486-509.

94. Salleh, E. M .; Ramakrishnan, S.; Hussain, Z. In *3rd International Conference on Mathematical Sciences,* AIP Conf. Proc.: 2014.

95. Salleh, E. M.; Zuhailawait, H.; Ramakrishnan, S.; Gepreel, M. A. H. A Statistical Prediction of Density and Hardness of Biodegradable Mehanically Alloyed Mg-Zn Alloy Using Fractional Factorial Design. *J. Alloys Compd.* **2015,** *644*, 476-484.

96. Bosomworth, P. A.; Harmer, M. P. Surface Coating Technique for Revealing Grain Structures in Alumina. *J. Am. Ceram. Soc.* **1988,** *71* (4), C-174-175.

97. Petzow, G. Ceramography. In *Metallographic Etching*, 2 ed.; ASM International: Materials Park, OH, 1999; pp 154-174.

98. Warshaw, S. I.; Seider, R. Comparison of Strength of Triaxial Porcelains Containing Alumina and Silica. *J. Am. Ceram. Soc.* **1967,** *50* (7), 337-343.

99. Carbarjal, L.; Rubio-Marcos, F.; Bengochea, M. A.; Fernandez, J. F. Properties Related Phase Evolution in Porcelain Ceramics. *J. Eur. Ceram. Soc.* **2007,** *27* (4065-69).

100. Correia, S. L.; Oliveira, A. P. N.; Hotza, D.; Segadães, A. M. Properties of Triaxial Porcelain Bodies: Interpretation of Statistical Modeling. *J. Am. Ceram. Soc.* **2006,** *89* (11), 3356-65.

101. Stathis, G.; Ekonomakou, A.; Stournaras, C. J.; Ftikos, C. Effect of Firing Conditions, Filler Grain Size and Quartz Content on Bending Strength and Physical Properties of Sanitaryware Porcelain. *J. Eur. Ceram. Soc.* **2004,** *24* (2357-66).

102. Tucci, A.; Esposito, L.; Malmusi, L.; Rambaldi, E. New Body Mixes for Porcelain Stoneware Tiles with Improved Mechanical Characteristics. *J. Eur. Ceram. Soc.* **2007,** *27*, 1875-81.

103. Esposito, L.; Salem, A.; Tucci, A.; Gualtieri, A.; Jazayeri, S. H. The Use of Nepheline-Syenite in a Body Mix for Porcelain Stoneware Tiles. *Ceram. Int.* **2005,** *31*, 233-40.

104. Leonelli, C.; Bondioli, F.; Veronesi, P.; Romagnoli, M.; Manfredini, T.; Pellacani, G. C.; Cannillo, V. Enhancing the Mechanical Properties of Porcelain Stoneware Tiles: A Microstructural Approach. *J. Eur. Ceram. Soc.* **2001,** *21*, 785-793.

105. Lundin, S. T. Microstructure of Porcelain. In *Microstructure of Ceramic Materials, NBS Miscellaneous Special Publication 257*, U.S. Government Printing Office: Washington D.C., 1964; pp 93-106.

106. Carty, W. M.; Senapati, U. Porcelain—Raw Materials, Processing, Phase Evolution, and Mechanical Behavior. *J. Am. Ceram. Soc.* **1998,** *81* (1), 3-20.

107. Iqpal, Y.; Lee, W. E. Fired Porcelain Microtructures Revisited. *J. Am. Ceram. Soc.* **1999,** *82* (12), 3584-90.

108. Iqpal, Y.; Lee, W. E. Microstructural Evolution in Triaxial Porcelain. *J. Am. Ceram. Soc.* **2000,** *83* (12), 3121-27.

109. Bernardo, E.; Esposito, L.; Rambaldi, E.; Tucci, A.; Hreglich, S. Recycle of Waste Glass into "Glass-Ceramic Stoneware". *J. Am. Ceram. Soc.* **2008,** *91* (7), 2156-62.

110. Chmelik, F.; Trnik, A.; Štubňa, I.; Pešička, J. Creation of Microcracks in Porcelain During Firing. *J. Eur. Ceram. Soc.* **2011,** *31*, 2205-09.

111. Martín-Márquez, J.; Rincón, J.; Romero, M. Effect of Firing Temperature on Sintering of Porcelain Stoneware Tiles. *Ceram. Int.* **2008,** *24*, 1867-73.

112. Bragança, S. R.; Bergmann, C. P.; Hübner, H. Effect of Quartz Particle Size on the Strength of Triaxial Porcelain. *J. Eur. Ceram. Soc.* **2006,** *26*, 3761-68.

113. Nyongesa, F. W.; Aduda, B. O. The Effect of Quartz and Mullite Phases on Strength of Triaxial Porcelain. *East African J. Phys. Sci.* **2004,** *5* (1), 11-24.

114. Tulyaganov, D. U.; Agathopoulos, S.; Fernandes, H. R.; Ferreira, J. M. F. Influence of Lithium Oxide as Auxiliary Flux on the Properties of Triaxial Porcelain Bodies. *J. Eur. Ceram. Soc.* **2006,** *26*, 1131-39.

115. Lee, W. E.; Iqpal, Y. Influence of Mixing on Mullite Formation in Porcelain. *J. Eur. Ceram. Soc.* **2001,** *21*, 2583-86.

116. Kara, A.; Stevens, R. Interactions Between an ABS Type Leadless Glaze and a Biscuit Fired Bone China Body During Glost Firing. Part II: Investigations of Interactions. *J. Eur. Ceram. Soc.* **2002,** *22*, 1103-12.

117. Kivitz, E.; Palm, B.; Heinrich, J. G.; Blumm, J.; Kolb, G. Reduction of the Porcelain Firing Temperature by Preparation of the Raw Materials. *J. Eur. Ceram. Soc.* **2009,** *29* (2691-96).

118. Pinto, B. M. Critical Evaluation of Strength-Controlling Variables in Ceramics. Ph.D. Thesis, Alfred University, Alfred University, 2006.

119. Pinto, B. M. Effect of Filler Particle Size on Porcelain Strength. M.S. Thesis, Alfred University, Alfred, NY, 2001.

120. Liebermann, J. Special Benefits of Bauxite for a Stable Porcelain Microstructure in High-Voltage Insulation. *ACerS Bulletin* **2017,** *96* (7), 32-35.

121. Elssner, G.; Hoven, H.; Kiessler, G.; Wellner, P. Revealing the Microstructure. In *Ceramics and Ceramic Composites: Materialographic Preparation*, Elsevier Science Inc.: New York, 1999; pp 39-44.

122. Moore, A. J. W. The Influence of Surface Energy on Thermal Etching. *Acta. Metall.* **1958,** *6*.

123. Chalmers, B.; King, R.; Shuttleworth, R. The Thermal Etching of Silver. *Proc. R. Soc. Lond. A* **1948,** *193*, 465-483.

124. Carty, W. M. The Processing of Ceramic Fibers from Particle Suspensions. Ph.D. Thesis, University of Washington, Seattle, WA, 1992.

125. Cesarano, J.; Aksay, I. A. Processing of Highly Concentrated Aqueous α-Alumina Suspensions Stabilized with Polyelectrolytes. *J. Am. Ceram. Soc.* **1988,** *71* (12), 1062-1067.

126. Cesarano, J.; Aksay, I. A.; Bleier, A. Stability of Aqueous α-Al_2O_3 Suspensions with Poly(methacrylic acid) Polyelectrolyte. *J. Am. Ceram. Soc.* **1988,** *71* (4), 250-255.

127. B962-17. Standard Test Methods for Density of Compacted or Sintered Powder Metallurgy (PM) Products Using Archimedes' Principle. ASTM International: West Conshohocken, PA, 2017.

128. Mason, R. L.; Gunst, R. F.; Hess, J. L. *Statistical Design and Analysis of Experiments*. John Wiley & Sons, Inc.: New York, 1989.

129. Box, G. E. P.; Hunter, J. S.; Hunter, W. G. *Statistics for Experimenters*. John Wiley & Sons, Inc.: New York, 1978.

130. Cochran, W. G.; Cox, G. M. *Experimental Designs*. 2nd ed.; John Wiley & Sons, Inc.: New York, 1992.

131. Montgomery, D. C. *Design and Analysis of Experiments*. 3rd ed.; John Wiley & Sons, Inc.: New York, 1991.

132. Norton, F. H. Effect of Heat on Fine Ceramics Bodies. In *Fine Ceramics*, Robert E. Krieger Publishing Co.: Huntington, NY, 1978; pp 269-270.

133. Lerdprom, W. Firing of Porcelain. Alfred University, Alfred, NY, 2014.

134. *Design Expert 11*, Stat-Ease, Inc.: Minneapolis, MN, 2018.

135. Rawson, H. Inorganic Glass-Forming Systems. Academic Press: New York, 1967; pp 11-29.

136. Gupta, T. K. Possible Correlation Between Density and Grain Size During Sintering. *J. Am. Ceram. Soc.* **1972,** *55* (5), 276-277.

137. Traore, K.; Kabre, T. S.; Blanchart, P. Gehlenite and Anorthite Crystallisation from Kaolinite and Calcite Mix. *Ceram. Int.* **2003,** *29* (4), 377-383.

138. Traore, K.; Philippe, B. Structural Transformation of a Kaolinite and Calcite Mixture to Gehlenite and Anorthite. *J. Mater. Res.* **2003,** *18* (2), 475-481.

139. Svancarek, P.; Galusek, D.; Loughran, F.; Brown, A.; Brydson, R.; Atkinson, A.; Riley, F. Microstructure-Stress Relationships in Liquid-Phase Sintered Alumina Modified by the Addition of 5 wt.% of Calcia-Silica Additives. *Acta Mater.* **2006,** *54* (18), 4853-4863.

140. Gentile, A. L.; Foster, W. R. Calcium Hexaluminate and Its Stability Relations in the System CaO-Al_2O_3-SiO_2. *J. Am. Ceram. Soc.* **1963,** *46* (2), 74-76.

141. Song, H.; Coble, R. L. Morphology of Platelike Abnormal Grains in Liquid-Phase-Sintered Alumina. *J. Am. Ceram. Soc.* **1990,** *73* (7), 2086-2090.

142. Habashi, F. A Hundred Years of the Bayer Process for Alumina Production. In *Essential Readings in Light Metals: Alumina and Bauxite*, John Wiley and Sons: 2013; Vol. 1, pp 83-93.

143. Johnson, C.A.; Tucker, W.T. Advanced Statistical Concepts of Fracture in Brittle Materials. In *Engineered Materials Handbook*, ASM International: 1991; Vol. 4, pp 709-715.

144. Kini, D. S. Potential Graphical Quality Control Tool for Evaluating Particle Size Distributions. M.S. Thesis, Alfred University, Alfred, NY, 2014.

145. Jillavenkatesa, A.; Dapkunas, S. J.; Lum, L. S. H. Reporting Size Data. In *Particle Size Characterization*, National Institute of Standards and Technology: Washington, DC, 2001; Vol. 960-1, pp 125-137.

146. Rahaman, M. N. Powder Characterization. In *Ceramic Processing and Sintering*, CRC Press: Boca Raton, 2003; Vol. 23, pp 128-136.

147. Smith, J. E.; Jordan, M. L. Mathematical and Graphical Interpretation of the Log-Normal Law for Particle Size Distribution Analysis. *J. Colloid Sci.* **1964,** *19*, 549-559.

148. Kottler, F. The Distribution of Particle Sizes. *J. Franklin I.* **1950,** *250* (4), 339-356.

149. Allen, T. Powder Sampling and Particle Size Measurement. In *Particle Size Measurement*, Chapman & Hall: London, 1997; Vol. 1, pp 44-108.

150. Reed, J. S. Particle Size and Shape. In *Principle of Ceramics Processing*, 2nd ed.; John Wiley & Sons, Inc.: New York, 1995; pp 92-117.

151. Barndorff-Nielson, O. Exponentially Decreasing Distributions for the Logarithm of Particle Size. *Proc. R. Soc. Lond. A* **1977,** *353* (1674), 401-419.

152. Rahaman, M. N. Powder Characterization. In *Ceramic Processing and Sintering*, CRC Press: Boca Raton, FL, 2003; p 141.

153. Carty, W. Controlled Distribution of Nano-scale Sintering Dopants. June 5, 2012, 2012.

154. Tierney, K. Preparation of Magnesium Silicate Nanoparticles. B.S. Thesis, Alfred University, Alfred,NY, 2016.

10. APPENDIX

10.1 Sample Batch Calculation

Presented for a sample composition of 88 wt% Al_2O_3 with 1 SiO_2 : 0.33 CaO:

Target moles of oxide components	**CaO**	**1.00**
	Al_2O_3	**42.00**
	SiO_2	**6.40**

	CaO	**Al_2O_3**	**SiO_2**				
Target moles	**1.00**	**42.00**	**6.40**	**# moles**	**g/mole**	**grams component**	**wt% component**
EPK	0.027	2.700	6.400	2.700	280.36	757.09	15.53%
balance	0.973	39.300	0.000				
Whiting ($CaCO_3$)	0.973	0.000	0.000	0.973	100.09	97.39	2.00%
balance	0.000	39.300	0.000				
Al_2O_3	0.000	39.300	0.000	39.300	102.33	4021.53	82.48%
balance	0.000	0.000	0.000				
						4876.00 g batch	**100%**

Raw Material Unity Molecular Formulas
(molar ratios of oxide components in batch component)

	CaO	**Al_2O_3**	**SiO_2**	**Molecular Weight (g/mole)**
EPK	0.01	1.00	2.37	280.36
Whiting ($CaCO_3$)	1.00			100.09
Alumina		1.00		102.33

10.2 Confirmation Run Data for Statistical Experimental Design

Table 10.I. Confirmation Run Data Comparing Partial and Full Factorial Model Density Predictions

Factor Conditions				Density				
Time (h)	Temp. (°C)	Al_2O_3 Level (wt%)	SiO_2:CaO Ratio	Measured (%)	Partial Fact. Predicted (%)	Difference from Measured (%)	Full Fact. Predicted (%)	Difference from Measured (%)
			1:0	82.68	83.04	0.36	82.48	0.20
			1:0.15	97.22	96.55	0.67	96.98	0.24
			1:0.33	97.55	97.76	0.21	98.11	0.56
3	1500	92	1:1.0	96.70	98.11	1.41	97.99	1.29
			1:1.5	96.99	96.81	0.18	97.4	0.41
			1:4.5	91.57	95.73	4.16	91.23	0.34
			1:8.0	91.01	95.48	4.47	89.5	1.51
			1:0	81.78	81.34	0.44	81.51	0.27
			1:0.15	98.10	96.78	1.32	96.65	1.45
			1:0.33	97.31	97.22	0.09	98.31	1.00
7	1475	92	1:1.0	97.74	98.22	0.48	97.99	0.25
			1:1.5	95.70	97.66	1.96	97.4	1.70
			1:4.5	92.78	92.24	0.54	89.69	3.09
			1:8.0	90.96	93.01	2.05	88.52	2.44
			1:0	82.85	85.05	2.20	83.78	0.93
			1:0.15	98.99	96.38	2.61	97.33	1.66
			1:0.33	96.61	98.85	2.24	98.38	1.77
1.5	1525	92	1:1.0	98.76	98.62	0.14	97.99	0.77
			1:1.5	96.04	97.71	1.67	97.4	1.36
			1:4.5	93.76	97.13	3.37	92.79	0.97
			1:8.0	90.10	94.85	4.75	90.52	0.42
			1:0	80.71	79.7	1.01	79.69	1.02
			1:0.15	97.67	99.04	1.37	99.13	1.46
			1:0.33	97.44	98.87	1.43	98.39	0.95
7	1475	88	1:1.0	96.23	97.57	1.34	97.69	1.46
			1:1.5	95.95	97.26	1.31	97.04	1.09
			1:4.5	74.30	76.05	1.75	86.42	12.12
			1:8.0	88.19	86.43	1.76	91.49	3.30
			1:0	85.04	86.64	1.60	85.42	0.38
			1:0.15	98.80	99.37	0.57	98.67	0.13
			1:0.33	97.80	97.72	0.08	97.77	0.03
3	1525	88	1:1.0	98.60	96.68	1.92	97.69	0.91
			1:1.5	97.33	96.59	0.74	97.04	0.29
			1:4.5	83.56	86.67	3.11	89.83	6.27
			1:8.0	91.91	92.24	0.33	94.07	2.16

10.3 Relative Accuracy of Grain Size Measurements via Abrams Three-Circle Procedure

According to ASTM Standard E112,[75] the 95% confidence interval (CI) value and % relative accuracy (RA) of a group of samples can be determined using Equations 1 and 2, respectively:

$$95\%\ CI = \frac{t \cdot s}{\sqrt{n}} \qquad (1)$$

$$\%\ RA = \frac{95\%\ CI}{\bar{X}} \cdot 100 \qquad (2)$$

Where s = standard deviation of the number of intercepts, n = the number of view field measurements, t = CI multiplier (based on n), and $\bar{X}$ = the mean number of intercepts. For a 95% CI, a % RA below 10% is desired for reporting average grain size. For each sample condition measured, approximately 500 intercepts were counted over ~6 micrograph fields.

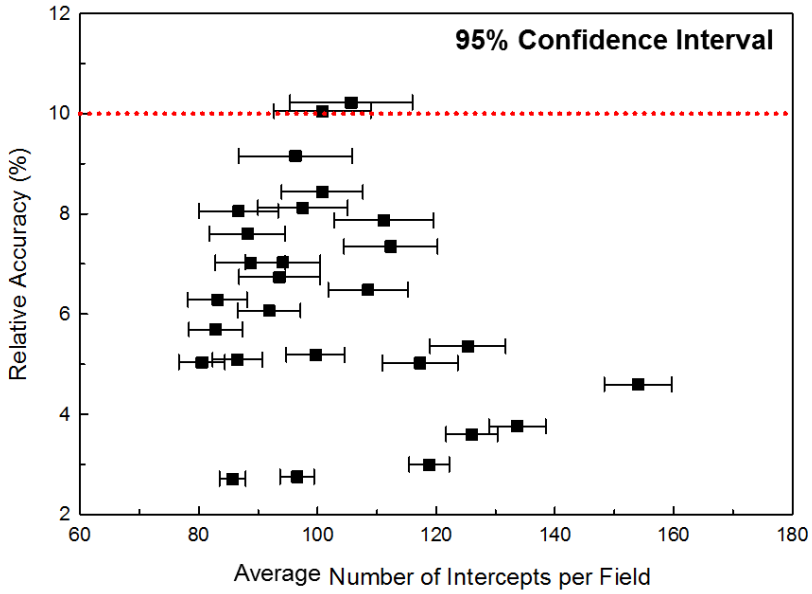

Figure 10.1. Percent relative accuracy versus average number of intercepts per field for 95% CI for samples measured with SiO_2:CaO>1.